

ME ChemE/MBA Jaeun Chung

**Nanoscale Characterization
of Epoxy Interphase
on Copper Microstructures**

BAM-Dissertationsreihe · Band 15
Berlin 2006

Die vorliegende Arbeit entstand an der Bundesanstalt für Materialforschung und -prüfung (BAM). Es handelt sich hierbei um eine bei der Fakultät III – Prozesswissenschaften der Technischen Universität Berlin eingereichte Dissertation zur Erlangung des akademischen Grades Doktor der Ingenieurwissenschaften – Dr.-Ing. – vorgelegt von ME ChemE/MBA Jaeun Chung aus Korea.

Promotionsausschuss: Prof. Dr. rer. nat. W. Reimers (Vorsitzender)
Prof. Dr.-Ing. M. H. Wagner (Berichter)
Dr. rer. nat. habil. E. Schulz (Berichter)

Tag der wissenschaftlichen Aussprache: 25. Januar 2006

Impressum

**Nanoscale Characterization of
Epoxy Interphase on Copper Microstructures**

2006

Herausgeber:
Bundesanstalt für Materialforschung und -prüfung (BAM)
Unter den Eichen 87
12205 Berlin
Telefon: +49 30 8104-0
Telefax: +49 30 8112029
E-mail: info@bam.de
Internet: www.bam.de

Copyright © 2006 by Bundesanstalt für
Materialforschung und -prüfung (BAM)

Verlag und Vertrieb:
Wirtschaftsverlag N. W.
Verlag für neue Wissenschaft GmbH
27568 Bremerhaven
Telefon: +49 471 94544-0
Telefax: +49 471 94544-77

Layout: BAM-Arbeitsgruppe Z.67

ISSN 1613-4249
ISBN 3-86509-514-3

Abstract

The epoxy/metal interface regions are recognized as crucial for the mechanical reliability of composite materials. In particular, the spatial stress distribution is governed by modulus variations, which may result from the physical-chemical interactions between epoxy and the metal surface. The properties of the interphase between bulk polymer and metal were analyzed in nanometer scale. It was aimed to characterize the stiffness gradient of the polymeric interphase, which was formed by a thermoset being cured in contact with a metal surface.

The means of the characterization was scanning force microscopy (SFM) in force modulation mode (FMM), which produces a high-resolution image to describe the stiffness variation. The analysis from the SFM-FMM correlated with the results of other methods such as dynamic mechanical analysis (DMA) and electron microscopy with energy dispersive X-ray analysis (EDX).

The composite material investigated consisted of epoxy and copper. Electron Beam Lithography (EBL) combined with lift-off technique was utilized to construct the copper microstructures on silicon wafers. The composite material was produced by curing the mixture of epoxy resin and amine-based hardener on the silicon wafer with the copper microstructures. Two different epoxy systems were used to produce two different kinds of composites. One consisted of a type of diglycidyl ether of bisphenol A (DGEBA) and a modified cycloaliphatic amine (EPIKOTE828 and EPIKURE F205, Resolution Europe). The other consisted of a type of DGEBA and an aromatic amine (DER332, Dow Chemical and DDS, Fluka Chemika). SFM-FMM depicted the mechanical property of the interphase, taking advantage of the novel sample preparation. The surface geometry of the interphase between epoxy and copper was flat and continuous; therefore it was optimized for the SFM-FMM characterization.

The stiffness gradient of the interphase was acquired by SFM-FMM, which detects the amplitude response of the SFM-cantilever operated in contact mode, while the sample is vertically modulated. Beside the FMM-amplitude image, other images were also available such as topography, normal force image, lateral force image and phase shift image. These contrasts were used for the recognition of the copper interface and the validation of the optimum condition of FMM analysis. When the slope of the analyzed surface exceeds $\sim|3^\circ|$, topography induced artifacts can be produced. In addition, the morphology of the epoxy surface was examined. With the applied curing parameters (T_g at 80°C for 2 hours, postcure at 130°C for 1 hour), the average size of the nodules were found to be ~ 125 nm, and more than 90 percent of the nodules have a length between 75 and 200 nm.

EPIKOTE828-EPIKURE F205 system formed an interphase width of ~ 1.9 μm with a minimum stiffness at ~ 0.4 μm away from the copper surface. On the other hand, DER332-DDS system produced an interphase with a width between 2.3 and 4.0 μm . The interphases contained heterogeneous stiffness profiles. The stiffness near the copper interface (up to 0.2–0.25 μm) was higher than that of the bulk. It indicates that the properties of a metal-induced interphase vary depending on the epoxy systems. The EDX with SEM and TEM revealed that the amine concentration was reduced near the copper in comparison with that in the bulk. The result from the SFM-FMM correlated with the modulus of cured epoxy with different amine concentrations, which was determined by DMA. These findings are interpreted with a reaction-diffusion model for the interphase formation. In conclusion, spatial variations of the epoxy network structure and mechanical properties occur via amine-epoxy concentration deviation.

Zusammenfassung

Die Grenzfläche zwischen Epoxid und Metall spielt für die mechanische Zuverlässigkeit des Verbundwerkstoffes (Composite) Epoxid/Metall eine wichtige Rolle. Insbesondere hängt die räumliche Verteilung mechanischer Spannungen von Variationen des Elastizitätsmoduls ab, die durch die physikalisch-chemischen Wechselwirkungen zwischen dem Epoxid und der Metalloberfläche hervorgerufen werden können. Daher wurden die Eigenschaften des Grenzbereichs (Interphase) zwischen dem Polymer, das nicht durch Grenzflächen-Wechselwirkungen beeinflusst wurde (Bulk-Polymer), und dem Metall auf der Nanometer-Skala analysiert. Hauptziel war es, die Steifigkeitsgradienten innerhalb der Epoxid-Interphase zu detektieren. Diese können durch die Gegenwart der Metall-Grenzfläche (Interface) hervorgerufen werden, die einen Einfluss auf den Prozess der Aushärtung zeigt.

Die Rasterkraftmikroskopie (Scanning Force Microscopy, SFM) im Force Modulation Mode (FMM) erlaubt die hochauflösende Abbildung von Steifigkeitsvariationen. Die Ergebnisse aus der SFM-FMM wurden mit Konzentrationsprofilen aus der energie-dispersiven Analyse von Röntgenstrahlen im Rasterelektronenmikroskop (REM-EDX) verglichen, als auch mit Relaxationskurven aus der dynamisch-mechanischen Analyse (DMA), die an Epoxid-Referenzproben durchgeführt wurde.

Die untersuchten Verbundwerkstoff-Proben bestanden aus Epoxid und Kupfer. Es wurde Elektronstrahl-Lithographie (EBL) in Verbindung mit der Lift-off Technik verwendet, um Kupfer-Mikroelektroden auf einem Silizium-Wafer herzustellen. Danach wurde die Mischung aus Epoxidharz und Amin-Härter in der Gegenwart der Kupfer-Mikroelektroden ausgehärtet, wodurch ein Epoxid/Kupfer Verbundwerkstoff entstand. Es wurden zwei verschiedene Epoxid-Härter Systeme verwendet, um unterschiedliche Probenotypen herzustellen. Eines bestand aus Diglycidyl-Ether des Bisphenol A (DGEBA) und einem modifizierten cycloaliphatischen Amin (EPIKOTE828 und EPIKURE F205 von Resolution Europe). Das andere bestand aus DGEBA und einem aromatischen Amin (DER332 von Dow Chemical und DDS von Fluka Chemikalien). SFM-FMM erlaubt es, die lokalen mechanischen Eigenschaften des Grenzbereichs zu beschreiben. Die neue Art der Probenpräparation ermöglicht es, eine an die Erfordernisse der SFM-FMM angepasste Glattheit der zu untersuchenden Oberfläche zu erzielen.

Bei der SFM-FMM wird die vertikale Position der Probe moduliert und die dynamische Verbiegungsamplitude des SFM-Cantilevers gemessen, während sich die Spitze im Kontakt mit der Probenoberfläche befindet. Neben dem resultierenden Amplituden- und Phasensignal sind noch andere Kontraste verfügbar, wie Topographie, Auflagekraft und Lateralkraft. Diese ergänzenden Kontraste wurden dazu verwendet, die Kupfer-Grenzfläche zu identifizieren. Ferner dienten sie der Kontrolle der Qualität der SFM-Messung. Insbesondere konnte gezeigt werden, dass von der Topographie induzierte Kontraste auftreten können, wenn ihre Neigung mehr als $\sim|3^\circ|$ beträgt. Außerdem wurde die Morphologie der Oberfläche des Epoxids untersucht, die noppenartige Strukturen, so genannte „Noduln“, aufwies. Bei den gegebenen Aushärtungsbedingungen (T_g bei 80°C über 2 Stunden, Nachhärtung bei 130°C über 1 Stunde) betrug die Durchschnittsgröße der Noduln ~ 125 nm, und 90 Prozent der Noduln waren zwischen 75 und 200 nm groß.

Das aus EPIKOTE828-EPIKURE F205 bestehende Epoxid-System bildete eine Interphase mit einer Breite von $\sim 1,9$ μm aus und der Punkt der niedrigsten Steifigkeit war in einem Abstand von $\sim 0,4$ μm vom Kupfer. Andererseits wies das DER332-DDS System eine Interphase mit einer Breite von $\sim 2,3$ – $4,0$ μm auf. Es wurden verschiedenartige Steifigkeitsprofile festgestellt. Diese Ergebnisse zeigen, dass die Eigenschaften des metallinduzierten Grenzbereichs vom Epoxid-System abhängen. Die Steifigkeit in der Nähe

von Kupfer (bis zu 0,2–0,25 μm Abstand) war deutlich höher als im Volumen des Epoxids. Sowohl die im REM als auch die im TEM durchgeführten EDX-Messungen zeigten, dass die Konzentration des Amins in der Nähe von Kupfer verringert ist. Die unter Verwendung von SFM-FMM gemessene Steifigkeit wurde mit dem Modulwert verglichen, der mittels DMA an Referenzproben wohldefinierter Amin-Epoxid Konzentrationsverhältnisse bestimmt wurde. Die gefundene Relation wurde im Rahmen eines Reaktions-Diffusions Modells interpretiert. Danach treten räumliche Schwankungen im Konzentrationsverhältnis von Amin und Epoxid auf, die zu Variationen in der Netzwerkstruktur des ausgehärteten Epoxids führen und sich somit auch auf dessen mechanische Eigenschaften auswirken.

할머니, 할아버지
my grandparents

When nothing is certain,
everything is possible.
-Anonymous-

Contents

1. Introduction	1
2. Polymer Matrix Composites and Interphases	3
2.1. Polymer matrix composites	4
2.1.1. Polymer/polymer composites and interphases	4
2.1.2. Glass and carbon fiber/polymer composites	5
2.1.3. Metal/polymer composites	6
2.1.3.1. Copper/epoxy interface	9
2.2. Significance of interphase	10
2.3. Mechanisms of interphase formation	12
2.3.1. Macromolecules at interfaces	12
2.3.2. Effects with thermosets	13
2.3.2.1. Epoxy systems	13
3. Epoxy Curing and Properties	17
4. Experimental Techniques	23
4.1. Scanning Force Microscopy in Force Modulation Mode	23
4.1.1. Fundamental principals of Scanning Force Microscopy	23
4.1.2. Theory of Force Modulation Mode	25
4.2. Depth-sensing Indentation	30
4.3. Electron microscopy with Energy Dispersive X-ray analysis	31
4.3.1. Scanning Electron Microscopy	31
4.3.2. Transmission Electron Microscopy	32
5. Analyses of Surface and Interphase	33
5.1. Stiffness measurement with Depth-sensing Indentation	33
5.2. Dynamic Mechanical Analysis	36
5.3. SFM-based stiffness measurement in Force Modulation Mode	36
5.3.1. Operating under the optimal configuration	36
5.3.2. Topography induced artifacts	40
5.3.3. Recognition of copper and epoxy surfaces	44
5.3.4. Recognition of the interphase in epoxy on copper	45
5.3.5. Advantages of Force Modulation Mode	47
5.4. Preparation of epoxy/copper composite	48
5.4.1. Epoxy interphase with copper microelectrodes	49
5.4.1.1. Preparation of substrate detached surface	49
5.4.1.2. Epoxy mixing and curing	51
5.4.1.3. Electron Beam Lithography	52
5.4.1.4. Metal evaporation and lift-off technique	54
5.4.2. Preparation of cross section surface	54
5.5. Properties of the epoxy/copper interphase	55
5.5.1. Copper and DGEBA-based epoxy with a cycloaliphatic curing agent	55

5.5.1.1. Interphase analysis of substrate detached surface	55
5.5.1.2. Cross section surface	58
5.5.2. Copper and DGEBA-based epoxy with an aromatic curing agent ..	59
5.5.2.1. SFM analysis of the interphase of epoxy/copper	59
5.5.2.2. Energy-dispersive analysis of X-rays for epoxy/copper interphase	63
5.6. Surface morphology of the cured epoxy	68
6. Epoxy Surface and Interphase	71
6.1. Epoxy/copper interphase	71
6.2. Nodules on the epoxy surface	78
7. Conclusion	81
Symbols	85
Abbreviations	87
References	88

1. Introduction

Knowledge of the mechanical properties of interphase is essential when designing multi-component materials such as fiber-reinforced matrix, protective coatings or multi-layered structures for integrated circuits. It can provide vital information for the durability of the finished product as a composite because its failure is often initiated in the interfacial region induced by internal or external stress during fabrication or service. A composite is usually referred as a manufactured material with two or more elements, which are distinguishable by an interface, but as a whole its characteristic is not depicted by any of the elements in isolation [1.1]. Composites in the industry are often categorized by the matrix phases, which are polymer, metal and ceramic. Here, a composite consists of polymer and metal is considered.

The composition of the multi-component thermosetting polymer can be altered by an adherend surface in the vicinity of the interface during the curing process. Thus, interphase can exist in solid/matrix composites like carbon fiber/polymer or metal/polymer composites. The interphase may be homogeneous, or it may exhibit a property gradient. In the case of the epoxy matrix composite, the interphase can be formed due to a stoichiometry imbalance [1.2,1.3,1.4]. As a result, the properties of the interphase are inclined to become different from the bulk. Drzal [1.5] has suggested that the interphase is more rigid than the bulk, while Piggott [1.6] has proposed that the interphase is softer. However, the previous studies were often experiments combined with a good deal of theoretical work and speculations. Moreover, a lack of experimental evidence and quantitative information of the interphase were suggested [1.3,1.6,1.7]. In the case of the amine based curing agent and epoxy resin, a high amine concentration region can be formed near the interface [1.5,1.8,1.9]. The redistribution of amine in the bulk cannot readily take place because of the increase in viscosity due to the polymerization [1.5]. Furthermore, models have predicted that this process leads to compositional gradients near the solid surface [1.10,1.11,1.12]. They were developed to present the interphase gradient accurately and to link the compositional gradients to the property gradients.

One approach to analyze the property gradient of such interphase is associating the material content in the interphase to the mechanical property results from bulk samples. The bulk samples are made of defined concentration ratios between epoxy and amine. An analysis such as dynamic mechanical analysis (DMA) is conducted with the samples to find out the change of Young's modulus depending on variation of the amine concentration. The results from the bulk samples can be linked to the analysis of interphase in an epoxy-fiber composite or epoxy-metal composite. When the composition of the interphase region is measured, it can be translated to mechanical property according to the test of the bulk samples [1.10,1.13]. In addition, a modeled prediction has been frequently used to determine the interphase content and properties. The models were developed considering the process parameters to find out the growth of the interphase width and its modulus gradient [1.11]. Thus, the properties of interphase were often found indirectly from predictions and analysis of bulk materials. A direct mechanical characterization in the interphase region has been limited by the size of the interphase, because it is too small to conduct an accurate mechanical testing with available instruments before SFM became

available. Non-mechanical analyses have been conducted on the interphasial material. Arayasantiparb *et al.* [1.14] used electron energy-loss spectroscopy (EELS) in a scanning transmission electron microscope (STEM) to study the size and composition of the epoxy-aluminum interphase. Although the result about the composition provides valuable information, the dimension of the interphase was still defined by the variation of the chemical composition rather than a mechanical property. Thus, it can only provide estimated stiffness information. However, since SFM became available, it was overlooked as feasibility for stiffness characterization of the interphase. VanLandingham *et al.* [1.15] used an indentation method with an SFM for the stiffness analysis in the interfacial region. In the interphase studies with SFM, the analysis of the bulk region is often simultaneously performed because the bulk region is always next to the interphase and it is used as the reference to the interphase properties. By comparing the interphase properties with the bulk properties, the alteration in the polymeric material due to the solid surface can be recognized. However, a quantitative measurement has been limited by the nature of the analytical technique. For example, a difficulty of the calibration restricts a measurement of Young's modulus in certain modes of SFM. The studies can yet characterize the interphase in comparison with the bulk.

In this study, two different epoxy systems were applied as the polymer material and copper was used as the metal. The two epoxy systems were EPIKOTE828-EPIKURE F205 and DER332-DDS, which are the commercial names shown as epoxy resin-hardener, respectively. The epoxy resins are based on diglycidyl ether of bisphenol A (DGEBA) and the hardeners are amine-based curing agent. EPIKURE F205 is a modified cycloaliphatic curing agent and DDS (4,4'-diaminodiphenylsulfone) is a sulfur-contained aliphatic curing agent. The two systems, especially the curing agents, consist of different chemical compounds, thus the reaction with the metal surface in the interfacial region may vary throughout the cure. Therefore, their interphase properties may be different. The formation of the interphase was deduced by describing the stiffness variation. The interphase was characterized by use of scanning force microscopy (SFM) in force modulation mode (FMM). SFM requires a flat surface for an adequate performance, especially for FMM. In order to satisfy this requirement, Electron Beam Lithography (EBL) was utilized to prepare the copper electrode, and epoxy-copper composite samples were constructed on silicon wafers, which were removed after the cure of the epoxy. In this research project, an extensive experimental study was undertaken to investigate the existence of the interphase and to describe the properties of the surface and interphase by means of SFM-FMM.

This thesis is organized by: the background of composites and interphase (Chapter 2), the introduction of epoxy (Chapter 3), the description and theory of the experimental techniques (Chapter 4), the experimental details and results (Chapter 5), the further discussions (Chapter 6), and the conclusion and prospects (Chapter 7).

2. Polymer Matrix Composites and Interphases

Interphase plays a crucial role in composites. Many important phenomena can occur at the matrix/reinforcement interface. Stiffening and strengthening rely on load transfer across the interface, toughness is influenced by crack deflection/fiber pull-out, and ductility is affected by relaxation of peak stresses near the interface. Large uncertainty surrounds the question of how best to characterize, and then optimize, the mechanical response of the interface to stresses arising from an applied load.

Composites are a combination of multiple components to produce materials with improved properties. Therefore, interphase is inevitable in composites. The composite industry is mainly divided into three manufacturing areas: Polymers, metals, and ceramics. Categorizing by their matrix phase, there are polymer matrix composites (PMCs), metal matrix composites (MMCs), and ceramic matrix composites (CMCs). When the composites are called *advanced*, it indicates that they combine the properties of high strength and high stiffness, low weight, corrosion resistance, and in some cases special electrical properties. This chapter deals with PMCs and their interphases as the reinforcements are in contact with the matrix materials.

In PMCs, the polymeric matrix materials can be divided in thermosets and thermoplastics. Glass fiber is often used as reinforcement in PMCs, and composite material made from a glass fiber and a polymer matrix is applied in a wide variety of industries: sporting goods, construction, aerospace, etc. Carbon is also considered as one of the most important fiber reinforcements. In addition, some other reinforcement materials are boron and aramid. CMCs take advantage of the unique properties of ceramics after filling its lack of toughness with reinforcements. Common ceramic matrix materials are SiC, Si₃N₄, and HfC. The advantages of ceramics are known as high strength and high stiffness at very high temperature, chemical inertness, low density, etc., but the major flaw of ceramics is the low toughness. The usual high fabrication temperature is a bearing point because of the mismatch of thermal expansion between reinforcement and matrix. CMCs have important roles in aerospace, e.g., in aircrafts, helicopters, and missiles. Another important application is cutting tool inserts [2.1]. MMCs are usually categorized by the reinforcing materials. The reinforcing component in the composite is normally ceramic, however sometimes a refractory metal is preferred. The shape of reinforcements like continuous fibers, short fibers or particles, can be used to subdivide MMCs. They are commonly used as stiffness and strength enhanced materials. Some examples with use of its stiffness enhancement are automotive drive shafts, racks to house electrical equipment, e.g., in aircrafts, and bicycles frames [2.2].

For polymer-based composites, although the chemistry involved may be complex, the objectives in terms of interfacial properties are often the rather straightforward ones of a high bond-strength (to transfer load efficiently to the fibers) and a good resistance to environmental attack. In designing ceramic composites, on the other hand, the aim is usually to make the interface very weak, as the prime concern is in promoting energy dissipation at the interface so as to raise the toughness. Metal composites usually demand a strong bond, but there may be instances where inelastic processes at the interface can be

beneficial. In addition, the avoidance of environmental attack is often less important than the need for control over chemical reactions between the constituents themselves, occurring during fabrications or under service conditions at high temperature.

2.1. Polymer Matrix Composites

Polymers are structurally more complex than metals or ceramics. They are in general inexpensive and easy to process. However, polymers have low strength and modulus, and do not resist to high temperature. They are generally poor conductors of heat and electricity, but they are more resistant to chemicals than metals [2.1]. PMC industry can be divided into two basic segments: industrial composites and advanced composites. The sector of industrial composites is a large industry and this accounts various resin systems including polyester, epoxy, and other specialty resins. These products are applied along with a catalyst or curing agent and some type of fiber reinforcement, and used in boats, piping, auto bodies, etc. The advanced composites are characterized by the use of expensive, high-performance resin systems and high-strength, high-stiffness fiber reinforcements. The aerospace industry is the major market for advanced composites. Composites are divided into two basic types according to the matrix polymer: thermosets and thermoplastics. When a polymer forms a network by crosslinking, it does not soften or melt on heating. Such a polymer is called a thermoset. Polymers that soften and melt by heating are thermoplastics. Thermosets are by far the predominant type in use today. Thermosets are subdivided into several resin systems including epoxies, phenolics, polyurethanes, and polyimides. Epoxy systems currently dominate the advanced composite industry.

2.1.1. Polymer/polymer composites and interphases

Polymers are commonly known to be immiscible with other polymers. A composite with two immiscible polymers may become a material, whose properties are worse than the properties of the individual polymers due to a weak interface. Thus, it defeats the purpose of creating a composite material. Adhesion between two miscible polymers is an important factor in polymer/polymer composites since it determines the overall quality of the material. During the formation of the adhesion between two polymers, wetting and diffusion are considered to be the most important factors at the interface. Wetting creates the initial contact between the two polymers. After the contact is established, the polymers diffuse across the interface and the interfacial region matures in time [2.3]. A sharp interphase at the initial contact broadens as the diffusion between the two polymers progresses. The extent of diffusion determines the extent of the interfacial region. This process affects the mechanical properties of the composite [2.4]. The ultimate properties of the material are determined by the interfacial structure and properties. Diffusion affects directly the adhesion process. The degree of adhesion always seems to be the main consideration in terms of the final performance.

The polymer/polymer interface is commonly seen in fundamental studies such as surface morphology and interface study between two miscible or immiscible polymers [2.5]. The layers of polymers are frequently seen in many practical applications such as adhesives, protective coatings, and multi-layer paints [2.6]. The diffusion and adhesion at polymer/polymer interface has important applications like various types of welding [2.7],

bioadhesion [2.8], and microelectronics [2.9]. Welding can be between two identical polymers, or just two chemically identical polymers with different number of monomers per chain, or two compatible polymers. Applications in bioadhesion are seen in pharmaceutical and biomedical areas. In microelectronics the encapsulation of a chip is often epoxy. When epoxy is applied on the polymeric dielectric layer such as polyimide to protect from the environment, the adhesion between the epoxy and the polymeric dielectric layer plays an important role.

2.1.2. Glass and carbon fiber/polymer composites

The fiber-reinforced composites are known for their high strength-to-weight ratio, corrosion resistance, and thermal and electrical insulating properties [2.10]. It has been for some time that glass fiber has been studied. For example, A. A. Griffith studied its crack and rupture characteristics against stress in 1920 [2.11]. They attempted to use glass fiber for reinforcement material in 1940, but it was not succeeded to fabricate. Fiberglass-reinforced silicone was recognized as an outstanding heat-resistant electrical insulator by J. F. Hyde at the Corning Glass Works. However, processing difficulties have been the major drawback for the advancement of the material in the industry [2.12]. Despite the slow beginnings with, nowadays, glass fiber is applied commonly as reinforcement material. In addition, application of the carbon fiber also has been spreading rapidly. Carbon fiber reinforced PMCs are widely used for lightweight, high strength and high modulus in the defense-related aerospace and commercial aircraft industry, followed by the sporting goods industry. Epoxy is the most commonly used for PMC with carbon fiber. Polyester, polysulfone, polyimide, and thermoplastic resins are also widely used [2.1, 2.13].

The mechanical properties of fiber/matrix composite rely on three factors: 1) Strength and modulus of the fiber, 2) strength and chemical stability of the resin, 3) effectiveness of the bond between resin and fiber in transferring stress across the interface [2.12]. The ultimate characteristics of fiber-reinforced composites rely on fiber properties and architecture, extent of resin cure and resultant matrix properties, quality of mold filling, and the nature of the fiber/polymer matrix interface. It is well accepted that the interface plays an important role, and the adhesion between the reinforcement and the matrix greatly influences the final properties of the composite [2.14]. It is often the case that polymer matrix and fiber reinforcement do not easily adhere together. For instance, carbon fiber with untreated surface and a typical amine-cured epoxy result in very low interfacial shear strength with failure taking place in the outer fiber surface layer [2.15]. In order to improve the adhesion between the fiber and the matrix, surface treatment of the fiber is used. Common treatments of carbon fiber mostly deal with etching of the surface and adding surface oxygen groups, which increase the concentration to about twice the level initially present on the fiber surface before surface treatment. This process doubles the adhesion level in terms of an interfacial shear strength test [2.16]. On the other hand, the surface of the glass fiber is often treated with size or coupling agent. Thickness of sizing is in the range from 0.5 to 1.0 μm for commercially available glass fibers with diameters between 10 to 14 μm . The size is commonly made of film former, silane coupling agents and auxiliary agent. The functions of silane coupling agents and their interactions with both the glass fibers and the polymer have been studied. The silanol groups react with the glass surface primarily via hydrogen bonds to form partly covalent bonds. The second functionality of the coupling agent has the ability to interact with the thermoplastic or thermosetting resin by a chemical

reaction [2.14, 2.17]. The interface region can make up a large fraction of the composite and it influences final properties of the material. The extent of the interphase in a fiber/matrix system is approximately 100 to 500 nm and may contain composition or property gradients between those of the fiber coating [2.10]. The interphase may be influenced by the type of coupling agent used to coat the fiber, the properties of the coupling agent layer, and the interaction between the resin and coupling agent [2.10].

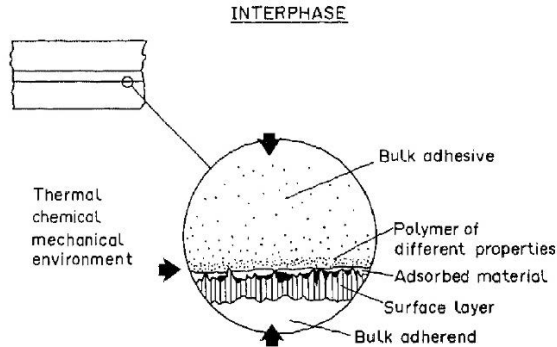


Figure 2-1. A Schematic model of interphase in fiber/matrix by L.T. Drzal [2.16]. The arrows represent the directions in which the thermal, mechanical or chemical environments can reach the interphase.

In view of an interface being two-dimensional between fiber and matrix, a three-dimensional region is built-on as interphase. Drzal [2.16] illustrated the possible components in an interphase with a schematic representation. Fig. 2-1 includes the contact between fiber and matrix (*interface*), adding a region of some finite thickness extending on both sides of the interface (*interphase*). The boundaries begin at the point in the matrix where the local properties start to change from the bulk properties in the direction of the interface. This region consists of matrix that may have chemical and morphological features different from the bulk matrix. At the interface, not only can there be chemical and physical interactions between fiber and matrix, but also voids, adsorbed gases and surface chemical groups can be concentrated. On the reinforcement side, morphological and chemical features can be different from the bulk. During the formation of the interphase, the processing conditions allow chemical reactions, volumetric changes and stresses to be generated. Thus, the resultant interphase can be a very complex material [2.16].

2.1.3. Metal/polymer composites

When the polymers are applied to the metallic substrates, the interaction between the matrix and metal surface creates an interphase, which has different chemical, physical, and mechanical properties from the bulk polymer. Metals and polymers have very different properties. When the two materials are in contact, owing to difference of their properties, a desired adhesion is often hard to be achieved. Being molecularly closely packed with strong metallic bonds, the metals have much higher cohesive energy (E_{coh}) than the polymers, whose cohesion is due to weak van der Waals bonds. Thermal expansion of metal is around 10 times smaller than polymer, and considerable amount of stress can be induced from the mismatch at the interface. And, metals are of course much stiffer than polymers. Some properties of copper and cured epoxy are compared in Table 2-1. Combination of

these differences produces difficulties processing the two materials together and may cause adhesion failures in the interphase between metal and polymer.

Table 2-1. Comparison of Copper and cured epoxy properties.

	Copper	Cured epoxy
Thermal expansion [$\mu\text{m}/(\text{m}\cdot\text{K})$]	16.5	45–65
Young's Modulus [GPa]	130	~2.5
Electrical property	Conductor (electrical conductivity $5.9 \times 10^7 / \Omega\cdot\text{m}$)	Insulator (dielectric strength $1.2\text{--}2 \times 10^7 \text{ V/m}$)

It is worthwhile to consider the condition of the metal surface to understand the metal/polymer interactions. Based on previous studies, a metal surface is actually a metal oxide surface [2.18]. Surface treatment can be done on the metal surface, but as soon as the metal surface is exposed to the atmosphere under normal ambient condition, an oxide layer will be created almost instantaneously in various thickness and structures, depending on the characteristics of the base metal and the condition of the environment. A model was developed to depict water and oxide layer on metals (Fig. 2-2). The oxide layer on metal surface is thin for mercury or for noble metals (gold, platinum), but thick (40–80 Å or more) enough for metals (like aluminum, iron, nickel, zinc, copper, magnesium, etc.), which are popular in the industries, so that the base metal underneath does not influence positively to form the adhesion force. Studies show that aluminum, iron and copper surfaces have up to twenty molecular layers of water present at ambient temperatures and humidity [2.19].

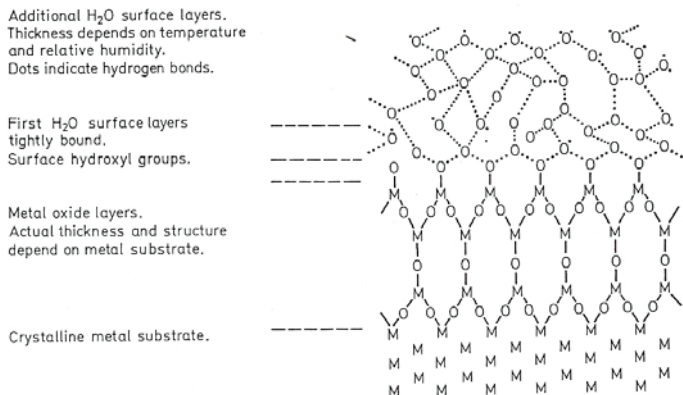


Figure 2-2. Schematic representation of water and oxide layers on a metal surface. M=metal atom, O=oxygen, OH=hydroxyl, H₂O [2.18].

One must not assume that the polymer/metal surface interaction should be equal on most metals because of the hydrated oxide surface layer on metals. The activity of the hydroxyl groups is different depending on the type of metal atom to which they are attached, and the number of hydroxyl groups on the surface can be varied by the temperature at the formation. For adhesive purpose, the hydrated oxide surface is helpful to enhance the wetting of metal surfaces by epoxies and other polar resins. It means that the surface also

attracts water and polar organic contaminants in atmosphere. In this case, the metal pretreatment can be done such as etching before applying adhesive and coatings [2.20].

From the studies of polymer interphase with aluminum it was found that the oxide morphology plays an important role to create strong adhesive joints, due to the presence of microscopically rough oxide surface to permit effective mechanical interlocking between adhesion and substrate [2.21]. The chemical composition of an interface can also have a large effect on the strength and durability of an adhesive joint or a coating. X-ray photoelectron spectroscopy (XPS) is often used to analyze the chemical compositions of the interphase [2.22]. There are other analytical techniques used to study metal/polymer interphase, e.g., ultraviolet photoemission spectroscopy [2.23], Fourier transform infrared reflection absorption spectroscopy [2.24], transmission electron microscopy [2.25], scanning force microscopy [2.26], etc.

Polymer on metal or *vice versa* can be found readily in various industries such as microelectronics, aerospace, automotive and food packaging [2.27]. Polymeric coating is, for example, applied to metallic layers for protection from corrosion. Metallic barrier layer such as aluminum is used in food packaging to keep moisture from the inside contents. In microelectronics, a polymer layer is suitable as a dielectric component in the multi-layered metal structure, e.g., integrated circuits (ICs) [2.28]. The desired low dielectric constant material^{*} in the industry can be satisfied by a polymeric material. The on-going interest of reduction of transistor gate length requires new materials. It has hastened the replacement of aluminum and SiO₂ as the interconnect metal and insulator of choice for silicon-based ICs with copper and so-called low-*k* material [2.29]. The possible candidates for low-*k* material are organic polymers and porous silicates. One of the utmost challenges in integrating these materials into microelectronic devices concerns the mechanical properties of the materials [2.29]. Despite the excellent dielectric constants, the degraded elastic performance of low-*k* materials compared to SiO₂ concerns the possible mechanical failure within the interconnect structure owing to externally applied stresses during interconnect planarization processing and/or thermally induced internal stresses from the thermal expansion coefficient mismatch of the dielectric and metallic components [2.29]. Besides the electrically non-conducting polymers, there are also conducting polymers. They are alternating-bond conjugated polymers [2.30]. Polymer-based light-emitting diodes (p-LEDs) can be fabricated from the conducting polymer. Indium tin oxide (ITO) is an important material in the p-LEDs fabrication. Subsequently the stability of the interphase between ITO and polymer plays an important role [2.31]. In addition, the conductive polymers can be utilized in conducting textiles, various antistatic coatings, etc.

Polymer metallization is often done with physical vapor deposition of metal atoms onto a polymeric substrate. In order to improve adhesion, plasma treatment of this polymer surface prior to metal deposition is a widely accepted technique [2.22]. When the polymer is plasma treated, only a few nanometers of the surface are modified and the bulk remains untreated. The depth of metal atoms penetration into the polymeric substrate is only limited to a few nanometers, however the chemical reaction at the interface is considered very important to establish a chemical link between the metal coating and the substrate. Regarding the

^{*} The materials with low dielectric constant are called low-*k* material.

adhesion characteristics, the significance of the chemical reactivity was demonstrated at the metal/polymer interface. The metal/fluoropolymer adhesion was weak for less reactive metals such as copper and strong for reactive metals such as titanium and chromium [2.32]. In addition, less reactive metals diffuse into the polymer substrate deeper than reactive metals [2.33].

Besides the layer-by-layer structures, the polymer composite filled with metal receives special attentions because its electrical characteristics are close to metal, but its mechanical properties are similar to plastics [2.34]. The recent interest is on polymer-based, lead-free metal composite materials considering as the electrical interconnect material because of their low processing temperature, ease in process, and high thermo-mechanical performance. For instance, silver is a popular filler material since its electrical conductivity is the highest among all the metals and acceptable with its oxide. The interface between the metal fillers is pointed out as one of the major factors that could degrade the electrical property of the polymer composite [2.35].

Other applications of polymer/metal composites are continuously explored such as the development of automobile engines, which consume alternative fuels like compressed natural gas [2.36]. The polymer/metal composite material could be engineered with built-in wear resistance because the flow of polymeric material can produce auto-healing effect in damaged areas on the surface during extended service. However, the development is hindered by the lack of physical insights on fatigue, which is caused by repeated cyclic loading in dynamic condition [2.37], and fracture phenomenon.

2.1.3.1. Copper/epoxy interface

Copper/epoxy adhesion plays an important role in microelectronics for the reliability of various components. An example of copper/epoxy application is in the manufacturing of printed circuit boards. The epoxy composite serves as a dielectric layer to separate the layers of copper circuitry, while providing the necessary structural integrity of the board. For this purpose, the bonding between epoxy and copper is important [2.38]. The excellent electrical conductivity of copper gives a great advantage in integrated chip (IC) manufacturing, and epoxies are often used as a packaging material along with silicones and polyimides [2.39]. In this packaging process in ICs, one of the major problems with epoxies application is their tendency to shrink upon curing, and it can cause adhesion failure at the interface. The segmental mobility of the epoxy resin and the hardener is reduced as the free volume decreases resulting from densification. The reduced mobility hinders the proper orientation of the reacting functional group, thus further reaction is retarded at the high conversion levels. In addition, due to the different thermal expansions (Copper $15\text{--}20 \times 10^{-6}/\text{cm}^{\circ}\text{C}$, epoxy $175\text{--}225 \times 10^{-6}/\text{cm}^{\circ}\text{C}$), lateral stresses can be generated during the various processing temperature. In addition, a substrate like copper surface influences the curing process. With various environmental factors the interphase of epoxy on copper contains some levels of complexities.

The studies of copper and various epoxy systems have been done as an effort to understand the interphase. Kelber et al. [2.40] examined the interaction of an aliphatic amine, dimethylamine with copper oxide surface using electron stimulated desorption (EDX), high resolution electron energy loss spectroscopy (HREELS) and temperature programmed desorption (TPD). The results indicated preferential adsorption of amines from

an amine/epoxy mixture onto the metal oxide surface during the curing process. Kelber and Brow [2.41] analyzed diethanolamine (DEA) on copper and aluminum surfaces with X-ray photoelectron spectroscopy (XPS) to study the chemical interaction of amine-cured epoxy resin and the substrate. The protonation of amine on the substrate was studied to see the different chemical interactions. The results indicate that the epoxy-amine mixture interacts differently on copper surface and on aluminium surface. Hong and Wang [2.42] used Fourier transform infrared spectroscopy (FTIR) to detect that the presence of copper oxides does not only lower the activation energy for degradation, it also affects the degradation mechanism of the dicyandiamide (DICY) cured epoxy system. Bolger et al. [2.42,2.43] identified that the two forms of oxides (cuprous oxide, Cu_2O , and cupric oxide, CuO), which exist as a mixture on copper surfaces, behave like a defect-semiconductor. Electrons on the surface can therefore readily move from the metal substrate to the environment and oxidation continues. The cuprous and cupric ion pair can be an effective oxidation and reduction couple that can increase the decomposition of polymers. Therefore, the failure of copper/epoxy interphase can be originated from the properties of the copper oxides.

2.2. Significance of interphase

Interphase, also called interfacial region, is the intermediate phase of two materials in equilibrium. It joins two bulk phases in order for the final performance of the composite. This is the utmost important function of the interphase. On the other hand, the interface refers to the common boundary between any homogeneous phases, which are at thermodynamic equilibrium [2.44]. Considering interfaces in binary systems, Adamson [2.45] mentioned that an apparent surface of a liquid or solid is, in fact, an interface in equilibrium with another phase that is solid, liquid, or gas. The five types of interfaces exist from the definition: liquid/gas, solid/gas, liquid/liquid, liquid/solid, and solid/solid. An importance of the interface results from the fact that the internal surface area occupied by the interface is considerably large. In the case with a cylindrical fiber in a matrix, the fiber surface area is essentially the same as the interfacial area. Without the fiber ends, the surface-to-volume ratio (S/V) of the fiber is expressed as following:

$$\frac{S}{V} = \frac{\pi dl}{\frac{1}{4}\pi d^2 l} = \frac{4}{d} \quad (2.1)$$

where d and l are the fiber diameter and length of the fiber, respectively. Thus, the interfacial area per unit volume increases as the radius decreases. As the diameter of the fiber decreases, the area fraction of the interface increases. The volume fraction of the interphase increases as well. Even small interphase regions may represent a significant portion of the matrix phase. Further looking at the geometry of the interphase, the fraction of matrix phase occupied by interphase material (V_{mi}) can be estimated in terms of interphase width (w), and fiber volume fraction (V_f) [2.46] as

$$V_{mi} = 4 \left(\frac{w^2 + wd}{d^2} \right) \left(\frac{V_f}{1 - V_f} \right) \quad (2.2)$$

Assuming 60 percent fiber volume fraction, a 6 μm diameter fiber having a 0.1 μm thick interphase, 10 percent of the matrix material could be comprised of interphase. Therefore, considering the geometry of composites, the interphase can well be a deciding factor for the properties of the entire composite.

The reinforcing fiber should not be damaged by an adverse interfacial reaction. As far as the function of the interfacial region concerns, it should transfer the applied load from the matrix to the fibers through the interface. Therefore, it is important to characterize the interphase how to be affected by temperature, diffusion, residual stresses, and so on.

Interfacial interaction and interphase play a significant role in all multi-component materials regardless of the number and the type of their components. Sometimes the composite materials are solely identified by the characteristics of the interphase. Important factors for composites are the characteristics of the components, compositions, structure and interfacial interactions. Interphases are always created in heterogeneous systems with different properties and thickness from the components. They are formed by the adsorption of the polymer on the surface of the inclusion in particulate filled polymer, by interdiffusion of the components in polymer blends, or by various chemical reactions on fibers. Otherwise, interphases are also seen in reinforced advanced composites, nanocomposites and biomimetic materials [2.47]. The function of the interphase is identical in the multi-component materials influencing interfacial adhesion.

In the fiber/matrix composites, the interfacial adhesion determines the properties of the composite. The adhesion between the fiber and the matrix material must be enough to transfer stress efficiently and effectively across the interphase [2.12, 2.13, 2.16, 2.47]. Thus, when a load is applied to the composite, the strong fiber endures as the matrix distributes and transfers the load from one fiber to the other. A stiffer interphase allows a better stress transfer due to the increased adhesion; however, the increased brittleness of the material reduces the fracture toughness of the interphase resulting in matrix cracking [2.16]. Therefore, optimizing the properties of the interphase is a crucial task for the overall quality of the composites. For example, it can be a great advantage to control the stiffness of the interphase without making it too brittle [2.13].

In the field of microelectronics, the interphase performance between interconnecting metal and the dielectric layer is of importance. The adherence of the layers is especially vital to endure the multi-step processing of IC manufacturing that includes dual-damascene lithography, etching, stripping and cleaning processes, chemical-mechanical polishing (CMP), and device packaging. For instance, because the dual-damascene stack is exposed to high shear stresses during the CMP process, any flaws at the interfaces or in the low- k film itself can lead to crack initiation and long-term reliability problems [2.48]. Dual-damascene process is explained in Fig. 2-3. In the on-going effort for the miniaturization of interconnect space, copper has replaced aluminum as a interconnect metal of choice, and low- k materials became the alternatives for SiO_2 [2.49]. Mechanical stability of the products is one of the major concerns in the manufacturing with low- k materials such as silica-based and silsesquioxane (SSQ)-based materials as well as organic polymers because the properties like Young's modulus, hardness, fracture toughness, adhesion strength are significantly different from the conventional SiO_2 layers. The problems with new materials are related to poor mechanical strength, low stiffness, adhesive fracture toughness, and low

cohesive strength. Subsequently, the stress induced by a mismatch of thermal expansion coefficients or mechanical stresses during the chip packaging process can easily lead to cracking or delamination within the on-chip metal/low- k interconnect stack [2.48, 2.50]. Therefore, the reliability of the interphase determines drastically the quality of the products.

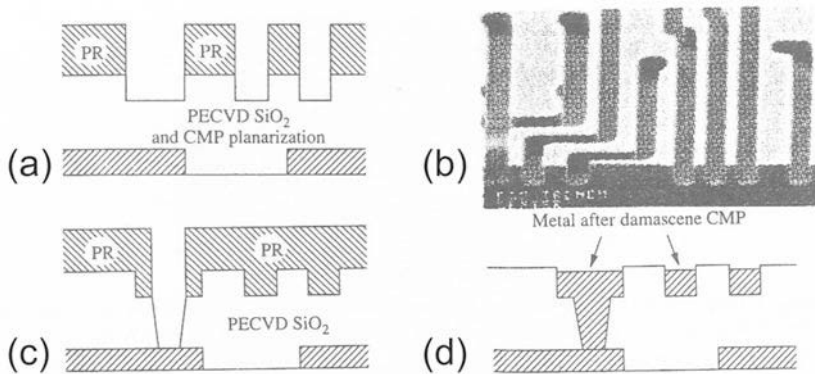


Figure 2-3. Dual-Damascene process. (a) IMD (Inter-metal dielectric) is deposited by CVD (chemical vapor deposition) and planarized by CMP. Trench is defined by first PR (photoresist) and then etched. (b) SEM of the etched trench after first PR has been stripped. (c) Vias are defined by second PR and then etched, using second PR to protect other regions of the IMD from etching. (d) Metal is deposited to simultaneously fill trenches and vias. CMP is used to remove excess metal. Repeat the sequence for the next level of metal [2.51].

2.3. Mechanisms of interphase formation

Understanding the properties of the interphase material is important not only for adhesion of two materials and the performance of the composites, but also the mechanical, electrical, and optical behavior of thin polymer films [2.52]. The following sections introduce the formation of interphases in thermoplastics and thermosets. In addition, interphase in epoxy systems is discussed as an example of a thermoset.

2.3.1. Macromolecules at interfaces

Composites with thermoplastics are processed with previously polymerized macromolecules on a solid surface. Structural accommodations of these large molecules are a complex phenomenon at the interface. The long-chain like structure of the molecule must fit into the given surface environment, or a part of the chain has to accept the adjustment of the other part with the surface barrier. In the process, a loss of the conformational freedom occurs in the interfacial region, and it is responded by a decrease in entropy [2.53]. Thermoplastics with various molecular weights are processed in the industry. The higher the molecular weight the greater is the effect in the interfacial region. Thus, the conformation loss of large molecules is higher than that of small molecules. The entropic driving force generates a surface-induced segregation. As a result, low molecular weight chains tend to move toward the surface barrier, which causes the formation of the interphase. Lower molecular weight species have a tendency to crystallize more readily than the higher molecular weight type [2.53]. The morphology in the interphase is dominated by nucleation from the surface to form spherulites. The degree of crystallinity can have a considerable influence on the interaction between two components at the

interface. Crystalline interphasical morphology could result in good adhesion strength [2.54].

2.3.2. Effects with thermosets

In the process of thermosets, monomers react to form high molecular weight polymers. There is more than one component in the reacting mixture. At the initial uncured state, the mixture is in liquid phase. It has a low viscosity, thus the molecules have high mobility. If one of the reacting components has stronger affinity towards the contacting surface than the others, a concentration gradient of that component may be created. This will cause an imbalance in the reaction stoichiometry. The surface energy of the material in contact with the mixture is primarily responsible for the relative affinity of the components. The interacting energies of the components with each other and the surface also play a role for the occurrence of the concentration gradient in the vicinity of the interface. The surface induced concentration gradient results in a different crosslink density and it will cause a different glass transition temperature than in the bulk. In the case with the interphase in thermosets with fiber reinforcement, a generalization of interphase characteristics should not be made or assumed. Drzal [2.55] has suggested that the interphase is more rigid than the bulk matrix, while Piggott [2.56] has postulated that the interphase is softer than the bulk. The studies show that the interphase may be analyzed by mechanical properties like modulus and strength. In addition, there may be different interfacial bond strengths for the interphase/fiber interface and the interphase/bulk matrix interface [2.57].

2.3.2.1. Epoxy systems

The chemical and topographical properties of reinforcement and adherend surfaces induce the adsorption of components commonly observed in epoxy systems. As the low viscosity liquid mixture of epoxy resin and the amine-curing agent is in contact with a solid surface, one component can be preferentially absorbed onto the surface. This indicates a strong thermodynamic driving force to form an interphase. When an epoxy resin is cured with an amine hardener in contact with graphite fibers, amine molecules are believed to adsorb preferentially on the fiber surface during the curing process [2.46]. This process is depicted in Fig.2-4. As the cure progresses, the mobility of amine molecules reduces along with the preferential adsorption in the vicinity of the interface. As a result, the gradient in chemical composition occurs. In order to deduce the preferential absorption, an independent study of amine/fiber and epoxy/fiber affinity can be performed. The characteristics of surface wetting comparison of amine hardener/graphite fiber and epoxy resin/graphite fiber show that amine wetted the graphite fibers much easier than epoxy resin [2.46]. The amine-epoxy system behaved in a similar way with carbon fibers. The affinity of amine hardener toward carbon fiber was stronger than that of epoxy resin, and the preferential absorption of amine onto carbon fiber was observed. The amine composition in the interphase increased.

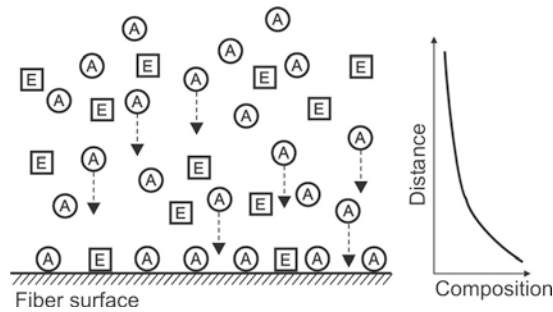


Figure 2-4. A graphic representation of amine preferential absorption onto fiber surface [2.46].

In contact with a metal surface, Rachich and Koutsky [2.58] studied the interphase formation between an amine-cured epoxy and a copper substrate. A preferential absorption of amine onto the copper surface was reported, when the mixture of epoxy resin and amine hardener was brought into contact with the copper surface and cure progresses. Kelber et al. [2.41] studied the interaction of dimethylamine with a copper surface. The result also indicated that the preferential adsorption of amines from an epoxy-amine system onto metal surface could passivate the surface and prevents subsequent bonding to the epoxy resin. Aluminum surface seems to attract amine at the low viscosity and low conversion level of the mixture. The aluminum oxide interacts stronger with amine than epoxide, thus amine adsorbed preferentially onto the metal oxide surface. Because of the preferentially absorbed amine at the surface, there was an indication that the curing of the epoxy was hindered at the interface [2.40]. In addition, this segregation effect is not only shown on the solid surface, but it has also been seen at the air surface. A low crosslink density was observed in the region near the air surface, which indicated that the stoichiometric ratio of the near-air-surface material is different from the bulk [2.59].

When the high concentration of amine occurs at the surface due to the high affinity of amine on the surface, the amine is supplied by the diffusion from the bulk resin in the immediate area near the surface. The redistribution of amine in the bulk cannot readily take place because of the increase in viscosity due to the polymerization. As the result, a compositionally separated epoxy is created. In addition, next to the high amine concentrated region, another region with a low amine concentration may exist near the copper surface owing to the migration of the amine to the interface. This leads to the existence of an intermediate amine concentration towards the bulk after the high amine concentration region [2.60]. Fig. 2-5 illustrates the concentration of the amine in the interphase with a solid surface.

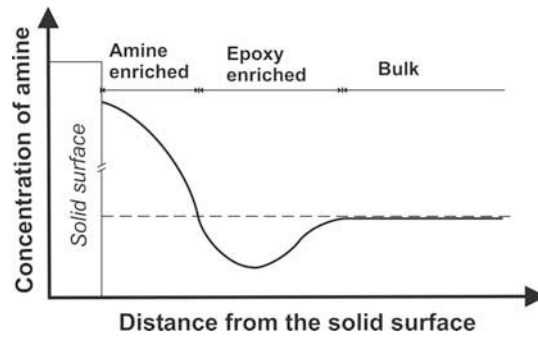


Figure 2-5. An illustration of amine concentration from a solid surface. The surface affects on the epoxy polymerization and the high concentration zone was created near the solid surface.

The studies discussed above show the preferential adsorption of amine onto the solid surface. The oxidized surface may be responsible for the high affinity of amine. In the case of a carbon surface, during the manufacturing process the surface is oxidized to improve adhesion. The chemical functionality on the surface is primarily acidic in nature (carboxylic and hydroxyl group). It may have an effect of adsorbing amine from the mixture onto the fiber surface [2.56]. On metal substrates, monitoring amine interactions with alumina, it is proposed that amine/surface interactions involve amine protonation. The surface hydroxyl groups are suggested to induce amine protonation. However, no conclusive evidence of the relationship between amine protonation and the preferential adsorption has been formulated [2.41].

The preferential absorption of a common component (e.g., amine) does not mean that the interphases have the same physical and mechanical properties. The size of the interphase can be different as well as the stiffness of the interphase. It can be softer or more rigid than the bulk. The interphase material can have different glass transition temperatures (T_g). The reaction extent of amine and epoxy can be different. The properties of the interphase are determined by the processing parameters. The surface condition of the solid surface is an important factor such as oxidation state, including the surface treatment. The nature of amine also affects the interphase properties such as aromatic, aliphatic or cycloaliphatic. In addition, other interphase determining factors are curing condition including curing temperature, resin and hardener stoichiometry, which do not only affect the interphase, but the factors are also important for the bulk material [2.61]. Interfacial bond strength can vary on assorted metal surfaces according to the stoichiometric ratio of epoxy and amine, thus the adhesion strength is also directly related [2.62].

Considering the equilibrium behavior of a liquid mixture in contact with a solid surface, enthalpic and entropic factors are responsible for the interphase formation [2.58, 2.63]. Enthalpic factors come from the interaction between the liquid components as well as interactions between these components and the solid surface. Entropic factors are the entropy of mixing and variations in entropy due to conformational effects that result from the presence of a surface. Concerning the substrate effect on adhesive, Kumines and Roteman [2.64] suggested that the mobility of a polymer in contact with a solid was different from that of the bulk polymer due to the adsorption of polymer segments onto the surface of the solid.

Racich and Koutsky studied the morphology of epoxy resins cured on various substrates with transmission electron microscopy [2.57]. The morphology of the resin was different near the interface and in the bulk. A layer of closely packed smaller nodules was observed immediately adjacent to the adherend while the nodules were considerably larger somewhat further away ($\sim 1000 \text{ \AA}$) from the interface. The closely packed small nodules near the interface were influenced by the segregation of the curing agent. Likewise, the large nodules were attributed to depletion of the curing agent in the region. Moreover, when epoxy resin is cured on metallic substrate, intrinsic and thermal stresses develop in the polymeric layer in contact with the substrate. Intrinsic stress is caused by the mismatch between the active sites of the metallic substrate and the organic network and/or the formation of the polymer network. Thermal stress occurs mostly during cooling. The mismatch of thermal expansion between the metallic substrate and the polymer induces the thermal stress [2.60]. These residual stresses result in weak adherence and induce cracks in the coating materials.

3. Epoxy Curing and Properties

In the early days the epoxy usage was only seen as varnish and adhesives [3.1], nowadays the application is broadened to various components as previously seen in Chapter 2, but the basic concept to take advantage of epoxy characteristics has not been changed dramatically. The epoxy resin consists of molecules with the reactive epoxy or oxirane group, Fig. 3-1(a), which is the main component of polymerization. The molecules of epoxy resin can be classified as any molecule with two or more alpha-epoxy groups. Through crosslinking or cure with a hardener or curing agent the resin becomes a thermosetting material, which is tough and adhesive. The dominantly used epoxy resin is diglycidyl ether of Bisphenol-A (DGEBA), Fig. 3-1(c), which is produced by the reaction of Bisphenol-A, Fig. 3-1(b), with epichlorohydrin in the presence of sodium hydroxide [3.2].

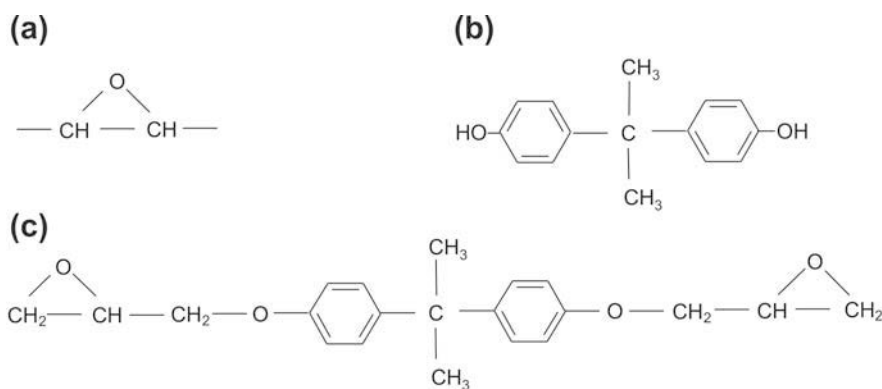


Figure 3-1. (a) Reactive epoxy (or oxirane) group (b) Bisphenol A (c) Diglycidyl ether of Bisphenol-A (DGEBA)

Epoxy resins are generally chemically stable up to 200°C, and have a long shelf life in the pure and uncontaminated state. Some curing agents execute the hardening by catalytic reaction, while others participate directly in the curing reaction. The curing reaction can be processed at room temperature with exothermic reaction, or may require external heat depending on the curing agent. The resin hardening is carried out by three different reactions: (1) direct linkage between epoxy groups; (2) linkage of epoxy groups with aromatic or aliphatic hydroxyls; and (3) crosslinkage with the curing agent through various radicals [3.3]. One of the well-used hardeners is based on amines. The crosslinking of epoxy monomers and amine hardeners generally involves the opening of the epoxide ring by reaction of amine hydrogens. The possible reactions initiated by primary amines are shown below in Fig. 3-2. Each primary amine group is theoretically capable of reacting with two epoxy groups. One will form a secondary amine with an epoxy group, Fig. 3-2(a). Then, the other is to form a tertiary amine, Fig. 3-2(b). The reactions involving secondary amines proceed at a lower rate than those involving primary amines because of steric limitations. Thus, the initial reaction is dominated by the primary amines, and then secondary amine reactions are carried out [3.4, 3.5]. The reaction rate of the two reactions from amine-epoxy is much higher than the etherification, which is reaction of hydroxyl, Fig. 3-2(c). The

etherification was observed only for excess epoxy mixtures after the depletion of amines [3.5]. As the curing reaction progresses and the glass transition temperature (T_g) approaches the cure temperature (T_{cure}), the reaction becomes less kinetically controlled and more diffusion controlled. Eventually the reaction stops without converting the secondary amine reactions. The postcure is performed at a temperature higher than T_{cure} to react remaining secondary amines with the remaining epoxide groups. As the result, T_g increases towards the postcuring temperature. Because the rate of this reaction is low, the postcure time and temperature can significantly influence the final T_g of epoxy-rich samples [3.5].

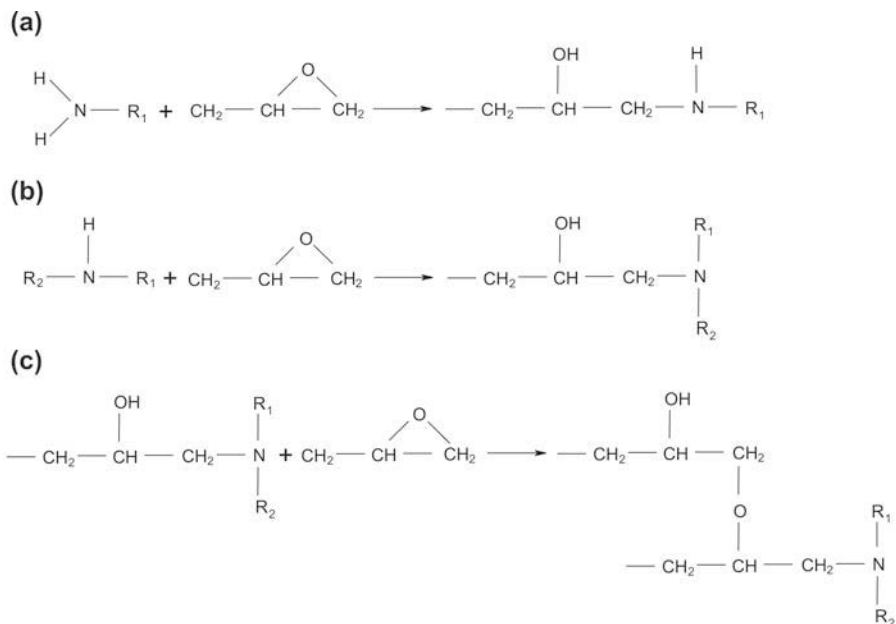


Figure 3-2. Polymerization reaction for a diepoxy-diamine system. (a) Epoxide ring-opening reaction with primary amine (b) Epoxide ring-opening with secondary amine (c) Etherification reaction between reacted and unreacted epoxy group

There are different types of amine based curing agents such as aliphatic, cycloaliphatic, or aromatic amines. Bis (*para*-amino cyclohexyl) methane and 4,4'-diaminodiphenyl sulfone (DDS) are examples of a cycloaliphatic diamine and an aromatic amine-curing agent, respectively. The final properties of cured epoxy depend on the various parameters in the curing condition. Skourlis and McCullough [3.6] examined the properties of amine-cured epoxy according to the change of the amine concentration. The epoxy in the experiments was a type of DGEBA, and the curing agent was bis (*para*-amino cyclohexyl) methane, which is a type of cycloaliphatic diamine. T_g was analyzed by differential scanning calorimetry (DSC) and modulus values as well as alternative T_g were provided by dynamic mechanical analysis (DMA). The result showed that the slope of the T_g decrease was more pronounced for the epoxy-rich region than for the amine-rich region. The different T_g values are related to the extent of the curing reaction. In addition, two different measurement techniques give different T_g values due to the different measurement frequencies. The

relationship between frequencies and temperature is an Arrhenius type of equation with T_g decreasing as frequency decreases. Thus, DSC values were always lower than the corresponding DMA values. The effect of stoichiometry can be better seen with the amine-to-epoxy ratio (r), which is defined by following equation.

$$r = \frac{2MW_e}{MW_a} \left(\frac{w_a}{w_e} \right) \quad (3.1)$$

MW_e and MW_a are the molecular weights of epoxy resin and amine curing agent, respectively, and w_a/w_e is the weight ratio of the two components (pph amine) [3.6]. Young's modulus (E) at room temperature was measured with different amine concentrations. There were often two local maxima; one at a point lower, and the other at a point higher than the stoichiometric ratio. Thus, the different amine contents influence the modulus as well as the glass transition temperature of the cured epoxy.

VanLandingham et al. [3.5] also have investigated the effect of the stoichiometric ratio utilizing DGEBA and a cycloaliphatic diamine. The results correlated well with those of Skourlis and McCullough, thus the different amine contents had an effect on E and T_g . See Fig. 3-3(a). The highest T_g was obtained for the stoichiometric sample after the postcure. It is well accepted that T_g increases with increasing degree of conversion, thus with increasing crosslink density. DiBenedetto derived an equation from theory, which only relates the shift of T_g to the degree of crosslinking [3.7,3.8]. Therefore, the various amine contents certainly influence the properties of cured epoxy. Observing the comparison of standard cured samples and postcured samples, some variation occurs within the samples with different amine contents. The epoxy cured with the stoichiometric ratio showed a great increase in T_g due to the high conversion level and low amount of unreacted molecules. The non-stoichiometric samples involved small increase of T_g after the postcure because the possible epoxy-amine crosslinking reactions already took place during the standard cure. For the amine-rich samples, because the epoxy-amine reactions had completed by the end of standard cure, the unreacted extra amine groups were oxidized during the postcure, but this oxidation did not seem to affect T_g greatly. The epoxy-rich samples showed a greater increase of T_g than the amine-rich samples, indicating that some etherification reactions occurred during the postcure. The modulus at 30°C, which is lower than T_g , was not influenced by postcure. The postcure promotes the completion of any unreacted species, and a change in microstructure and T_g is expected. However, it turned out that the change is not enough to affect the modulus. The stoichiometric sample showed the highest T_g in comparison with all the samples. The T_g decreases as the ratios move further away from the stoichiometric ratio. Inhomogeneity in microstructures of the cured epoxy with stoichiometric ratio was also reported [3.5].

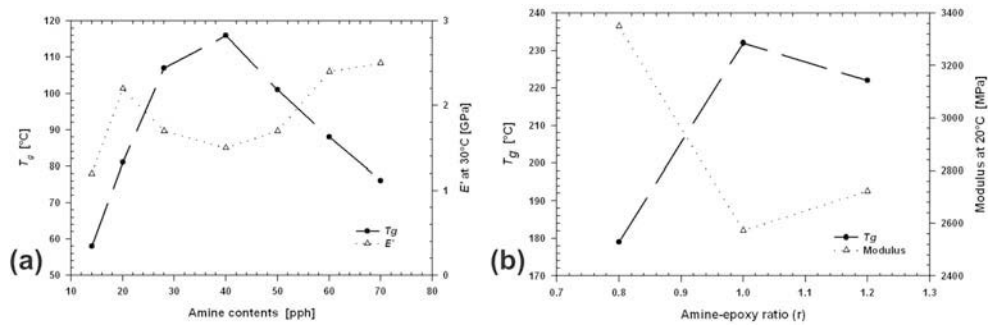


Figure 3-3. Glass transition temperature. (T_g) and modulus measured by using DMA in a variation of amine content. (a) DGEBA and cycloaliphatic diamine (EPON828-PACM 20) [3.5] (b) DGEBA and DDS (DER332-DDS) [3.9]

Meyer et al. [3.9] reported different properties of cured epoxy from the samples of DGEBA and DDS. The experiments were performed with three different ratios between epoxy resin and the amine hardener: epoxy-rich, amine-rich, and stoichiometric ratio sample. The epoxy-rich and amine-rich samples contained 20 percent more epoxy and amine respectively. In addition, the thermal process during cure was done differently to each sample. The epoxy-rich sample showed the lowest T_g as well as the widest breadth of relaxation transition, Fig. 3-3(b). This explains that the epoxy-rich sample has lower crosslink density than the others. The postcure affects the epoxy-rich sample minimally compared to the others. The modulus measurement at 20°C showed the lowest modulus at the stoichiometric ratio. The highest modulus was recorded in the epoxy-rich mixtures and slight increase of modulus was observed with the amine-rich samples. This result indicates that the properties of cured DGEBA-DDS system are determined by the ratio of the components and the condition of the cure. In addition, within the tested parameters and the tested properties, the results showed that the final properties are more sensitive to the component ratio than the thermal history. However, the influence of component ratio and thermal history needs further investigation for a generalization. Min et al. [3.10] studied the influence of the curing temperature of DGEBA-DDS system. The result indicated that T_g increases with increasing T_{cure} until it approaches its maximum glass transition temperature ($T_{g\infty}$). Murayama and Bell [3.11] studied DGEBA and methylene dianiline (MDA), and obtained various properties of cured epoxy with different component ratios at the beginning of the cure. The result showed that the highest T_g and highest storage modulus (E') at room temperature was achieved by the sample, whose mixture ratio is close to the stoichiometric ratio. This result postulated that the highest T_g was associated with the highest room temperature modulus. However, it cannot be applied to all amine-cured epoxy as the result from VanLandingham et al. displayed minimal correlation between T_g and modulus.

Besides the glass transition temperature and the modulus, the morphology of the surface can be different according to the mixture ratio and the curing condition. In addition, the morphology at the interface can be different due to the influence of solid surfaces. Earlier, it was assumed that bulk thermosets are homogeneous, however different morphological features were observed within a sample. Dusek [3.12] recognizes that the understanding of nodular structures on cured thermoset resins is significant for understanding and the control of the curing process. Morgan et al. [3.13] studied a DGEBA-DETA system and reported the morphological inhomogeneity in two different domains: regions of high crosslinked

density embedded in a low or not crosslinked matrix, and low or not crosslinked regions embedded in a high crosslink density matrix. The latter was more commonly seen from the analysis. The analysis of morphology is valuable for examining physical properties of the thermosets because there have been some theoretical indications that morphological inhomogeneities might be able to explain the lower tensile strengths of thermosets than the predicted values based on primary bond breakage or van der Waals bond breakage [3.14]. The morphological features are believed to be created in the low density state of the curing process [3.15]. Microstructures, so called nodules, on amine-cured epoxy have been seen on various surfaces such as free surface, fracture surface and etched surface [3.14]. Nodular structures were seen on cured epoxy with various amine-curing agents utilizing photo micrograph [3.16] and scanning electron microscope (SEM) [3.13,3.16]. Summarizing the experimental evidences from 1960's and 1970's, Mijovic and Koutsky [3.17] concluded that the more highly crosslinked nodules are surrounded by a lower molecular weight matrix in thermoset morphology. According to their observation of the cured surface of a DGEBA-DETA system, the size of nodules depends on the amount of amine-curing agent. A high content of amine-curing agent resulted in small nodules. The nodules were identified to be the sites of higher crosslink density because fracture initiated around nodules. A similar result was seen by Cuthrell [3.16], i.e. nodules were more rigid than the surrounding materials. Furthermore, because the size of nodules was independent of postcure, it suggested that the nodules probably form prior to gelation and only the internodular matrix is affected by postcure treatments.

The relationship of nodule size and composition on amine-curing agent has also been studied. According to the previous studies [3.17,3.18], it was found that the size of nodules decreases as the content of amine-curing agents increases. Different sizes of nodules were observed in a sample. The nodules in bulk were different from the nodules on interfaces and near interfaces with a solid surface [3.14,3.18]. The nodules were significantly larger near interfaces than in the bulk. This was considered to be an indication of different composition in the interface region. The size of nodules may be related to the curing condition. Cuthrell [3.16] observed that large nodules formed near a thermally insulated surface, and small nodules formed near a thermally conductive mold surface like steel or aluminum. It was speculated that the rate of heat transfer to the sample during the initial stage of cure could have affected the formation of nodules. Considering further the thermal effect of the nodule formation, Lüttgert et al. explained the nodule formation process in terms of a nucleation reaction. The exothermic nature of epoxy curing reaction with amine was considered the driving force of the reaction. The heat propagation of the exothermic reaction from the initial reaction sites increases the reaction rate in the close vicinity of the spontaneous reaction, where the first crosslinking reaction occurred. The growth of a crosslinked cluster is completed when it meets the front of another growing cluster. Since the probability of a spontaneous crosslinking reaction increases with the temperature, the density of reaction nuclei is increased and the average size of the cluster is reduced at higher curing temperature.

Even though considerable effort has been made to understand the morphology of crosslinked thermosets, more studies are necessary to fill the gap of understanding. Dušek [3.19] claimed that he has not seen a correlation between the nodular structure and the degree of crosslinking, nor has he seen a correlation between nodule size and crosslinking

density. In addition, the majority of studies have been conducted with electron microscopy, and it is likely that nodules were affected by the interaction of electrons or other ionic particles with the material exposed [3.16]. On the other hand, VanLandingham et al. [3.5] reported somewhat different results from the previous findings. They observed nodules on the surface of cured epoxies with scanning force microscope in terms of the amine contents by analyzing free surface and etched surface. The analysis of size distribution of morphological features implied that the epoxy with high amine content creates larger nodules than the sample surface with low amine content. This does not correlate with the previous studies by SEM. Undoubtedly, more work is required to construct a generalized concept. Furthermore, recognizing the significance of thermoset morphology, SFM can further help the analysis to expand the understanding of crosslinked thermosets.

4. Experimental Techniques

4.1. Scanning Force Microscopy in Force Modulation Mode

The principle investigation technique of the experiments, scanning force microscopy (SFM), is described in this section. First the basics of SFM are introduced in terms of topography analysis. Then, a mode of SFM to determine the local mechanical property in terms of stiffness, namely force modulation mode (FMM) is explained in detail.

4.1.1. Fundamental principals of Scanning Force Microscopy

Scanning force microscopy is nowadays one of the most inspiring methods to analyze surfaces owing to its irreplaceable characteristics as a surface analyzer. At the invention of this technique in 1986 [4.1] it is originally named *Atomic Force Microscope (AFM)* by the inventors, but now both *scanning force microscope* and *atomic force microscope* are used interchangeably. The development of the microscope has been extensive in many numerous directions, but different applications are still sought as the SFM development continues. Depending on the research objectives, the setup of analysis can be flexibly adjusted by a researcher and the sample surface needs not to be electrically conductive as it is often required for other analytic methods such as SEM.

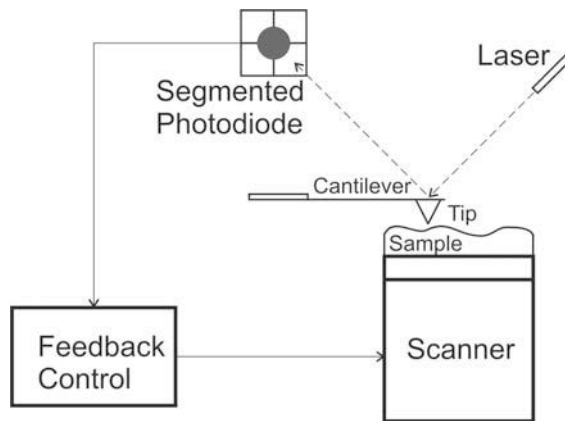


Figure 4-1. Schematic of the scanning force microscope.

The high resolution is one of the most attractive features of SFM in the analysis of surface topography. It can reproduce surface topography with a lateral resolution of less than a few nanometers and a vertical resolution of better than 1 Å [4.2]. SFM can be considered as a method in between scanning tunneling microscopy (STM) and stylus profilometry. The tunneling current of STM is replaced by the force between tip and sample which provides the necessary measure of the tip-sample contact. In the profilometry analysis, it is required to have a smooth and well-defined tip, however, in SFM it is advantageous to have the tip apex as sharp as possible [4.3]. As the tip on the micro-cantilever, Fig. 4-2, scans in contact across the surface of the material, the cantilever moves vertically according to the surface height, and it also bends laterally according to the surface friction. The both movements are captured by recording the activity of the laser beam, which is reflected from

the back of the cantilever. A feedback control is employed to keep the z-level of the cantilever constant by adjusting the piezo-scanner level. This is another feature, which differentiates SFM from profilometry, which operates without topography feedback control. Recording the change of the z-level of the piezo-scanner, the topography image is obtained. Besides the topography, other images are simultaneously acquired: the force image is the vertical bending of the cantilever, which is used as input signal for the feedback control, and the lateral force image shows the cantilever torsion. Other than the above mentioned images are possible depending on the software ability and the setup. For example, the amplitude image in FMM, which will be described in the next section, shows the local stiffness of the surface.

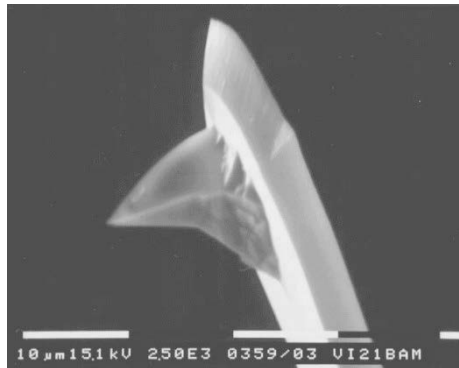


Figure 4-2. A typical SFM micro-cantilever used in FMM analysis: POINTPROBE® FMR by NANOSENSORS GmbH, Wetzlar-Bankenfeld, Germany; according to the manufacturer, resonance frequency of 75 kHz, force constant of ~2.8 N/m, radius of curvature of the tip apex of typically <10nm.

Three different SFM systems were used in the experiments. They are called ‘BerMad’, ‘NanoLyser’, and ‘Explorer’, which are all manufactured by different companies and institutions. Thus, each system has its own uniqueness. According to the sample geometry and the interest of the analysis, one should carefully select which system will be used. A researcher usually considers the scan size, sample orientation on the holder, software, etc. The visibility of the sample surface with the attached light microscope can be an important factor especially for the non-homogeneous surface since it eases locating the tip at a certain spot on the surface such as is needed for the interphase characterization. The characteristics of the systems are summarized in Table 4-1.

* NANOSENSORS GmbH is integrated into NanoWorld AG, Neuchâtel, Switzerland as of October, 2002. NANOSENSORS™ is now a trademark of NanoWorld AG.

Table 4-1. Comparison of SFM systems used in the experiments.

	<i>BerMad</i>	<i>NanoLyser</i>	<i>Explorer</i>
Manufacturer (Year)	Nanotec Electrónica S.L. (1998)	Triple-O Microscopy GmbH* & Univ. Wuppertal (Prof. Balk) (2002)	Topometrix* (1997)
xy-scanner range	13.50 μm	75.0 μm	120 μm
z-scanner range	$\sim 5 \mu\text{m}$	$\sim 7 \mu\text{m}$	12 μm
Sample positioning and adjusting	Flat (2D)	Tilted (3D adjust with a tilt angle)	Flat (2D), 3D with home-made table
Scan component (sample or cantilever)	Sample	Sample	Cantilever
Software	WSxM	QuickScan v2.1	Topo-SPM
No. of max. images during scanning	10	12	4

*The companies do not exist any longer. Topometrix became a part of Veeco Instruments.

4.1.2. Theory of Force Modulation Mode

The force modulation mode (FMM) is introduced to analyze the variation of local surface elasticity [4.4]. It is one of numerous dynamic modes (i.e. atomic force acoustic microscopy, scanning local acceleration microscopy (SLAM) [4.5], pulsed force microscopy [4.5,4.6], ultrasonic force microscopy [4.7], etc.), in which the cantilever or the sample surface is vibrated. Unlike the Tapping Mode™, which utilizes the resonance frequency of the cantilever in order to obtain the large amplitude of the cantilever, FMM is mostly operated with a frequency well under the resonance range of the cantilever, so the amplitude is small and the tip is always in contact with the sample surface. Therefore, it is a contact mode technique. The amplitude displacement can be introduced to the cantilever or the sample surface during FMM operation. Through the stiffness of the cantilever, the displacement modulation translates to force modulation. The vertical displacement modulation in z-direction results in modulated compressive loading of the tip-sample contact. The dynamic response of the cantilever reflects the respective stiffness of the tip-sample contact. The position change of deflected laser beam off the backside of the cantilever is traced to recognize the physical characteristics of materials. When the same force is applied to the sample surface, a soft area deforms more than a stiff area, and thus the cantilever deflection is less over a soft area [4.4,4.6], Fig. 4-3. Therefore, capturing ability of the cantilever deflection is important, and it is also directly related to the sensitivity of the measurement. The lock-in technique can be employed for the signal recovery. Utilizing a dual-channel lock-in amplifier, both amplitude and phase of the response signal can be captured. Furthermore, via variation of the modulation frequency, rate-dependent behavior of the surface material can be investigated. As an alternative to the amplitude of dynamic cantilever deformation, the tip-sample stiffness can be calculated from the shift of the resonance frequencies of the cantilever [4.5].

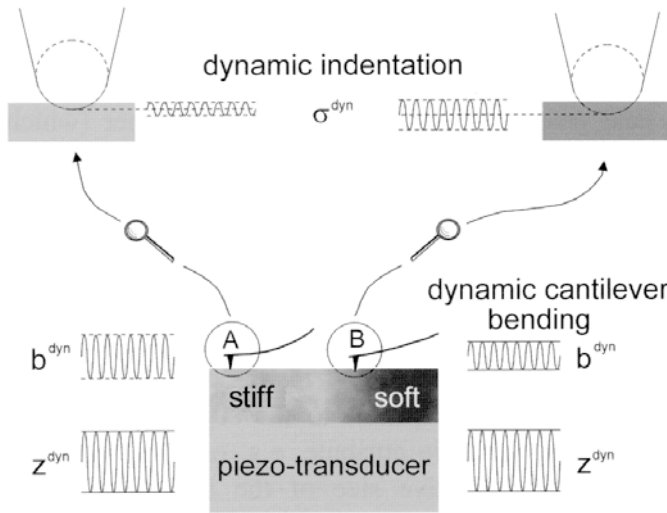


Figure 4-3. Illustration of the tip contacting stiff and soft surface [4.8].

Precisely reviewing the SFM process in FMM, the sample is placed on the modulating sample holder, which generates the excitation with a frequency lower than the resonance frequency of the cantilever. For example, the modulation height (Δz) can be created by using a piezo-transducer, and its amplitude and frequency can be controlled by a synthesized function generator. As the cantilever scans across the modulated sample surface, the tip, which is in contact with the surface, indents the surface with different depths according to local elastic conditions of the sample surface. Because the indentation depths (σ) are different, the displacements of the cantilever (Δb) are various. Thus, the force exerted on the cantilever (F_c) is different. If the tip cannot penetrate into the sample because the surface is extremely stiff, the amount of the surface modulation will be the same as the bending of the cantilever (Δb). However, because the tip indents into the sample surface, the cantilever bending is always smaller than the surface modulation (Δz). In other words, the sum of the cantilever bending and the tip indentation equals to the surface modulation:

$$\Delta z = \Delta b + \sigma \quad (4.1)$$

The mechanism of the cantilever and the tip-sample contact can be depicted as a series of two springs, one representing the cantilever stiffness (k_c), and the other representing the tip-sample contact stiffness (k_{ts}) (See Fig. 4-4). And, when the cantilever stiffness is k_c , the force exerted on the cantilever (F_c) is given by

$$F_c = k_c \cdot \Delta b \quad (4.2)$$

Thus, the force exerted by the tip-sample contact can be expressed as

$$F_{ts} = k_{ts} \cdot \sigma \quad (4.3)$$

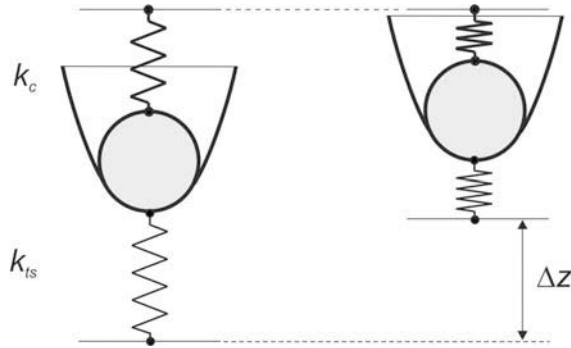


Figure 4-4. Two-spring model [4.9].

Because the modulation frequency of the sample surface is much lower than the resonance frequency of the cantilever, the forces exerted on the cantilever and by the tip-sample contact are equal at each contact point. In addition, it can be assumed that the tip itself is not elastic since it is much smaller than the sample and the scale of the exerted forces are also much smaller than the force, which is required to squeeze the tip material. Therefore, from the relationship of the forces and Equation (4.1), the stiffness of the tip-sample contact is derived:

$$k_{ts} = k_c \cdot \frac{\Delta b}{\Delta z - \Delta b} \quad (4.4)$$

The tip-sample stiffness (k_{ts}) is determined by the interaction between the tip and the sample surface. The alteration of the tip-sample contact area changes the tip-sample stiffness. In addition, the reduced modulus affects the stiffness measurement. In other words, the tip-sample stiffness is proportional to the radius (a) of the contact area as well as to the reduced modulus (E_r). Assuming a purely elastic contact, a Hertzian contact is applied while the surface force is not taken into account. Thus, when no plastic deformation occurs, according to the Hertz model [4.10,4.11] the normal contact stiffness of tip-sample (k_{ts}) is expressed as

$$k_{ts} = 2aE_r \quad (4.5)$$

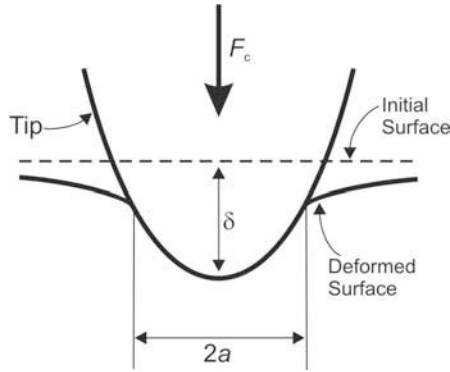


Figure 4-5. Illustration of the tip apex in contact with surface.

The reduced modulus (E_r) is obtained by the Young's modulus of the tip (E_t) and the sample material (E_s), respectively. When the Poisson's ratio of tip and sample are ν_t and ν_s , respectively, E_r is given by

$$\frac{1}{E_r} = \left(\frac{1 - \nu_t^2}{E_t} + \frac{1 - \nu_s^2}{E_s} \right) \quad (4.6)$$

while the radius of contact (a) is related to the indenter load (F_c), the tip apex radius (R), and the elastic properties of the contacting materials:

$$a = \left(\frac{3}{4} \cdot \frac{RF_c}{E_r} \right)^{\frac{1}{3}} \quad (4.7)$$

The contact models by Hertz or Johnson-Kendall-Roberts (JKR) assume that the contact radius (a) is much smaller than the radius of curvature (R) of the apex of the tip [4.12]. There are several models used to develop relationships between the measurements and mechanical properties. They describe the contact between two elastic materials. The Hertzian model portrays two elastic spheres of radii R and R' , which make contact at a point. Assuming R' is extremely large (i.e. ∞), it can be seen as a sphere of radius R indenting a flat surface. At the loading, the surface deforms such that the radius of contact (a) increases with the amount of penetration (σ) according to the Hertzian relation, $a = (R \cdot \sigma)^{1/2}$. When the load is removed, the contact area decreases back to the initial point [4.10,4.13].

The force in the perpendicular direction by the interaction of the cantilever against the local surface elasticity through the tip is transferred as cantilever displacement. (Strictly speaking, the cantilever is tilted about 10–14°, thus the force is not perfectly perpendicular to the surface.) The displacement is captured by the segmented-photo diode as the laser beam is reflected off the back of the cantilever. The captured signal (U_{in}) is fed into a dual-channel lock-in amplifier and separated into real part (U_R) and imaginary part (U_I), which correspondingly represent amplitude (U_A) and phase shift (U_ϕ). The relationship between

them is $U_A^2 = U_R^2 + U_I^2$. The stiffness image is generated from the measured amplitude signal. The cantilever displacement (Δb) is calibrated for the input signal (U_{in}), which is captured by the photodiode, and the relationship is given by

$$U_{in} = C_{spd} \cdot \Delta b \quad (4.8)$$

where C_{spd} is the slope between U_{in} and Δb . When the sample surface is assumed to be very stiff, the tip will not be able to penetrate the sample surface ($\sigma = 0$), and the vertical modulation of the sample surface will be equal to the cantilever displacement ($\Delta z = \Delta b$). The calibration can be done, for example, using a very stiff surface like stainless steel, and C_{spd} can be calculated from U_{in} and Δz . The displacement can be measured, for example, by interferometry. In the same way, the piezo modulation can be calibrated. The relationship is expressed with input voltage (U_{exc}), piezo displacement (Δz), and the slope of the two (C_{piezo}) is given by

$$U_{exc} = C_{piezo} \cdot \Delta z \quad (4.9)$$

In applying equation (4.8) and (4.9), the stiffness of the tip-sample contact can be rewritten from the equation (4.4) as following

$$k_{ts} = k_c \cdot \frac{\frac{U_{in}}{C_{spd}}}{\frac{U_{exc}}{C_{piezo}} - \frac{U_{in}}{C_{spd}}} \quad (4.10)$$

In order to apply Equation (4.10), the spring constant of the cantilever (k_c) has to be known, and it can be obtained by several different ways. One method is by using a calibrated cantilever. The cantilever with unknown spring constant is placed over the calibrated cantilever. By applying a load to the upper cantilever and from the known spring constant of the lower cantilever, the unknown spring constant can be calculated. Also, the spring constant can be calculated from resonance frequency and the amplitude of the cantilever.

The input signal (U_{in}) is still unknown since the amplitude image and the phase shift are from real part and imaginary part, respectively. In order to find out the original signal from the measured amplitude signal, the setup of the lock-in amplifier and the equation given by the manufacturer are used. For example, for SR830 DSP Lock-in Amplifier (Stanford Research Systems, Sunnyvale, USA), U_{in} is calculated as

$$U_{in} = \frac{sens}{10V} \left(\frac{U_A}{exp} + 10V \cdot offset \right) \quad (4.11)$$

where *sens*, U_A , *exp*, and *offset* are sensitivity, signal of the amplitude, expand factor, and offset percentage, respectively [4.14].

4.2. Depth-sensing Indentation

Local mechanical properties like hardness and modulus of homogenous and heterogeneous surfaces can be analyzed with a depth-sensing indentation (DSI) system. At the event of the indentation, it is able to measure depths of penetration with nanometer resolution to around 1 or 2 μm . This scale gives great advantages to perform measurements on a typical thin film without the influence from the substrate. There is a variety of indenter geometries in common use, but the two most popular ones for sub-micron testing are the sphere and the three-sided pyramidal, also called Berkovich, indenter. Commonly the analyses are done in sub-micron scale to extract elastic modulus and hardness of the film specimen material from experimental readings of indenter load and depth of penetration. Load and depth of penetration are recorded as load is applied from zero to an assigned maximum, and then from the maximum load back to zero. A residual impression will remain on the surface, if plastic deformation occurs. However, the impression is too small to be measured by an optical technique. The area of contact can be indirectly obtained from the penetration depth and the shape of the indenter. Thus, the mean contact pressure can be estimated, and therefore also the hardness of the surface material. In the process of removing the load, the material attempts to regain its original shape, but in case of plastic deformation the full recovery is not possible. However, some degree of original shape is recovered by relaxation of elastic strains within the material. An analysis of the initial portion of this elastic unloading response gives an estimate of the elastic modulus of the indented material [4. 15].

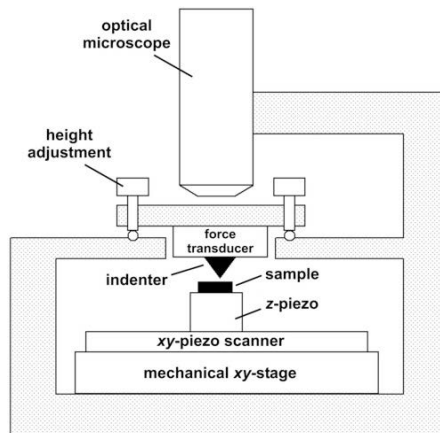


Figure 4-6. Instrumental setup of the depth-sensing indentation.

The DSI system used in the experiments is combined with a scanning device, which allows precision positioning of area of interest and topographic imaging. A diamond indentation indenter is attached to a force transducer (TribolIndenter, Hysitron Inc., Mineapolis, USA), which is mounted to the upper side of the frame, which contains the scanning unit. The height and the angle of the force transducer and the indenter are adjusted with three precision screws. A z-piezoelectric actuator with a maximum displacement of 24 μm is placed on a piezoelectrically driven xy-scanning stage with the maximum displacement of

175 μm . Initial positioning of the indenter is done using optical microscopes. The shape of the indenter consists of the Berkovich geometry, which is a three-sided pyramid with an opening angle of 136° . Although the indenter is with a wide angle, the surface image is in reasonable quality. For example, plastic deformation of epoxy can be easily recognized.

4.3. Electron microscopy with Energy Dispersive X-ray analysis

Two techniques in the area of electron microscopy are introduced. One is scanning electron microscopy (SEM) and the other is transmission electron microscopy (TEM). The energy dispersive X-ray analysis (EDX) is often integrated for elemental analysis in electron microscopy, where the electron beam is used to eject the inner electrons. An example is found in the experiments: a curing agent with sulfur, which is an element readily detectable by EDX, is used in order to verify the local concentration of the curing agent near the interface. Fig. 4-7 shows the comparison of SEM and TEM, and how the interfacial region is analyzed in the case of fiber-matrix composites.

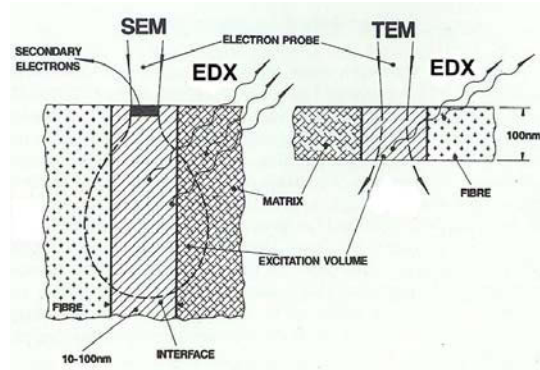


Figure 4-7. Illustration of electron beam for EDX in SEM and TEM.

4.3.1. Scanning Electron Microscopy

The scanning electron microscope is designed primarily for producing high resolution electron images of the surfaces of bulk specimens. The resolution is depending on the diameter of the electron probe (see Fig. 4-7) [4.16], and minimizing the spot size of the primary beam is important to achieve a good resolution. Surface structures are viewed with resolutions of typically 1–20 nm [4.17]. Besides a good lateral resolution, it has the ability to produce high depth of field, thus three-dimensional impression of the sample topography is a great feature of SEM. To avoid electric charging by the electron beam, the sample must either be electrically conductive or a thin metal layer needs to be applied. The emission of the secondary electrons is achieved by the primary electrons from the beam source. Because these secondary electrons have low energies (~ 20 eV), only the ones close (~ 1 nm) to the surface can escape from the sample [4.17]. This makes SEM highly surface sensitive. The image is produced by displaying the intensity of the secondary electrons from the detector versus the position of the primary beam on the sample. The detection is done in a high vacuum environment ($\sim 10^{-7}$ mbar), so that the electrons are not scattered by gas molecules. Thus, the sample is inside of high vacuum chamber. However, in the environmental scanning electron microscopes (ESEM), the sample can be placed at a gas

pressure up to 30 mbar, and the image can be still produced. The difference from the normal SEM is that the sample chamber with the detector is separated from the rest of the instrument by pressure-limiting apertures. The instrument used in the experiment is ESEM XL30 (FEI-Philips, Hillsboro, USA). It was not only used for the element analysis with EDX, but it is also utilized in electron beam lithography (EBL) (See 5.4.1.2. for the description of EBL).

As far as X-ray analysis goes, the electron scattering, also called the matrix effect [4.18], has to be carefully considered. Even though the electron probe size of 7–10 nm is employed, the detected X-rays may come from a region around 1–2 μm in diameter due to electron scattering in the bulk of the specimen [4.19], as shown in Figure 4.6. The scattering effect is a function of the voltage of the beam and the atomic number of the element. In SEM, it is important to note that the X-ray spatial resolution is larger than the image resolution; any unobserved inhomogeneities below the surface will contribute and result in misleading information of the spectrum, but in thin specimens the scattering is very small and X-ray resolution may approach image resolution [4.19]. In order to eliminate the scattering effect, the sample in the experiment is tested also with TEM, which is introduced in the next section.

4.3.2. Transmission Electron Microscopy

The resolution limit imposed by the penetration and scattering of electrons in a solid sample may be overcome by using a thin specimen. The specimen preparation is the major drawback of transmission electron microscopy (TEM), but the resolution is better than SEM. TEM is usually used to study the internal microstructure and crystal structure of samples, which are thin enough to transmit electrons with relatively little loss of energy. The thickness of the specimen is usually in the range of 20–300 nm. It provides surface sensitive diffraction data and images, and associated analytical capabilities through X-ray and electron energy loss spectroscopies. In addition, images and diffraction patterns may be formed in the reflection mode, off smooth surfaces or facets [4.20]. Because the electrons have to pass through the entire specimen, TEM cannot be called a surface sensitive method [4.17]. It needs to be ensured that the surface of the specimen investigated by TEM is equivalent to those studied by surface analysis. TEM is suitable to analyze interphase on the free surface and the bulk. Limiting scattering of electrons, the electron beam can be focused to several nanometers. Utilizing the high resolution, an interphase between two bulk materials can be investigated. Combining with EDX, the element analysis can be also done. The previously mentioned sulfur detection is later discussed in detail. The instrument used was FEI 800xP (FEI-Philips, Hillsboro, USA), and it is integrated with EDX.

5. Analyses of Surface and Interphase

5.1. Stiffness measurement with Depth-sensing Indentation

Depth-sensing indentation (DSI) was applied for an attempt to study the interphase in cured epoxy between the copper and the bulk epoxy. A silicon wafer was used as the substrate to prepare the sample with the interphase between epoxy and copper. First, copper was deposited on the substrate by physical vapor deposition (PVD) with a thickness of ~ 500 nm. Then, the epoxy was placed on top of the substrate, which was partially covered with copper. The epoxy resin was DER332 (Dow Chemical), which is a DGEBA based epoxy resin with the epoxy equivalent weight of ~ 174 g/mol. The curing agent was DDS (Fluka Chemika), which is 4,4'-diaminodiphenylsulfone. After the cure, the sample was removed from the substrate. The copper remains on epoxy and the modulus of the sample was examined (See Fig. 5.1-1).



Figure 5.1-1. Illustration of the sample preparation and analysis with DSI.

The load of DSI can be varied, and $10,000 \mu\text{N}$ was first applied for the maximum load of the indentation. The area around the interface was studied in order to recognize the different stiffness of bulk epoxy, interphase, and the copper surface. The indentation was performed in various locations starting at close to $100 \mu\text{m}$ away from the interface to the interface since it was not sure how wide the interphase was. From the indentation the reduced modulus (E_r) between the tip and the surface was acquired. During the initial attempts the difference of the moduli in bulk material and the interphase could not be measured. A slightly higher E_r was measured on the copper surface than the epoxy surface. There are several possible reasons that the interphase was not recognized. The interphase could be very small, so that the sensitivity of DSI was not able to catch the subtle difference of moduli between bulk epoxy and the interphase. The diameter of an indent was greater than $6 \mu\text{m}$ in lateral direction. Thus, when the interphase is smaller than $6 \mu\text{m}$ from the interface, DSI will not be able to locate the interphase from the difference of moduli in this sample. In addition, the depth of the indentation matters. When the surface is too deeply indented, it will be out of the interphase region and the bulk material influences the measurement. Since the thickness of copper was ~ 500 nm, an indent with a depth less than 500 nm next to the copper will stay within interphase in normal direction, when the tip does not touch the copper. The load of $10,000 \mu\text{N}$ created on average an indent with a depth of $\sim 1,270$ nm on epoxy and $\sim 1,180$ nm on copper-covered epoxy region. Because the indentation depth was greater than the thickness of the copper, the measured E_r did not show a great difference between epoxy and copper. The tip penetrated through the copper layer and indented the epoxy as well, so E_r was not only measured from the copper, but it was also from the epoxy. Therefore, the indentation depth affects the characterization as well as the width of the indentation. Chechenin et al. [5. 1] studied the indentation depth and the film thickness on elastic properties. They found that when an indentation depth is more than ~ 10 percent

of the film thickness, the modulus value will be influenced by the substrate. This indicates that the size of the indentation must be much smaller than the thickness of the film.

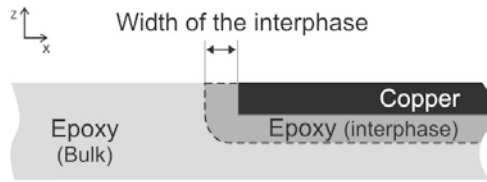


Figure 5.1-2. Illustration of epoxy interphase around the copper film.

In order to reduce the size of the indentation, the load during the indentation needs to be reduced. Therefore, indentations with reduced load were performed. Various loads were tried during the indentation near the interface in epoxy. However, the interphase, which should be created by the copper, was not found. In other words, near the interface with copper, the indentations did not show higher or lower reduced moduli compared to the bulk epoxy. Considering the indentation size, the initial contact of tip was made at less than 8 μm away from the interface. According to the measurement, the copper layer did not appear to have much higher modulus. Even at the lowest adjustable load at 100 μN on the copper layer, the indentation was influenced by the epoxy below the copper and the modulus value was affected also by the epoxy.

Table 5-1. Summary of the indentation results. Reduced modulus and indentation depth on the bulk DER-DDS and 500 nm copper film on DER-DDS.

Load [μN]	Reduced modulus (E_r) [GPa]		Indentation depth [nm]	
	Epoxy	Cu film on epoxy	Epoxy	Cu film on epoxy
100	3.13	5.30	83	55
150	3.25	4.79	117	79
300	2.93	3.95	192	14
500	3.19	3.77	252	204
1000	3.23	3.50	388	322
2000	3.28	NA	561	NA
3000	3.27	3.30	693	625
5000	3.22	3.44	886	809
10,000	3.15	3.29	1278	1183

As the load decreased, the indentation depth decreased as well. The maximum load of the DSI system was 10,000 μN , and the measurement below 100 μN showed instability. Thus, the load was not reduced below 100 μN . The interface region still did not show much different moduli with assorted loads. The indentation depth was in the vicinity of 10 percent of the copper layer when the load was 100 μN . Thus, when the interphase was wide enough, a different modulus could have been measured. Because it did not show a different elastic modulus near the interface, the interphase must be very narrow as compared to the width of the indentation.

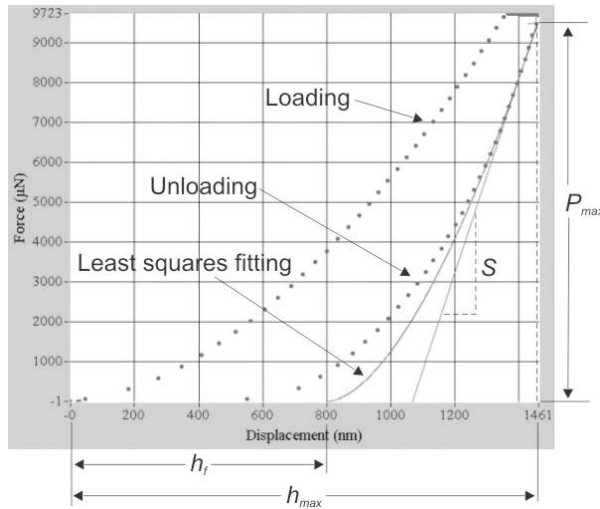


Figure 5.1-3. A typical force vs. distance curve with $\sim 9,700 \mu\text{N}$ for an indentation experiment. P_{max} is the peak indentation load, h_{max} is the indenter displacement at peak load, h_f is the final depth of the contract impression after unloading, and S is the initial stiffness.

The DSI measurement produces a force-distance curve for each indentation. The curve represents the indenter displacement according to the load. A typical load vs. displacement graph is shown in Fig. 5.1-3 at epoxy surface during loading and unloading. The elastic stiffness is acquired from the unloading. Following the theory by Oliver and Pharr [5.2], the initial part of the unloading data is:

$$P = A(h - h_f)^m \quad (5.1)$$

where P is the load, and h is the displacement. The constants A , m , and h_f are all determined by a least squares fitting procedure. The fitting was set up, so that the values between 55 percent and 95 percent of the load would be taken for the calculation. Because of the scattering at the maximum load, the data from the top 5 percent was not taken into account. The stiffness (S) is given by the value of the 1st derivative of Eq. 5.1 at $0.95 \cdot P_{max}$.

The result showed that the reduced modulus is ~ 3.1 GPa. Young's modulus of the sample can be calculated by equation 4.6, and the epoxy modulus is ~ 2.56 GPa according to the DSI measurement. The hardness of epoxy was ~ 0.18 GPa. Through the DSI analysis of this sample, the method was considered not to be sensitive enough to measure the interphase between epoxy and copper. In addition, the modulus of copper on epoxy could also not be successfully measured because of the substrate effect. The DSI system, which was used for the experiment, was not designed for hard materials like metals. Even though the DSI analysis does not seem to be an effective method to study the physical properties of heterogeneous materials with small interphases, it can be effective method for an investigation of homogeneous materials, and films.

5.2. Dynamic Mechanical Analysis

Variation of the cured epoxy modulus in relation to the amine content provides a fundamental insight to understand the interphase properties. For the EPIKOTE828-EPIKURE F205 system, the stoichiometric ratio is 58 parts of the curing agent per 100 parts of epoxy resin by weight. In the experiment to find out stiffness of the bulk samples with various mixing ratio between the resin and curing agent, the epoxy resin was cured by the curing agent with above and below the stoichiometric ratio. The samples for the SFM-FMM analysis were in the stoichiometric ratio, thus the stiffness gradient of the interphase is expected to be near the stiffness of an epoxy cured with the stoichiometric ratio. The ratios between the epoxy and amine used for the bulk samples are listed in Table 5-2. The epoxy equivalent amine ratio was mainly considered in the proportion between the resin and the curing agent. The mixtures were cured at 80°C for 2 hours. One of each sample was tested by dynamic mechanical analysis (DMA). The samples were polished to the adequate sizes to fit in the sample holder, which were in the length of 45–50 mm, the width of 4.2–5.7 mm, and the thickness of 3.1–3.9 mm. NETZSCH DMA242 (NETZSCH-Gerätebau GmbH, Germany) performed the DMA with a temperature range from –170 to 170°C at various oscillation frequencies. The sample holder was the three-point bending holder, which clamps the ends of the sample and oscillation is applied in the middle of the sample. The length of the holder was 40 mm and the oscillation was in the middle at 20 mm.

Table 5-2. Epoxy resin (EPIKOTE 828) and curing agent (EPIKURE F205) ratios of samples for DMA. (pph: parts per hundred by weight)

Epoxy equivalent amine ratio (r)	Mass [g] EPIKOTE828	Mass [g] EPIKURE F205	Amine content [pph]
0.5	31.0	9.0	29.0
0.6	29.7	10.3	34.7
0.7	32.0	13.0	40.6
0.8	24.0	11.0	45.8
0.9	29.6	15.4	52.0
1.0	25.3	15.0	59.2
1.2	23.9	16.6	69.5
1.3	22.9	17.3	75.5

5.3. SFM-based stiffness measurement in Force Modulation Mode

5.3.1. Operating under the optimal configuration

Detecting the stiffness contrast in the interphase of a composite by means of SFM in FMM mode is determined by the amplitude of cantilever, which depends on the material property. In order to exploit the performance of FMM analysis, various parameters need to be properly adjusted, including control parameters for SFM. Here, the frequency dependency of FMM is concerned. The sample is modulated by the piezo transducer with a certain amplitude and frequency. The modulation can be done at various frequencies during the analysis. However, the frequency of the sample modulation is practicable to be under the resonance of the cantilever during the FMM analysis. The reason is that the phase shift is minimal below the resonance, thus the cantilever reacts according to the sample modulation without a delay. The typical resonance curve is shown in Fig. 5-3.1.

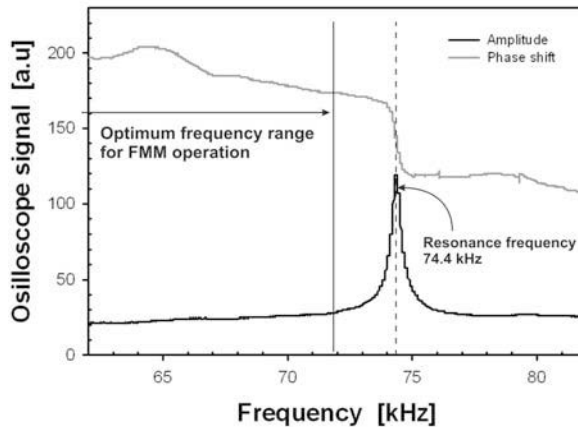


Figure 5.3-1. Frequency sweep of an SFM cantilever in air. The resonance frequency is shown at 74.4 kHz along with its amplitude response, which is shown as the oscilloscope signal and phase shift. The entire frequency range is 62 to 83 kHz.

A frequency sweep of a cantilever was performed in air, Fig. 5.3-1. The cantilever was Arrow™ FMR (Force Modulation Mode – Reflex Coating, NANOWORLD AG, Neuchâtel, Switzerland). According to the manufacturer’s description, the resonance frequency is 75 kHz, but typically within the range of 58–97 kHz. The frequency sweep indicated a resonance frequency of 74.4 kHz, which implied that the cantilever was manufactured as it was intended. This is mentioned because in general the resonance frequency often does not match with the manufacturer’s value. The amplitude of the cantilever is much lower in the region outside of the resonance than in the resonance region. The low amplitude is advantageous since the indentation will be small, such that problems like the substrate effect will be less pronounced. By achieving a stable amplitude, the FMM analysis can be optimally performed. A higher frequency than the resonance can be also utilized for SFM scanning. Scanning local-acceleration microscopy (SLAM) [5.3] uses sample modulation and contact-mode SFM similarly as FMM, but the sample is vibrated at a frequency just above the resonance of the tip-sample system. SLAM is intended for the application with stiff materials like metal matrix composites (MMC) and ceramic matrix composites (CMC). Besides the amplitude, more prominently the phase shift has to be considered according to the frequency of the modulation [5.4]. The phase shift varies negligible amount or very little below the resonance region as shown in Fig. 5.3-4. The phase changes the most at the resonance. If the scanning was done at a frequency within the resonance region, the cantilever would not react simultaneously with the modulation of the sample position, and a phase shift would have occurred. Therefore, it is important to carry out the FMM analysis at non-resonance region.

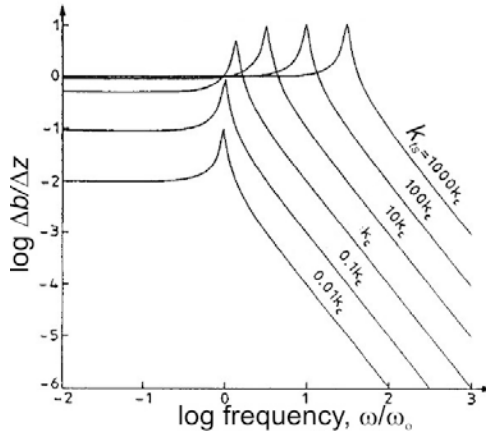


Figure 5.3-2. The ratio of cantilever amplitude (Δb) and transducer excitation amplitude (Δz) in a function of normalized frequency with the resonance frequency (ω_0) and a function of the tip-sample stiffness (k_{ts}) relative to the cantilever stiffness (k_c) [5.3].

The cantilever behaves differently in contact with materials. The cantilever behavior was modeled by Burnham et al. [5.3] to see the dependency of the tip-sample stiffness and the frequency of the modulation, Fig. 5.3-2. The ratio of cantilever response amplitude (Δd) and transducer excitation amplitude (Δz) was plotted as a function of frequency, which was normalized to the cantilever resonant frequency (ω_0) and as a function of the tip-sample stiffness (k_{ts}) relative to the cantilever stiffness (k_c). The different resonant peaks are easily recognized in the graph as the tip-sample stiffness changes. If the operating frequency is chosen in the region of the resonance, the contrast of the cantilever amplitude can be inverted. Thus, the surface with high stiffness can be identified by lower amplitude than the surface with low stiffness.

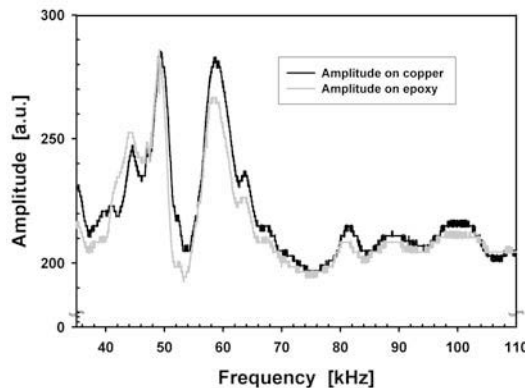


Figure 5.3-3. Amplitude of the tip response to the transducer excitation on copper and epoxy surface without scanning. The excitation frequency was from 35 to 110 kHz.

The amplitude of the cantilever is different when it is free in the air and in contact with materials, because the damping increases as it becomes in contact with materials.

Considering the behavior of cantilever amplitude on copper and on epoxy, a shift of the amplitude peak can occur during scanning the stiff material and soft material. Fig. 5.3-3 illustrates the situation when the amplitude peak is shifted because of the different stiffness of materials. In most cases, the FMM amplitude is lower on the soft material than on the stiff material. However, influenced by the properties of material, the resonance region can be shifted and the soft material can have a higher FMM amplitude than the stiff material. For example, the cantilever amplitude is higher at the resonance on the soft material than at the same frequency on the stiff material, which is not in resonance. In this case, the FMM amplitude image can show a higher amplitude in the soft material than in the stiff material.

A range of frequencies from 35 to 110 kHz was applied to the excitation of the sample, and the amplitude of the tip response is measured while the tip is in contact with copper and epoxy surface, Fig. 5.3-3. The amplitude of the tip on the copper is not always higher than on the epoxy. At the frequency where the copper amplitude curve is above the epoxy amplitude curve, the copper region is brighter than the epoxy region in the FMM amplitude image. This is the most by the case in the analysis, and the FMM configuration is setup to have the copper region brighter than the epoxy region, so that the stiffer material in the interphase also shows brighter than the softer material. On the other hand, the epoxy amplitude curve is partially higher than the copper amplitude curve. When the FMM is performed within this frequency region, the contrast is reversed. Hence, the epoxy region is brighter than the copper region, Fig. 5-3.4.

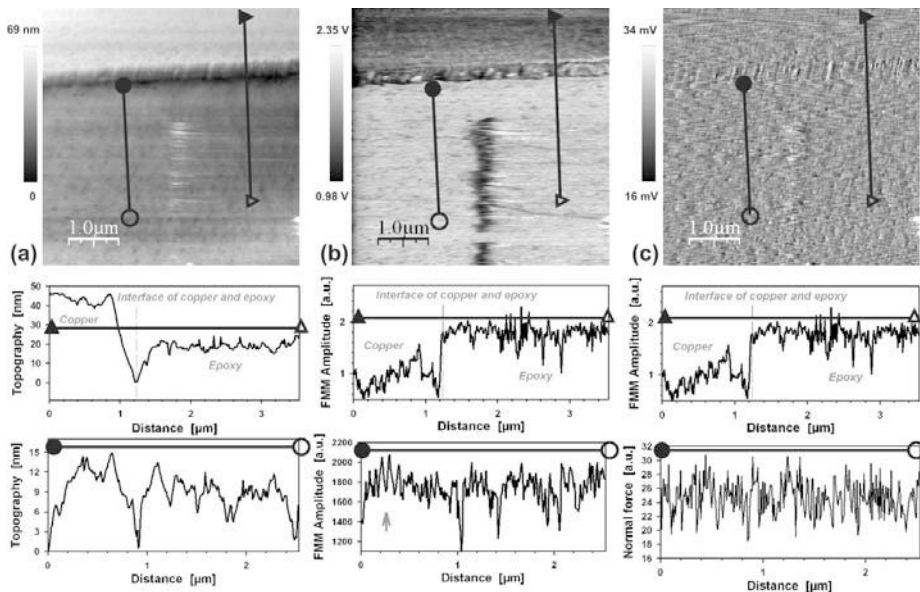


Figure 5.3-4. SFM images with a backward contrast FMM image: soft region as bright and stiff region as dark. (a) The topography shows the copper on the upper part of the image and the epoxy on the bottom. (b) The FMM amplitude image shows the epoxy as a bright region and the dark trace in the middle is an artifact generated by deformation from the previous scanning. The profile shows that the FMM amplitude is higher in the epoxy region. (c) The normal force image shows that the SFM parameters are optimal and the feedback control was well performed.

The epoxy amplitude and copper amplitude are about the same at certain frequencies. In this case, the FMM amplitude image does not clearly show a difference in contrast. The topography image, Fig. 5.3-5(a) demonstrates that the surface is very flat, and a good continuity exists in the interface region between the two materials (copper and epoxy). Thus, the FMM analysis can be well performed with the sample. The FMM amplitude image, Fig. 5.3-5(b) does not show the stiffness contrast between copper and epoxy surface because the sample excitation frequency is in the range, which does not allow for distinguishing between the different material stiffnesses. In this case, the sensitivity of FMM analysis is dramatically reduced and it is not able to detect the stiffness difference between stiff and soft materials. Fig. 5.3-5(c) demonstrates that the parameters of the feedback control were set correctly for SFM-FMM performance.

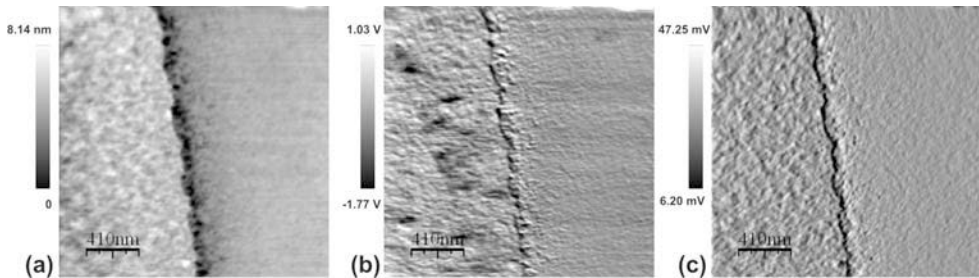


Figure 5.3-5. SFM analysis of copper and epoxy with barely any difference in contrast of FMM amplitude. (a) The topography shows the copper on the left and the epoxy on the right. (b) The FMM amplitude image does not clearly show the stiffness contrast between copper and epoxy. (c) The normal force image shows that the feedback control was well performed, thus indicates that suitable values of the SFM parameters are applied.

5.3.2. Topography induced artifacts

It is worthwhile elucidating that the FMM signal can be also affected by factors other than the local sample stiffness. As shown by Eq. 4.5, variations of the contact radius (a) will change k_{ts} as well as variations of the tip-sample modulus, which is the reduced modulus (E_r) of tip and sample. Changes of the tip-sample contact area can be caused by the sample topography both in a direct and in an indirect sense. In the direct sense, the geometry of topographic features such as hills or pits makes the contact area either to shift on the surface of the apex or to change in magnitude. Hills are convex curvature and pits are concave curvature. For instance, in pits with a radius of curvature comparable to that of the apex, the contact area will be significantly increased. The increased contact radius will result in an increased contact stiffness (see Eq. 4.5). In the indirect sense, the coupling occurs via the topography feedback. Because of the non-zero period of time, the feedback needs to adjust the cantilever height position to the topography at the position of the tip. The normal force exerted by the tip onto the surface is not perfectly constant, but exhibits some deviations from the set-point value. In the case of the tip scanning uphill, the non-instantaneous reaction of the topography feedback will lead to a slightly increased normal force which in turn results in an increased contact area. However, this second effect via the topography feedback depends on a number of parameters such as the scan velocity and the various control parameters for adjusting the performance of the feedback. Therefore, these topography-related effects are hard to be taken into account in a quantitative manner,

and serious data correction procedures will be difficult to achieve. Thus, a more pragmatic, but nevertheless rigorous approach was devised for ruling out topography-related effects on the FMM stiffness signal and the potential misinterpretation of stiffness data [5.5,5.6]. The region of analysis is limited to regions where the amount of the local surface slope angle (as measured in the direction of scanning) is lower than a critical value. This approach is motivated by the general finding that the image of normal forces resembles that of the local slopes of topography. That is, when scanning uphill, the surface slope angle is positive and the normal force is higher than the force set-point value; in reverse when scanning downhill. Moreover, also the lateral forces are affected by topography [5.2].

Analyzing a number of topography images recorded with a typical feedback performance, it was found that the maximum angles of the surface slope, which the feedback is able to adjust to with near-perfect accuracy, are $\sim|3|^\circ$ [5.5]. The images were recorded with a typical scan frequency of 1 line/s and the distance over which the slope angle, α , was calculated was $\sim 1/50$ of the scan range. According to $\alpha = \arctan(dz/dx)$, α was calculated from the slope which results by differentiating with respect to position along the scan line. Although better performance of the topography feedback may be achieved with peculiar SFM systems, in the sense of a conservative quality criterion a critical slope angle of $\sim|3|^\circ$ can be defined. Considering that low value, it seems that with this criterion also the direct contact area effects are negligible, at least in case of typical SFM tips with radius of curvature (R) smaller than ~ 50 nm. It should be noted that the image of slope angle has to be calculated from the raw topography image as measured prior to application of any software-based leveling function.

The concept is confirmed by the following example of FMM analysis on an uneven surface of an epoxy sample, Fig. 5.3-6. Considering the topography, Fig. 5.3-6(a), and amplitude images, Fig. 5.3-6(c), there is some unevenness on the epoxy surface near the upper edge of the images. For convenience the two regions of particular interest are labeled as A and B, respectively. In region A the change of height is not as dramatic as in region B. As usual, high brightness indicates high altitude and vice versa in Fig. 5.3-6(a). The FMM image shows that the amplitude did not change in region A, but there is a change of amplitude in region B. Because the amplitude is homogeneous in the rest of the image including region A except for the upper part of the image, where a lot of grain-like structures are, it seems certain that the amplitude variation in region B originates from the topographic features rather than from true stiffness variations. Fig. 5.3-6(b) shows the slopes on the surface, which were calculated from the topography image. After the calculation of slopes, a threshold value was looked for to find the critical slope from which on topography-related artifacts occur in the FMM amplitude. As visible from Fig. 5.3-6(b), the critical slope value is $\sim|3|^\circ$. It indicates that if the unevenness of the surface becomes greater than 3° or lower than -3° , contrasts are induced in the FMM image. As a result, topographic features also affect the FMM amplitude, which is supposed to contain stiffness-related information only.

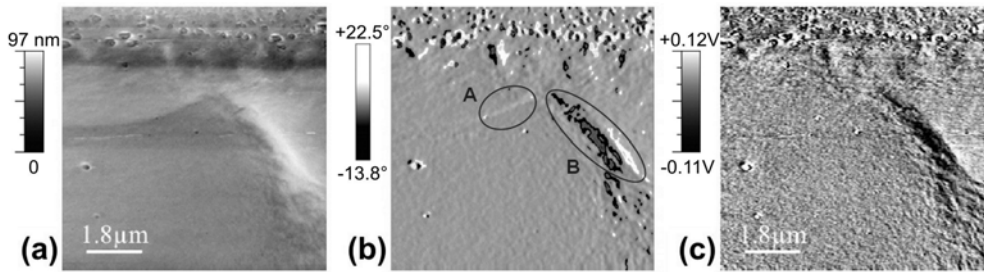


Figure 5.3-6. Effect of topography on FMM amplitude, as measured on epoxy. (a) Topography image. (b) An image of slope angles as calculated from the topography. (c) FMM amplitude image. In region B, where the slope angles exceed $+3^\circ$ or -3° , the amplitude image exhibits variations. Total height range of the topography image $z_{max}=97$ nm; cantilever stiffness $k_c\sim 3$ N/m; FMM frequency at 57.0 kHz; FMM amplitude $\sim 0.1\text{--}1$ nm [5.5].

Concerning the application of the topography criterion, some remarks should be made: First, by its nature, the above defined topography criterion is necessary, but it is not sufficient enough. Considering the feedback at a certain point of time, its performance depends not only on the topography at the current position of the tip, but also on the one it passed just before. In terms of the widespread proportional-integral-differential (P-I-D) algorithm, the I- and the D-terms account for the non-instantaneous reaction of the feedback. In particular, long-standing deviations from the force set-point value affect the feedback via the I-term. Correspondingly, at the edges of the scanned area, significant deviations from the force set-point value may occur due to topography features situated outside the scanned area but still affecting the feedback. Second, one should bear in mind that the true topography differs from the measured one. Aside from the non-perfect topography feedback, differences can result from the limited sharpness of the tip or from the non-zero compliance of the surface material. Whereas the latter two effects will not be reflected in the force image, it proves useful for checking deviations from the feedback set-point value. In addition, the lateral force signal should be inspected along with the normal force signal for topography-related force variations. Topographic slopes come along with lateral forces leading to the torsional deformations detected in lateral force mode [5.2]. The related tilt of the tip means changes of the tip-sample contact area, in particular its position on the apex of the tip. In case of severe misalignment of the optical detection scheme, torsion cantilever deformation may even give a contribution to the normal force signal.

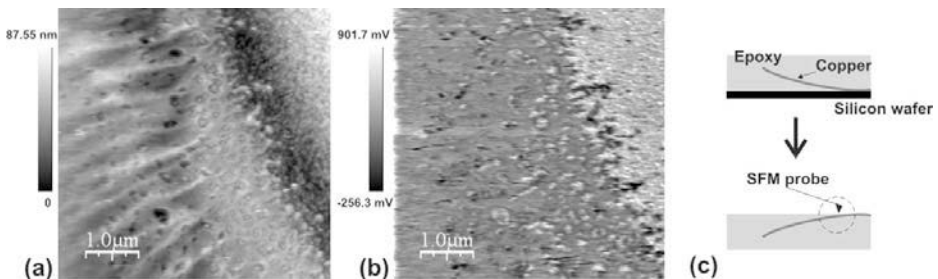


Figure 5.3-7. Wavy structures of epoxy interfacing with copper. (a) SFM Topography. (b) FMM amplitude image. (c) Sample preparation and sample shown in cross section.

As it has been discussed, the various parameters influence the SFM analysis and the FMM analysis, so the topographical limits of measurable surfaces may not be easily defined. With well-adjusted control parameters, FMM analysis can bear certain irregularity on the surface. In Fig. 5.3-7(a), the topography shows that the surface is somewhat wavy and small wholes exist in the interfacial region between epoxy and copper. It seems that the topographical condition of the surface is not optimal for the FMM analysis, but the FMM amplitude image, Fig. 5.3-7(b), represents the stiffness of the material well. The copper with higher stiffness than epoxy is shown as the bright area on the upper right corner. Because epoxy is very thin near the interface as the illustration of the sample shows, Fig. 5.3-7(c), the bright holes might be from the high amplitude influenced by the copper underneath of the epoxy. The copper layer on the silicon wafer was partially delaminated. When the mixture of epoxy resin and curing agent was applied on top of the copper and the silicon wafer, the mixture was placed in between the copper and the silicon wafer, creating a thin epoxy layer on the copper. Because the flat silicon wafer was used as the substrate, epoxy and copper formed a flat surface. After removing the silicon wafer upon curing the resin, the edge of copper, which is circled in Fig. 5.3-7(c), was examined by SFM in FMM mode. In the amplitude image, the wave-like structures in the topography were not found at all. It indicates that the unevenness did not affect the FMM analysis. The above images from the uneven surface exhibit that the FMM analysis can tolerate a certain level of local roughness in the specimen.

Due to a limited number of data channels in the software, however, in many cases the simultaneous measurement of FMM amplitude and phase, as well as normal and lateral forces is not possible. Moreover, the data evaluation procedure becomes a time-consuming task with careful consideration of all these details. Hence, application of the topography criterion seems to be a valuable approach, in particular since contact area variations in the direct sense are not reflected by force images.

The global tilt of the sample surface can easily be higher than the above defined critical slope angle of $\sim 3^\circ$, thus rendering any stiffness analysis with strict application of the topography criterion is impossible. However, parallelization between the plane of scanning and the plane of sample surface can be achieved when using a setup where the cantilever is scanned rather than the sample. In the less favorable case where the sample is scanned, these two planes are not decoupled from each other and any tilt between the plane of the sample surface and the head of the microscope will result only in a tilt of the tip. It should be noted that in the case of point-wise stiffness measurement (i.e. without any simultaneous scanning motion), the effects resulting from the sluggishness of the topography feedback are avoided. However, the contact area is still affected by the tilt of the sample surface.

When tiny dips exist on the surface, the tip-sample contact area can be increased and it induces short peaks of high amplitudes during FMM analysis. The images in Fig. 5.3-8 illustrate the surface of the EPIKOTE828-EPIKURE F-205. The topography, Fig. 5.3-8(a), shows tiny dips as small dark dots as the arrows in the image indicate some of the dips, which are commonly seen on the surface. The dark dots represent that they are lower than the rest of the surface. The arrows in the amplitude image, Fig. 5.3-8(b), denote the same locations as in the topography. When the tip scans through the dips, the FMM amplitude is increased dramatically as the bright spots in the FMM amplitude image indicate. They are artifacts from the topographic features on the epoxy surface.

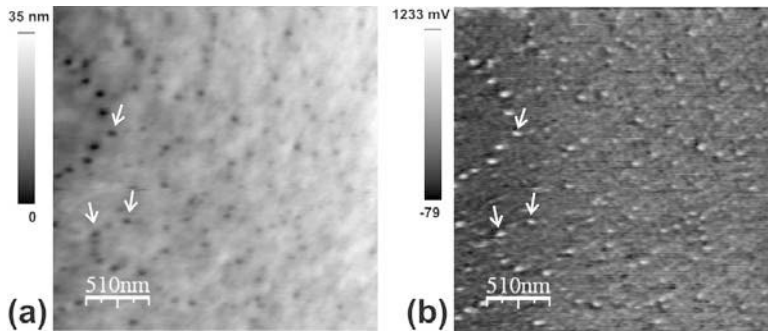


Figure 5.3-8. SFM images showing topographic artifacts in the FMM analysis due to the tiny holes on the surface. Some examples are indicated with the arrows. (a) Topography of epoxy surface. (b) FMM amplitude image.

5.3.3. Recognition of copper and epoxy surfaces

The recognition of the stiffness difference between the copper and the epoxy is a good indication that the method is valid to examine the stiffness contrast in the material. It is clear that copper is a stiffer material than the cured epoxy, so the result from the analysis can show how the FMM image looks like. As it is previously explained (See 4.1.1), high amplitude implies stiff material, and low amplitudes imply soft material. Knowing that the copper is much stiffer than the epoxy, the FMM amplitude image should show the copper brighter than the epoxy.

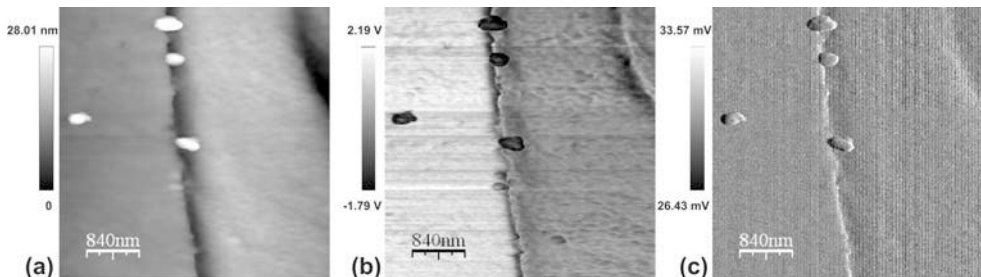


Figure 5.3-9. SFM images ($4.2 \times 4.2 \mu\text{m}^2$) of the interfacial region of copper (left) and epoxy (right) on the images. EPIKOTE828/EPIKURE F205 system cured at 70°C for 2.5 hours and post-cured at 130°C for 1 hour; (a) Topography. (b) FMM amplitude image. (c) Normal force image.

The SFM images, Fig. 5.3-9, are taken in the interface region, where the epoxy meets the copper. The cured epoxy consisted of EPIKOTE828 and EPIKURE F205. The cure was at 70°C for 2.5 hours and then it was post-cured at 130°C for 1 hour. The vertical line in the middle of the images is the interface. The copper is on the left from the interface and the epoxy is on the right from the interface. The thickness of the copper layer is ~ 500 nm and the epoxy is also underneath of the copper layer. Since the indentation depth of the SFM-tip on the surface is ~ 1 nm [5.7], the previously concerned substrate effect with the DSI analysis (See 5.1) is no longer an influential effect. The topography image, Fig. 5.3-9(a), shows the height of the surface by the brightness. The high brightness corresponds to the high surface. The height range, which is indicated by from the lowest point to the highest point, of the surface is ~ 20 nm. The scale bar of the topography image covers up to 28 nm in

order to show a better contrast of the surface. When the scale bar is adjusted to 20 nm, which is the same as the highest point on the surface, the region at the height near 20 nm will be depicted with high brightness and the region is hard to be recognized on the image. The edge of the interface, where epoxy starts, shows as a narrow dark region, and it indicates that the edge from copper to epoxy is not perfectly continuous. The four bright spots are dust particles. It is a good comparison to see how flat the surface is. The copper and the epoxy can be much better distinguished from the FMM amplitude image, Fig. 5.3-9(b), which shows the stiffness contrast. Copper being much stiffer than epoxy, the amplitude is higher on the copper than on the epoxy. High and low amplitudes are shown respectively as bright and dark area on the amplitude image. The slight discontinuity on the interface did not seem to disturb the FMM analysis because the topographically induced artifact was not generated in the region. The dust particles are shown as dark spots in the amplitude image. They might be softer than the rest of the sample, but their low amplitude signals might have been generated from the sudden height change. The normal force image, Fig. 5.3-9(c), is always an important measure for the optimal performance of the feedback control. When the cantilever bending is perfectly controlled, the image will show no disturbance and there will be no contrast. With current technology the feedback control cannot be perfect. However, the fewer features on the normal force image indicate the acceptable feedback control during the FMM analysis. The dust particles are good examples of feedback disturbance. When the height suddenly changes on a large scale, the feedback is not able to adjust the sudden bending of the cantilever. Thus, the disturbance appears in the image. This is also shown at the interface, but compared to the effects of the dust particles shows that the effect was minimal.

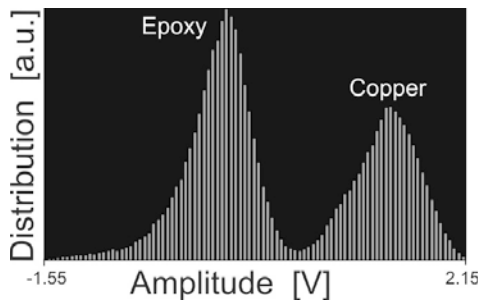


Figure 5.3-10. Distribution of FMM amplitude in epoxy and copper from Figure 5.3-9(b).

Further analyzing the FMM amplitude image, Fig. 5.3-9(b), the amplitudes distribution graph, Fig. 5.3-10, from epoxy and copper clearly shows two different peaks, which differentiate the stiffness of epoxy and copper. The range of the amplitudes is readjusted to show only the area of interest from -1.55 to 2.15 V. The amplitude of epoxy being lower than that of copper, epoxy peak is on the left side of the copper peak. In addition, the epoxy area is somewhat larger than the copper area in the image; the area of the epoxy peak is also somewhat larger than the area of the copper peak in the graph.

5.3.4 Recognition of the interphase in epoxy on copper

The stiffness of an interphase in a cured epoxy on copper was analyzed by SFM in FMM mode. The sample surface is flat and continuous between the two materials. The geometry

of the sample is important, in order to investigate the interphase with scanning force microscope. In Fig. 5.3-11, the topography and the amplitude image are shown. The cured epoxy is on the left wide area and the copper surface is on the right narrow area. In the topography, Fig. 5.3-11(a), the two different areas are easily recognizable from the interface between them. The profile of the topography of the marked area, which is $(2.6 \mu\text{m})^2$, in epoxy surface is shown below the images. The square area is parallel to the interface with the copper, in order to see the width of the interphase in the epoxy from the copper. The profile is the average values across the selected area in the epoxy. Thus, the profile of the topography is the height average, and the profile of the stiffness image, which is below the image in Fig. 5.3-11(b), is the amplitude average in the square area. The profile starts from the left side of the marked area. The unevenness of surface height is larger close to the copper than far away from the copper. It indicates that the surface geometry of the interphase in epoxy is different from the bulk. However, the local slope of the surface is very low and it is adequate for FMM analysis. The slope is also shown with the profile of the topography. The difference between the lowest point and the highest point in the profile is about 100 nm. However, the local slope is small in general. The largest slope is $|-0.15|^\circ$ in the marked area and it is well below the critical slope of 3° . In the amplitude image, Fig. 5.3-11(b), only the epoxy surface is shown in order to show the gradient of contrast. Because of the large stiffness difference between epoxy and copper, when the contrast of the amplitude image is adjusted for the epoxy surface, the copper surface is shown as just a bright area. The amplitude profile shows the variation of the stiffness in the interphase. The epoxy near the interface has a lower amplitude than the epoxy far from the interface. Likewise its stiffness is lower near the copper than far from the copper. However, at the end of the profile, the amplitude suddenly increases, and supposedly it is because the contact area between the tip and sample was increased due to a narrow and sharp discontinuity at the interface. The lowest amplitude in the profile is just outside of the interface, and then it increases over about $1.5 \mu\text{m}$ away from the copper according to the profile. It indicates that there is a lowest point of stiffness in the interphase in epoxy. The dark area, which indicates the lowest amplitude in the profile, is seen near the copper. The cause of the stiffness variation in the interphase can be a change of the relative concentration of the epoxy resin and the curing agent. And, this composition change may have been influenced by the copper surface. It is most likely that the interface induced a local preferential adsorption during the curing process. When the mixture of epoxy resin and curing agent was placed on the copper, the adsorption of either epoxy resin or curing agent may have occurred towards the copper surface, and the interphase could have been created from the different composition between epoxy resin and curing agent on the copper surface. The amplitude profile shows that the cured epoxy in the bulk is stiffer than near the copper.

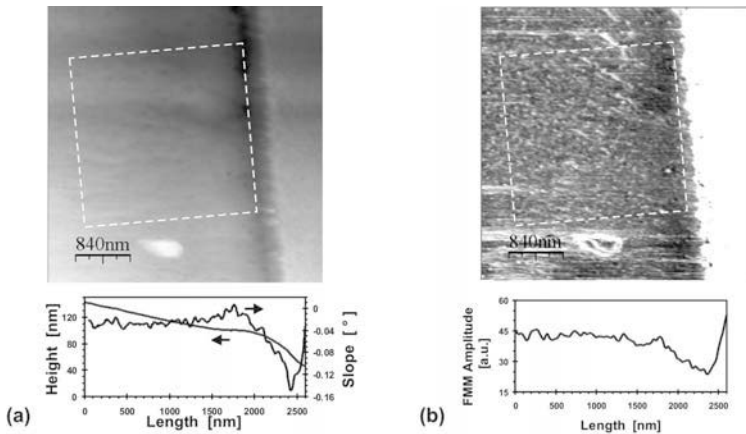


Figure 5.3-11. Interphase in epoxy between the bulk epoxy and copper. (a) SFM Topography of epoxy and copper. The graph below the image is the average profiles of topography and the slope of the interfacial region in the marked area. (b) Corresponding FMM amplitude image. The simultaneously taken FMM amplitude image shows the softer area near the interface and the average profile of the marked area is below the image.

Although the stiffness of amine-cured epoxies depends very much on the ratio of epoxy resin and curing agent [5.8,5.9,5.10], the stiffness gradient in the interphase of the cured epoxy on copper may also be caused by the chemical interaction with copper oxide [5.11]. Partial delamination of epoxy on copper surface has been already seen. It was previously reported that copper oxide causes the failure of adhesive bond between copper and epoxy. Carboxylic acids are produced at the interface with copper and it can further react with the metal surface to produce soluble metal salts. The diffusion of these salts into the polymer matrix can cause degradation.

5.3.5 Advantages of Force Modulation Mode

The SFM in force modulation mode (FMM) is especially advantageous for the sample containing a region of interest with small geometry. As was shown at the beginning of the chapter, in the case of an indentation technique when an indenter makes a large trace, it might not recognize the different physical characteristics of the region of interest. Furthermore, it is impossible to identify the gradient within the area. Considering the substrate effect and the influence of adjacent material, an indent must be much smaller than the region of the interest in order to analyze its mechanical property. For example, the depth-sensing indentation with a Berkovich indenter was shown in the characterization of the interphase between epoxy and copper. On the other hand, SFM uses a much smaller indenter with significantly less load force; subsequently its indentation is smaller. These days, the common radius of the curvature of the tip apex is ~ 10 nm with commercial cantilevers. A static normal force exerted on the sample surface is ~ 100 nN during a typical FMM analysis [5.12].

In terms of the characterization of mechanical properties, the given geometry of indenter enables investigation of a small area such as 1 to $2 \mu\text{m}^2$ or even smaller, and the gradient within the region can be profiled. This does not only make it possible to study a small region, but it can be also applied to study a thin film less than $1 \mu\text{m}$ thick, which is well

within the range of the theoretical limit. Using the high sensitivity of amplitude alteration caused by the stiffness of materials, it can be utilized to spot defects in polymer matrix composites. For example, when a small amount of the undesired polymer is placed cross the edge of the metal, it can be shown as various sizes of polymer spots on the metal near the edge. In Fig. 5.3-12 a case of copper and epoxy are shown. The copper is located at the top half of the images of SFM, and the bottom half is the epoxy. The topography image, Fig. 5.3-12(a), shows the clear indication of epoxy on the edge of copper with a thickness of $\sim 1 \mu\text{m}$. The apparent difference in the morphology between epoxy and copper, the unwanted epoxy at the edge of copper is easily seen. However, when the amount of epoxy is very small, the small islands of epoxy cannot easily be seen in the topography. Examining the FMM amplitude image, Fig. 5.3-12(b), the brightness contrast between epoxy and copper shows where the small islands are. The small amount of epoxy on the copper in the circled area does not show in the topography image. The normal force image, Fig. 5.3-12(c), validates SFM performance.

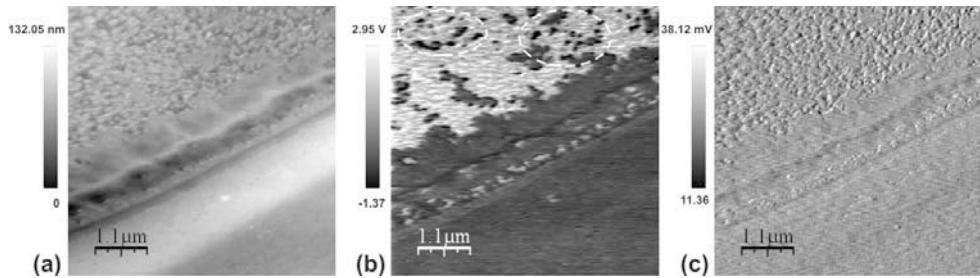


Figure 5.3-12. An example of an application of SFM-FMM to detect small polymer defects on a metal surface. (a) SFM topography. The top half is copper and the bottom half is epoxy. (b) FMM amplitude image shows small epoxy spots on copper surface. (c) Normal force image.

5.4. Preparation of epoxy/copper composite

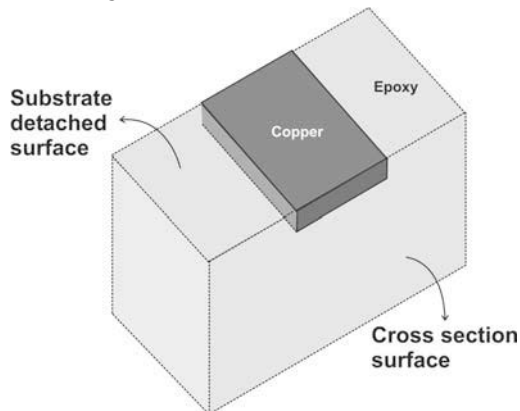


Figure 5.4-1. The orientation of the two surfaces analyzed: the substrate detached surface and the cross section surface.

The detailed description of the sample preparation procedure is discussed in this section. As it has been already discussed previously, the interphase analysis was conducted on the

surface of the copper-epoxy composite. The analysis was done on two different surfaces of the same sample. One is the substrate-detached surface, which was in contact with a silicon wafer and detached from it. The other is the surface of the cross section from the same sample, and the surface was prepared by carving with a microtome. The orientation of the surfaces is shown in Fig. 5.4-1. The difference of the two surfaces is significant regarding the substrate effect.

5.4.1. Epoxy interphase with copper microelectrodes

Several techniques were employed to prepare the samples for the interphase analysis. The overall preparation procedure is described step by step. Then, electron beam lithography, and metal evaporation and lift-off technique, which are also introduced in the procedure, are dealt in order to illustrate additional explanations of the techniques.

5.4.1.1. Preparation of substrate detached surface

As the sample preparation is illustrated in Fig. 5.4-2, the interphase of copper and epoxy is produced by a number of steps. The preparation consists of three main steps. First, the positive e-beam resist was prepared for the electron beam lithography. Second, the exposed resist was developed and the copper film was evaporated. Third, after the lift-off an epoxy system was applied to the entire area, and after curing the silicon wafer was removed to complete the sample.

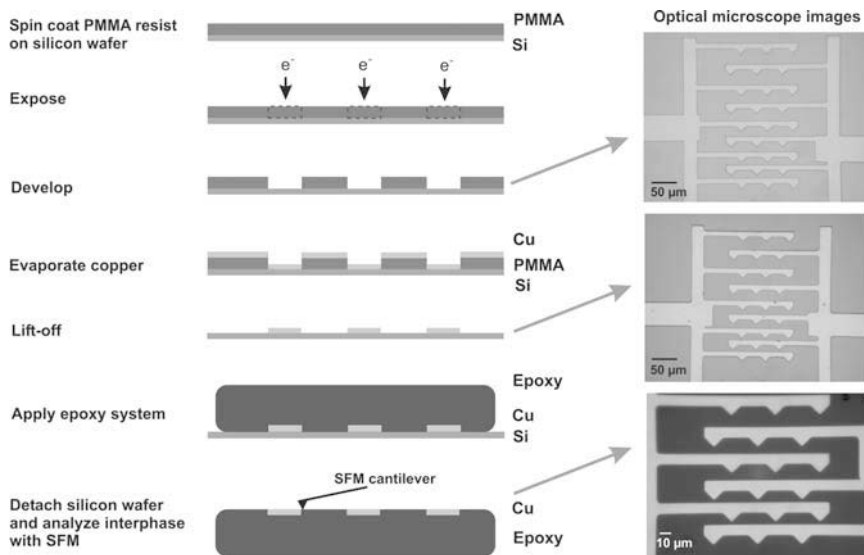


Figure 5.4-2. The sample preparation procedure of copper-epoxy interphase and the images of the sample during the preparation.

The silicon wafer was cut in pieces of 2 cm by 2 cm with a diamond cutter, and one of the pieces was cleaned with a plasma cleaner for 2 minutes before the spin-coating of the e-beam resist. After no significant dust particles were found on the surface, the wafer was placed in the substrate holder of the spin coater, which was assembled in house. A vacuum pump was turned on to hold the substrate during spinning. As soon as a few drops of e-

beam resist were applied on the wafer, the holder started to spin at 1,500 rpm for 1 minute. The positive e-beam resist was PMMA 600K (AR-P 669.029, ALLRESIST GmbH, Strausberg, Germany). Then, it was baked on a hotplate at 100°C for 30 seconds to dry the surface. In order to produce thick resist layer of ~1.5 µm, the spin coating was repeated 2 more times including the 30-second baking to dry each coated layer. The thickness of the resist is closely related to the viscosity of the liquid resist and spin speed. The thickness is inversely proportional to the viscosity of the liquid resist and the spin speed. After numerous attempts to reach the lowest applicable spin speed possible in order to produce a layer as thick as possible, it was found that the spinning was not steady below ~1500 rpm with the available spin coater. However, the flatness of the resist was better when it was somewhat higher (~1,700 rpm). Once the coating process was completed, the resist was pre-baked on a hotplate at 160°C for 10 minutes. Later, a commercial spin-coater was available for the sample preparation, and lower rotation speed than 1,700 rpm could be done, but most of the resists were made with the in-house assembled spin-coater.

After the pre-bake, the coated resist was ready for the electron beam exposure. Pre-designed patterns were loaded in the software for the pattern generator, ELPHY system, and the input parameters such as electron beam current, dosage, and coordinates were specified. (See 5.4.1.3 for the details about the EBL.) After the exposure the resist was developed and the patterns were revealed. One of the patterns after developing is shown in the top image of the optical microscope images in Fig. 5.4-2. In addition, the developed resist was observed with a white light interference microscope (WYCO NT2000, Veeco Instruments, Woodbury, New York, USA) to measure the thickness of the coated e-beam resist. The resist on the image, Fig. 5.4-3, was overexposed since the tip of the triangle shape structure touches the adjacent structure. The profiles from the image show that the resist was evenly coated and the thickness was measured as ~1.5 µm as it was expected. In the profiles the overshoot on the edges of the developed resist is a measurement artifact and should be ignored. When the pattern was successfully made, the resist with pattern was placed in the evaporation chamber for copper deposition. The copper was deposited by using Auto306 TURBO Vacuum Coater (Edwards High Vacuum International, West Sussex, UK). The thickness of the evaporated copper film was monitored during the deposition. When the thickness was ~600 nm, the shutter was closed to prevent any additional deposition of evaporated copper on the sample. After cooling the chamber for about 15 minutes, the sample was taken out (See 5.4.1.4. Metal evaporation and lift-off technique).

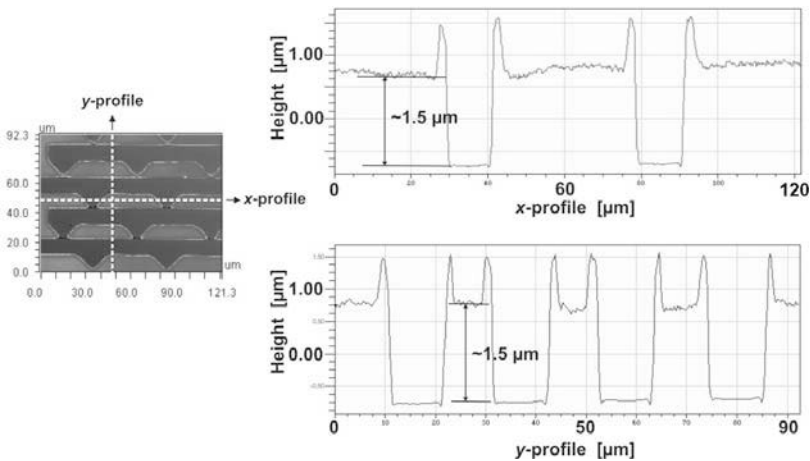


Figure 5.4-3. A pattern for the copper structures by electron beam lithography. The topography and the dimension measurement were produced by a white-light interference microscope. The thickness of the e-beam resist and the quality of the coating can be identified. The overshoot of the measurement artifacts in the profiles should not be considered on the edges of the patterns.

The copper deposited sample was placed in a small beaker with the solution of the remover (AR300-70, ALLRESIST GmbH) for the lift-off procedure. The small beaker was then placed in an ultrasonic bath for about 5 minutes or as long as necessary for the lift-off. As the resist was removed, the lift-off was preceded and the construction of copper structures was completed. (See the optical microscope image in the middle in Fig. 5.4-2.) Once the copper structures were made on the silicon wafer, the mixture of epoxy resin and the curing agent was prepared. The epoxy resin and curing agents are well mixed in an oil bath with an elevated temperature by stirring with a glass rod for several minutes. (See 5.4.1.2 for the details of the epoxy curing conditions.) A Teflon o-ring was placed where the copper electrodes are. It is to prevent overflowing of the runny liquid mixture and to obtain a certain thickness of the cured epoxy. Several drops of the liquid mixture were placed in the o-ring, which was on the silicon wafer with the copper electrodes. The sample was placed in an oven and cured for several hours. After the cure, the oven was turned off and the sample remained in the oven for several hours to cool down slowly. Then, the cured epoxy was removed from the silicon wafer. The surface of epoxy, which was in contact with the wafer was used for the investigation.

5.4.1.2. Epoxy mixing and curing

Two epoxy-curing agent systems were used for the samples. The first system consisted of EPIKOTE 828 and EPIKURE F205 (Resolution Europe B.V., The Netherlands). The epoxy resin, EPIKOTE 828, is a type of diglycidyl ether of bisphenol A (DGEBA). It is a clear and viscous liquid at the room temperature. The curing agent, EPIKURE F205, is a modified cycloaliphatic amine-curing agent. It is a yellowish and also viscous liquid similar to the epoxy resin. According to the manufacturer's description, the epoxy equivalent ratio is 58 parts of the curing agent per hundred parts of the epoxy resin by weight. It was first well mixed by stirring with a glass rod at 80°C for at least 7 minutes in an oil bath. Then, the mixture was cured in an oven at 130°C for 2 hours.

The second system consisted of DER332 (Dow Chemical) and DDS (Fluka Chemika). DER332 is also a type of DGEBA with an epoxy equivalent weight of 174 g, and DDS is 4,4'-diaminodiphenylsulfone, which is an aromatic amine-curing agent. The primary purpose of this system was to compare the results between FMM and EDX because the curing agent, DDS, contained sulfur and the behavior of the curing agent can be revealed by detecting the sulfur content with EDX. DER332 and DDS was mixed in the epoxy equivalent ratio, which is 12.415 g of DDS per 34.80 g of DER332. DER332 was heated at 110°C for about an hour. Then, the temperature was increased to 160°C and DDS was added. The mixture was well stirred with a glass rod for at least 5 minutes. The cure was preceded at 170°C for 2 hours.

5.4.1.3. Electron Beam Lithography

In the process of sample preparation for the stiffness analysis of the interphase by SFM based FMM, the electron beam lithography was applied to create copper patterns on the silicon substrates. Here, the electron beam lithography (EBL) process is described, focusing on the approach in the sample preparation.

Micro lithography is one of the main driving technologies in microelectronics. Lithography using electron beam to expose the resist was one of the earliest processes used for integrated circuit (IC) fabrication. High volume production is done with the optical techniques, but electron beam systems play their own vital roles: First, they are used to generate the masks that are used in optical and x-ray exposure systems; Second, they are used in the low-volume manufacture of ultra-small features for high performance devices [5. 13]. Despite the throughput limitations of electron systems, it might influence the process greatly in advanced manufacturing. Shortly after the development of EBL based on the scanning electron microscopy (SEM) in the late 1960s, it was found that poly(methylmethacrylate) (PMMA) could be utilized as an electron beam resist [5. 14]. In spite of the progressive technological advances since then, it is still often used and much work continues to be done with PMMA resists on a modified SEM.

Without an exception, the patterns for the copper structures in the samples of copper/epoxy composites were also made with PMMA resists and a modified SEM with a pattern generator and blanker. The resist for the sample preparation was made of PMMA positive photo resist 600K by ALLRESIST GmbH, Strausberg, Germany. The EBL system used consisted of an environmental scanning electron microscope (ESEM) (XL30 LaB₆ by FEI COMPANY, Hillsboro, Oregon, USA) and a pattern generator (ELPHY Plus by Raith GmbH, Dortmund, Germany). The resolution limit of resists and the lithography techniques are in one of the interests of the industry for developing advanced applications. Chen and Ahmed [5. 15] stated that the resolution limit of the PMMA positive resist was 10 nm. On the other hand, Vieu et al. [5. 16] proved later that it was possible to achieve below 10 nm resolution for isolated features.

There are two choices for the resist: One is a positive resist, and the other is a negative resist. The positive resist becomes more soluble in the developer after the electron beam exposure, and the negative resist becomes less soluble in the developer after the exposure. Correspondingly, the exposed area is removed with the positive resist and the exposed area will be remained with the negative resist, Fig. 5.4-4. The resist used for the above coating procedure is an example of a positive resist. An example of a negative resist is one

called SU-8. Its sensitivity is much higher than PMMA, so it is vastly applicable in the production of micro-electro-mechanical systems (MEMS). The saturation dosage of SU-8C, which is a modified version of SU-8, is $\sim 3.8 \mu\text{C}/\text{cm}^2$, while that of PMMA is $\sim 500 \mu\text{C}/\text{cm}^2$ [5.17].

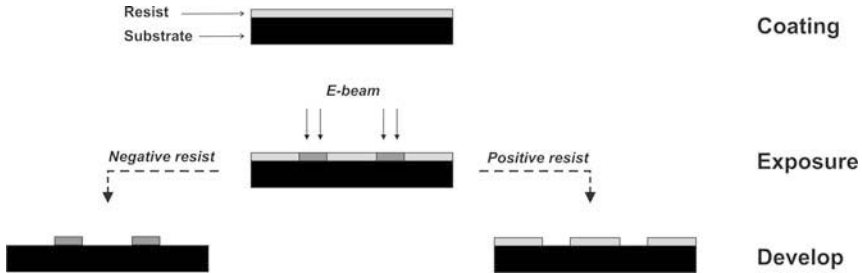


Figure 5.4-4. Process of a positive resist and a negative resist.

When the resist was prepared, the sample was placed into the SEM chamber for electron beam exposure. Before the exposure was conducted the desired pattern needed to be created in the pattern generator. One of the patterns for the EBL is shown in Fig. 5.4-5. It also shows how the software is arranged to control the EBL. The windows shown in the figure are for alignment, stage control, magnification, and exposure parameters. When the EBL parameters were entered and the setup was finished, the resist was exposed to the electron beam. By calculation and trial-and-error, the proper dosage of the resists prepared under the EBL system used was found to be $\sim 300 \mu\text{C}/\text{cm}^2$. When the proper dosage was not used, the resist will be under or over-exposed, Fig. 5.4-5. Once the electron beam was focused on the resist surface and stabilized, the exposure to the electron beam was started. After the exposure, the exposed area was removed by using a developer (AR600-55, ALLRESIST GmbH) and the pattern was created.

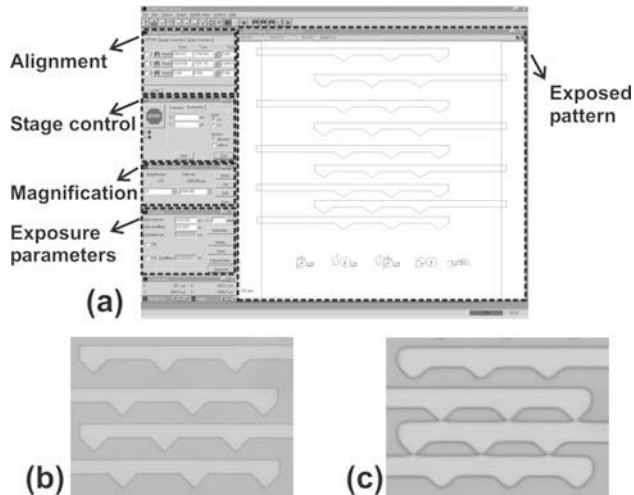


Figure 5.4-5. (a) Overview of the ELPHY Plus software and the design of the copper structure. (b) Well-created pattern. (c) Over-exposed pattern.

5.4.1.4. Metal evaporation and lift-off technique

In order to create copper structures on the substrate, the evaporation and lift-off technique was applied. In physical vapor deposition (PVD), the solid material is vaporized by heat or by an energetic beam of electrons, photons (laser ablation), or positive ions (sputtering) to be transported to the substrate [5. 18]. Evaporation is one of several PVD techniques, which also include ion plating, sputtering, etc. Metals with low melting temperatures, such as gold, are often deposited with this technique and the amount of material that can be evaporated is only small. When the pressure of the chamber is below 10^{-3} Pa, the heat source for the evaporation boat is turned on. The evaporation boat, which contains the source metal, is heated up by an electrical current. Once the temperature is high enough to start the evaporation of the metal, the shutter is opened to start the deposition of the metal on the sample. The thickness of the film is monitored during the deposition. At the desired thickness the shutter is closed to prevent additional deposition on the sample and the electrical current is turned off. The sample remains in the chamber for about 10 minutes to cool down before it is taken out, in order to avoid oxidation of the evaporated metal layer at a high temperature. During the evaporation the mean free path length of the molecules is long enough, so that the evaporated metal moves in straight lines before it condenses onto the sample. This prevents depositing on the wall of the resist patterns. If an alloy is evaporated, the composition of the deposited material might be change due to the different partial pressures of the components [5. 19]. The schematic of the evaporation chamber is illustrated in Fig. 5.4-6.

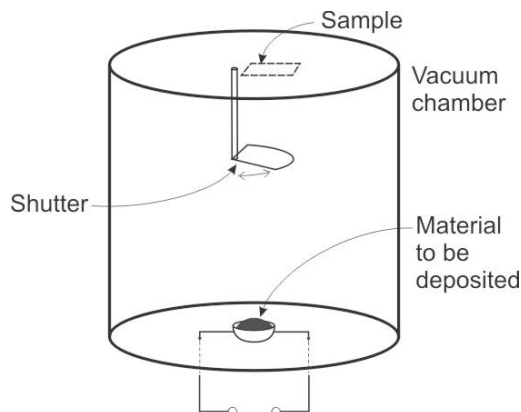


Figure 5.4-6. Schematics of evaporation chamber.

5.4.2. Preparation of cross section surface

After the characterization of the substrate-detached sample had been completed, the cross section sample was prepared. The analysis of the cross section was important because the surface was not in contact with the silicon wafer. Thus, the pure interaction between epoxy system and copper during the curing process could be investigated. In addition, the result could be compared with the result from the substrate-detached sample, in order to elaborate if the influence of silicon substrate could be neglected.

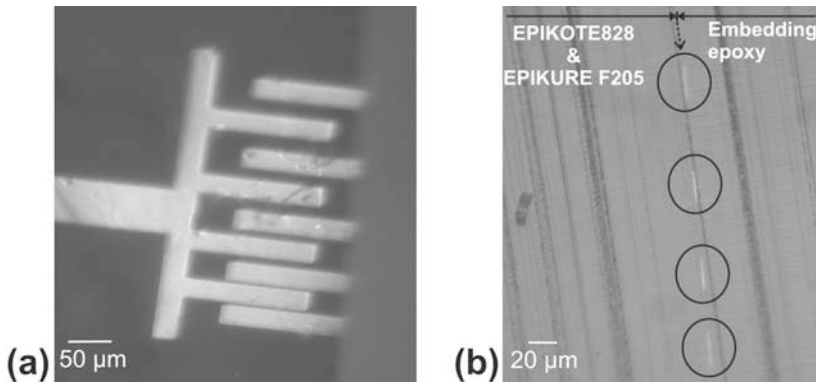


Figure 5.4-7. Images of a cross section sample taken by an optical microscope. (a) The copper structures are seen through the embedding epoxy. (b) The cross section of the copper structures is visible inside the circles. The interface of two epoxy systems cannot be identified in the optical microscopic image, but it is marked with a dotted arrow on the top of the image.

In order to prepare the cross section surface, the surface of the substrate-detached sample was first covered with an embedding epoxy to create a continuous surface for SFM analysis. After the embedding epoxy was cured, it was carved with an ultramicrotome (ULTRACUT 125UCT, Leica Mikrosysteme GmbH, Vienna, Austria). Microtoming was done at the room temperature, using an ‘Ultra30’ type diamond knife (Diatome, Biel, Switzerland). The copper structures on the substrate-detached surface can be still seen through the embedding epoxy, Fig. 5.4-7(a) and the cross section surface is shown in Fig. 5.4-7(b). The cross sections of the copper structures are marked with circles. If the copper lines were connected, it would be the interface of EPIKOTE system and the embedding epoxy. The dotted arrow line describes the direction of the interface of the two epoxies. During the interphase characterization with SFM, the path of the tip of the SFM cantilever can be prescribed in such a way that it scans the EPIKOTE epoxy near copper layer, and then it scans over the copper and finishes scanning the embedding epoxy.

5.5. Properties of the epoxy/copper interphase

The following results are from the analysis of the samples, which were made by the method described in the previous section. The epoxy area around the copper, which is the interphase of the two materials, was the region of interest (ROI). The physical properties of the ROI were intensively studied in terms of the stiffness changes in comparison to the bulk area, which is considerably further away from the copper. In order to confirm the results and identify the reasons of property gradients in the ROI, a composition analysis by means of energy-dispersive analysis of X-rays was performed.

5.5.1. Copper and DGEBA-based epoxy with a cycloaliphatic curing agent

5.5.1.1. Interphase analysis of substrate detached surface

A DGEBA-based epoxy resin, EPIKOTE828 and a modified cycloaliphatic curing agent, EPIKURE F-205 were used to prepare the sample. The epoxy surface was cured in contact with copper, which is on the silicon substrate, then it was detached from the substrate, and the surface was analyzed by SFM. Thus, it must be kept in mind that the surface was not

cured as a free surface, which refers to a surface in contact with air. The silicon may have influenced the property of the cured epoxy. Hence, the analyzed epoxy surface may contain the properties influenced by copper and silicon. However, because the entire epoxy surface was in contact with the silicon substrate, its influence is assumed to be equal and homogeneous. On the other hand, copper is partially in contact with epoxy. Therefore, the stiffness gradient in the interphase is considered to be caused by the influence of the copper surface. On the corner, where three materials are supposed to meet, a small gap may exist if the liquid epoxy does not fill in all the way to the corner of copper and the substrate. This may be caused by the non-zero viscosity of the liquid epoxy formula, Fig. 5.5.1. Also, the cooling process could have caused shrinkage due to the difference of the heat expansion between epoxy and copper. In this unfilled space, the epoxy is not in contact with the silicon substrate. Even though the sample surface is in general very flat and continuous between the two materials (copper and epoxy), the small gap creates a slight unevenness and discontinuity at the interface. This gap, ~ 5 nm, in the sample sometimes creates a rough surface condition to perform the stiffness characterization by FMM because the sudden height change results in a steep slope. However, in some cases the area can be nicely analyzed by means of FMM when the roughness of the surface is within the tolerance. The small gap should not influence in the overall result too much, because the size of the gap is too small to influence the result of entire interphase. In addition, the stiffness measurement by FMM becomes questionable in the very area close to copper. The reason is that the measurement can be influenced by the neighboring material, copper, which is a much stiffer material. Thus, there might be an influence of copper stiffness in the epoxy interphase within ~ 10 nm from copper, considering the indentation depth is ~ 1 nm. Regarding the elimination of the discontinuity between copper and epoxy, the cross-section surface is prepared by cutting with a microtome, whose result is presented in the next section.

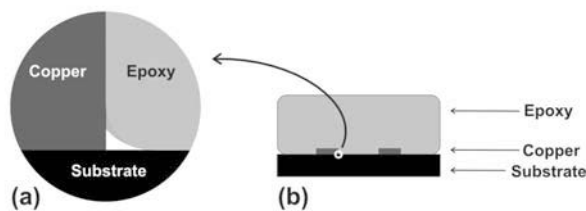


Figure 5.5-1. (a) An illustration of liquid epoxy mixture filling up the corner of the silicon substrate and copper structures. (b) An overview of the sample.

The analysis of SFM clearly distinguishes the copper surface and the epoxy surface. The images of SFM are shown in Fig. 5.5-2, whose scan area is $(4.8 \mu\text{m})^2$. The morphologies of copper and epoxy are very different, which can be found in Fig. 5.5-2(a). The top of the image is the copper surface, and fine grain like structures are shown on the surface. The epoxy placed partially on the edge of the copper structure and it was seen like a mountain range above the dotted line, which indicates the end of the copper structure. On the epoxy there is almost no morphological features seen unlike the copper surface. Just below the border line with the copper (dotted line) a narrow lane of ~ 5 nm along the copper is found. It

is dark contrast because it is lower compared to the rest of the area and it is considered to be the slight discontinuity between copper and epoxy. The height range in the topography is from 0 to 104 nm. The FMM amplitude image, Fig. 5.5-2(b), has very distinguishable two contrasts, which are copper (bright) and epoxy (dark). The contrast is adjusted for both contrasts, thus it is hard to recognize the gradient of contrast in the epoxy interphase, which is shown just as a dark area according to the image. The FMM amplitude image is created based on the signals from the lock-in amplifier, so the scale is arbitrary. The performance of the feedback control is validated by the normal force image, Fig. 5.5-2(c).

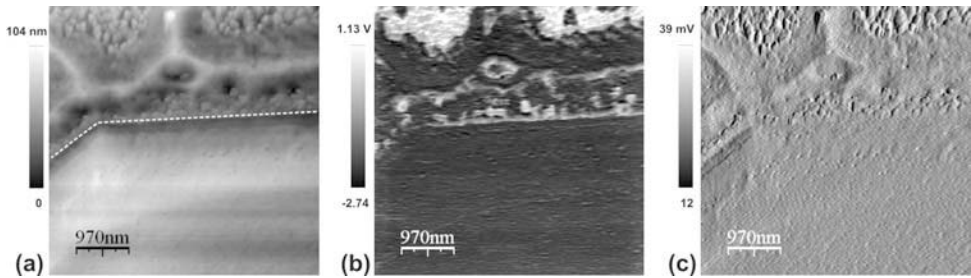


Figure 5.5-2. (a) SFM Topography ($4.8 \times 4.8 \mu\text{m}^2$). The end of the copper is marked by a dash line. (b) FMM amplitude image. The frequency of sample modulation was 59 kHz. (c) Normal force image.

Carefully observing the interphase in epoxy, the property variation in the cured epoxy can be recognized. The interphase is shown in various forms of images in Fig. 5.5-3. The topography, Fig. 5.5-3(a), shows where the copper ends and the epoxy starts by elucidating the morphologies and the height differences. The copper is located on the very top of the image and the rest is epoxy, which is presumably mostly interphase. The line profile below the image is taken from the line, which is indicated in the image. The line is drawn parallel to the copper structure in order to identify the precise changes in terms of distance from the copper. The top of the line in the image corresponds to the left of the profile as it is indicated with a filled circle. A small arrow in the profile points out the end of copper and the beginning of the epoxy. Thus, to the left side of the arrow is copper and to the right side is the epoxy. In the topography the epoxy is partially higher than the copper surface. According to how the sample was produced, the epoxy surface should not be higher than the copper surface because both materials were in contact with the flat silicon wafer. It means that the surface should have been leveled. The reason for the uneven surface in epoxy could have been from the slight shrinkage upon curing. The volume change of the epoxy undergoes greater changes than the copper during the curing process. The surface turns out to have a level difference between the copper and epoxy of the order of 10 nm. Some contrast can be recognized in the FMM amplitude image, Fig. 5.5-3(b). Near the copper the FMM amplitude image is darker than away from copper. When the upper half of the epoxy area is compared to the bottom half, one can distinguish the contrast difference. In the profile of the FMM amplitude below the image, the FMM amplitude on the copper is significantly higher than on the epoxy. Near the arrow the FMM amplitude is high, but there is low FMM amplitude on the left side, where supposedly the copper region, but some epoxy placed on the edge of the copper resulted in the low FMM amplitude. Then, in the right side of the arrow, which is the epoxy region, the profile starts going down rapidly until

around $\sim 0.6 \mu\text{m}$, then rising slowly until $\sim 1.9 \mu\text{m}$ and slight decrease appears before it reaches the bulk area at $\sim 2.5 \mu\text{m}$. Even though a trend line is drawn in the profile, it is still hard to recognize the changing point at $\sim 1.9 \mu\text{m}$, since the y -scale is too large to recognize the change, because it is adjusted to show the FMM amplitude in the copper as well. It is discussed in more detail in Chapter 6. The normal force image does not show either large or sudden changes of cantilever position. The arrow in the profile shows when the tip scans over the interface, but it did not affect the measurement greatly. The normal force values are within 10 mV and this indicates that what the profile includes is mostly noise from the signals.

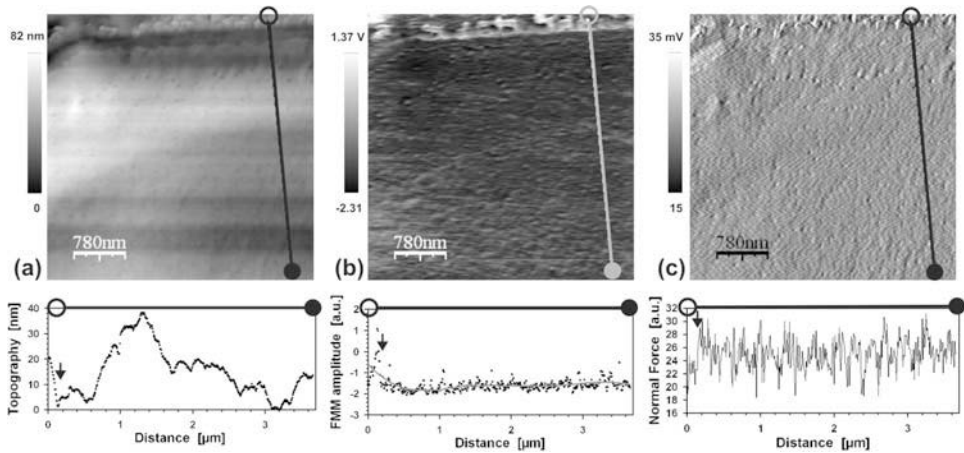


Figure 5.5-3. SFM images and profiles of epoxy interphase with copper. (a) Topography. (b) FMM amplitude image. (c) Normal force image.

5.5.1.2. Cross section surface

The cross section surface is prepared to study the interphase, which is produced only in contact of copper and epoxy. In contrast to the substrate detached surface, which was made while it was in contact with the silicon wafer, the surface of the cross section is constructed by revealing the inside of the material, where copper and epoxy are in contact. SFM images of the cross section surface are Fig. 5.5-4, whose scan range is $(4 \mu\text{m})^2$. The microtoming of the surface left some traces from cutting on the surface, which can be seen in the topography, Fig. 5.5-4(a). The traces are almost parallel to the copper structure and a profile could be chosen to show the stiffness of the interphase without the influence of the trace. The copper is obviously higher than the rest of the area as it is shown in the profile of the topography. The points between the upside down triangles is the copper, which is as high as over 40 nm more than adjacent epoxy. (Note that the filled circle is on the right side in the image and on the left side in the profile in order to place the interface on the left side of the profile.)

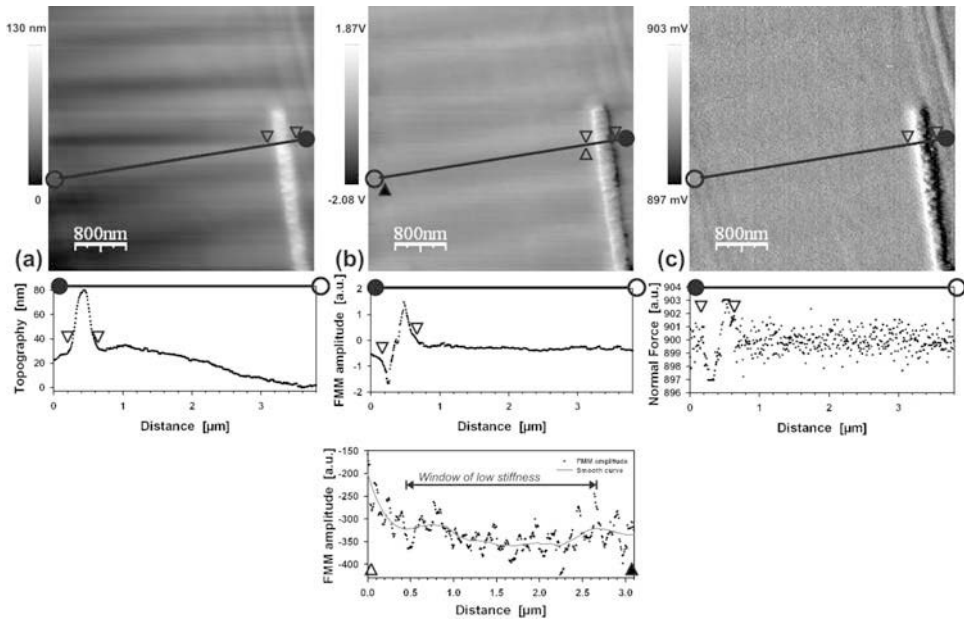


Figure 5.5-4. SFM images and profiles of epoxy-copper interphase from the cross section surface. (a) Topography. (b) FMM amplitude. (c) Normal force image.

The FMM amplitude image, Fig. 5.5-4(b), shows a strong influence of the surface geometry when the tip scans across the copper. In general, the tip has a lateral tilt caused from scanning. When the tilt changes, the tip-sample contact area changes as well. As the tip scans over the copper, the contact area increases and the FMM amplitude increases as well. Thus, the amplitude is at the maximum when the uphill slope is at the highest, then the FMM amplitude starts to decrease. It reaches the minimum when the downhill slope is at the lowest, and then it increases again. Therefore, the scan direction is from the unfilled circle to the filled circle. The second profile of the amplitude is between the unfilled triangle and the filled triangle. The profile starts at the point where the unfilled triangle is, and it ends at where the filled triangle is. A trend line is drawn to help recognize the stiffness gradient. The low stiffness region is $\sim 2.5 \mu\text{m}$ wide and this result is in good agreement with the result from the substrate-detached sample. The normal force image, Fig. 5.5-4(c), shows that the feedback control of SFM during the scanning was acceptable since there are no features on the epoxy area. The sudden change of height in the copper area was clearly the troublesome area, but it barely affected the interphase measurement.

5.5.2. Copper and DGEBA-based epoxy with an aromatic curing agent

5.5.2.1. SFM analysis of the interphase of epoxy/copper

The cross section of the epoxy based on DGEBA cured with DDS was analyzed with SFM. All images in Fig. 5.5-5 were simultaneously captured during scanning, as well as the opposite direction of the scan (not shown), so a total of ten images are available from the analysis. There are five different kinds of images: topography, FMM amplitude, normal force, lateral force, and phase shift image. They show the condition of the interphase

between the copper and the cured epoxy. The cantilever used was Arrow™ FMR. FMM was performed with a frequency of 35.1 kHz. The topography image, Fig. 5.5-5(a), shows the copper as a bright vertically straight region. The surface was microtomed in order to create a flat and smooth surface with a continuous interface. Being a softer and more elastic material than copper, the cured epoxy underwent more relaxation than the copper during microtoming of the surface. The right side is the DGEBA epoxy cured with DDS and the left side is the embedding epoxy for the SFM scanning. The dotted line in the first profile indicates the end of copper and the beginning of the epoxy. The first profile of the topography shows that the copper is ~200 nm higher than the epoxy surface. The copper region is shown as almost symmetrical convex curve. Both sides of epoxy surfaces are flat. The flatness of the epoxy surface can be better seen from the second profile, which begins at the end of the copper. One should notice that the height scale is in nanometers and the distance scale is in micrometers. Thus, the height difference is only 10 nm in the first 1 μm and the slope is much less than 3°, which is the critical slope for the FMM analysis. The slope is calculated and shown in the profile. Because of the scattering of the measured height points, mean values were used to calculate the slope. Under consideration of the scan speed and the scan range of the image, every 5 pixels, which is about 70 nm, were averaged to find the mean values, then two consecutive mean values were taken to determine the slope. As the graph shows, the slope in the topography is within $[0.02]^\circ$. It indicates that an influence from the geographical artifact was minimal during the FMM analysis.

The FMM amplitude image, Fig. 5.4-5(b), shows the stiffness of the epoxy. The narrow vertical region indicates the copper and the DDS cured epoxy is on the right. From the contrast of the image the DDS cured epoxy is stiffer than the embedding epoxy as it is shown brighter than the embedding epoxy. Being cured at room temperature, which is a lot less than the curing temperature of the DDS cured epoxy, it is more likely that the embedding epoxy has lower stiffness than the DDS cured epoxy. The stiffness difference between the epoxies can be recognized from the first profile of the FMM amplitude image. The right side, the DDS cured epoxy, is higher than the left side. The copper appears to have a stiffness variation, however, it is an artificial representation from the combination of geometrical effect of the copper surface and the scan direction. Because the geometry of the copper includes variation of sudden height changes, the tip-sample contact area was not constant as the tip scans over the area. It is probably the predominant reason for the FMM amplitude variation on the copper since the scan direction changes the direction of the amplitude variation. Thus, at forward scan the tip-sample contact area is the smallest when the tip is at the beginning of the convex curve and the contact area continues increasing until the end of the curve. It appears that the epoxy region, which is just beside the copper, has even higher amplitude than the copper. The high FMM amplitude can be explained by the minor discontinuity, evidently less than 15 nm, between the copper and epoxy. The gap is close to the size of the tip or a part of the tip and the tip-sample contact area could have been dramatically increased, resulting in large FMM amplitudes. The second FMM amplitude profile starts at the high amplitude. After the peak of the amplitude it rapidly decreases until ~0.2 μm in the second profile, then the decrement slows down. The high amplitude of the epoxy near copper indicates high stiffness. Another possible cause of high amplitude near copper can be an influence from the stiff copper, but considering the depth of the tip penetration, which is ~1 nm, the influence of copper should not be more

than 10 nm away from its surface. Therefore, the stiffness of epoxy near copper surface is definitely much higher than the bulk epoxy. The amplitude decreases rapidly up to $\sim 0.2 \mu\text{m}$, then the smaller decrement continues up to $\sim 1 \mu\text{m}$. It is obvious to see the decrease of the slope until $\sim 1 \mu\text{m}$, but it is hard to recognize where it exactly ends. However, the gradient of amplitude exists $\sim 2 \mu\text{m}$, and so does the length of the interphase between the copper and the cured epoxy.

The normal force image shows the force exerted in normal direction by the cantilever and it also indicates that the feedback parameters were well adjusted for the characterization by showing the constant values in epoxy areas. The scan direction can be recognized in the first profile of the normal force from the values in the copper area. The scan direction was from the left to the right since the normal force value starts high at the beginning of the copper and it ends low at the end of the copper. When the tip faces a sudden height change on the surface, the feedback control does not compensate the height change fast enough, and it can be monitored in the normal force image. Thus, the normal force of the cantilever suddenly jumps, then it decreases as the feedback control tries to reduce the force on the cantilever by adjusting the level of the z-piezo. Then, the normal force decreases until it reaches the flat surface of epoxy again. In a similar manner, a force deviation occurs for the negative slope. The profile shows a typical behavior of the cantilever and the performance of the feedback control. The constant normal force values in the second profile indicate that the feedback control was successfully performed. Even if the feedback did not optimally perform in the copper region, it performed well in the epoxy, especially where the epoxies showed slight unevenness for $\sim 1 \mu\text{m}$, thus the unevenness should not have generated an artificial contrast.

The lateral force image, Fig. 5.5-5(d), shows the torsion of the cantilever during scanning. Due to the different friction forces between the surfaces of different materials and the tip, the torsion of the cantilever exerts various lateral forces. According to the Bowden and Tabor model [5.20], the friction is proportional to both the contact area and a mean lateral force per unit area, so-called shear strength, in micrometer scale. The copper surface probably produces a homogenous lateral force per unit area. The contrast in copper is probably caused by the variation of the contact area. The left side is dark and the right side is bright, so the tip-sample contact area was smaller on the left side than the right side. The first profile shows the clear difference of the torsion of the cantilever in the copper region from the epoxy region. The lateral force is even lower than in the epoxy area at the beginning of the copper, then increases until it reaches the flat epoxy area. The lateral force image often contains a particular artifact. This image also shows an artifact, which is the wave-like shape in diagonal direction. The artifacts are often caused by the deflection of a part of the laser beam from the sample surface and optical interference with the part of the beam reflected off the backside of the cantilever.

The phase shift image, Fig. 5.5-1(e), shows how the cantilever reacts to the sinusoidal oscillation of the sample. Depending on the surface properties, a delay of the oscillation occurs. Copper being a stiff material, its phase shift is much less than that of the epoxy, which is a viscoelastic polymer. The first profile shows that the phase shift is lower in the copper region than in the epoxy regions. The phase shift only in the epoxy region is shown in the second profile.

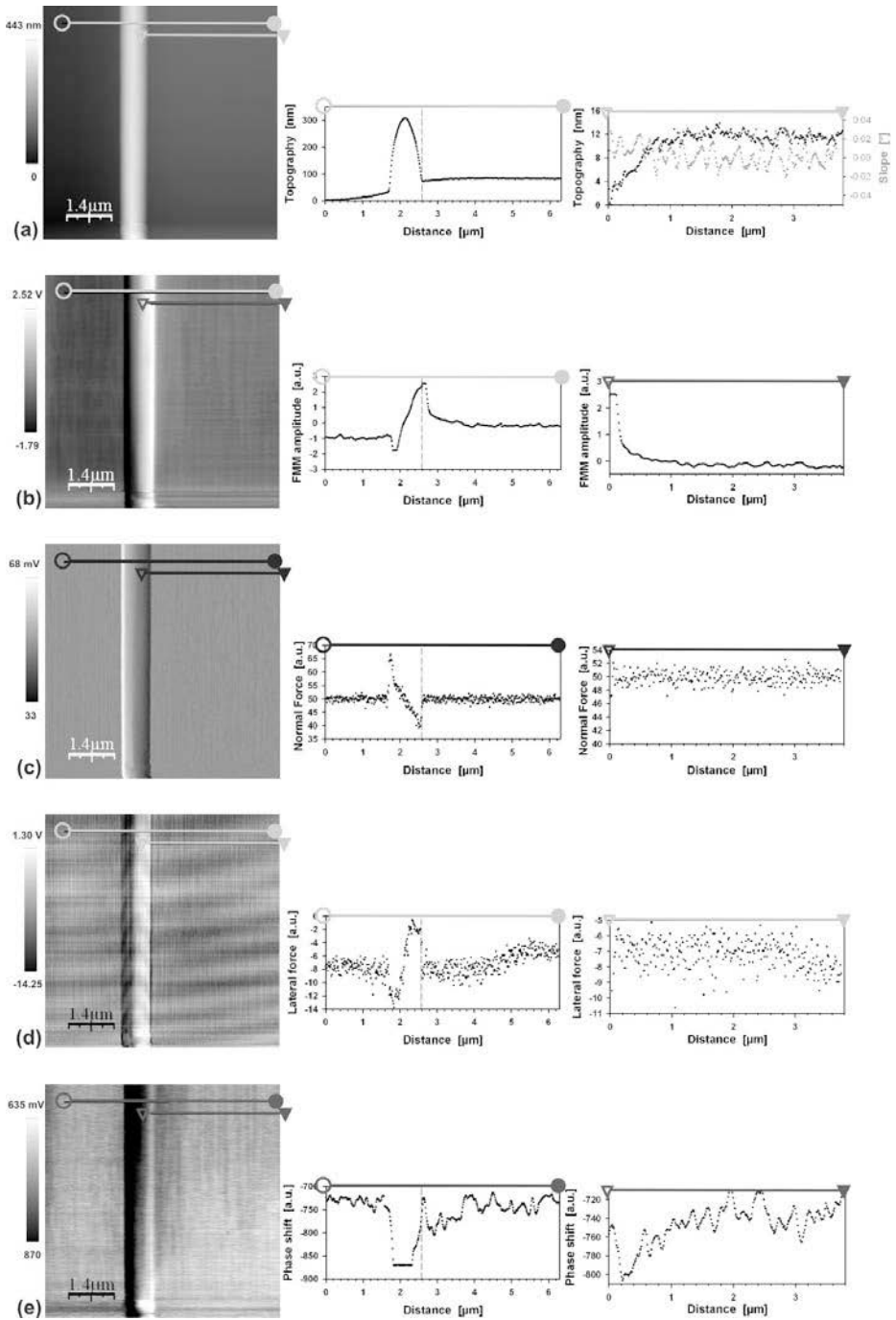


Figure 5.5-5. SFM analysis of the interphase between copper and cured epoxy (DGEBA-DDS). The cross section surface of the sample was analyzed for topography and stiffness. (a) Topography. (b) FMM amplitude image. (c) Normal force image. (d) Lateral force image. (e) Phase shift image.

5.5.2.2. Energy-dispersive analysis of X-rays for epoxy/copper interphase

The chemical content analysis in the interphase was done using energy-dispersive analysis of X-rays (EDX). An epoxy resin based on DGEBA (DER332) was cured by DDS (4,4'-diamino-diphenylsulphone). The DDS molecule, Fig. 5.5-6, contains sulfur, which can be used as a tracer to determine the concentration of DDS by EDX, assuming that the sulfur is not a part of the curing reaction. Thus, the concentration of sulfur should indicate the initial movement of the curing agent, DDS, during the gelation, the beginning of the cure. If there is a change of concentration of sulfur in the interphase, it is a good indication that the local concentration ratio between the epoxy resin and curing agent also has changed. This can be one of the main causes for the formation of the interphase and the change of its mechanical properties.

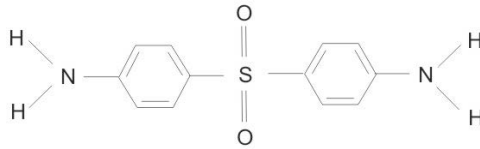


Figure 5.5-6. Molecular formula of DDS (4,4'-diamino-diphenylsulphone)

Similar to the change of modulus according to the concentration of curing agent as discussed in Chapter 2, it can be also seen with DER332 and DDS system. The relationship between the stoichiometric concentration ratio (r), and the shear storage modulus (G') and storage modulus of Young's modulus (E') at 20°C are shown in Fig. 5.5-7 with DER332 and DDS. The dynamic-mechanical analysis of a series of cured epoxy samples characterizes a change of shear modulus with different concentration ratios between DER332 and DDS [5.21]. The E' is calculated from G' and Poisson's ratio (ν). The samples were cured at 170°C for 2 hours. An evident increase of the storage modulus was observed in the region of $r < 1$, whereas there is no significant change of modulus in the region of $r > 1$. The stoichiometric mixing ratio of epoxy and amine is given by $r = 1.0$. The curve indicated 'heating' is the DMA measurement as the temperature increases and the 'cooling' curve is the *vice versa*. The cooling curve might represent a property after some post cure, thus the relation between r and E' from the heating curve is used to estimate E' of the interphase region according to the TEM-EDX. A linear relationship, Eq. 5.2, shows where r is less than 1.1 [5.5].

$$E'[\text{GPa}] = 6.0 - 2.6r \quad (5.2)$$

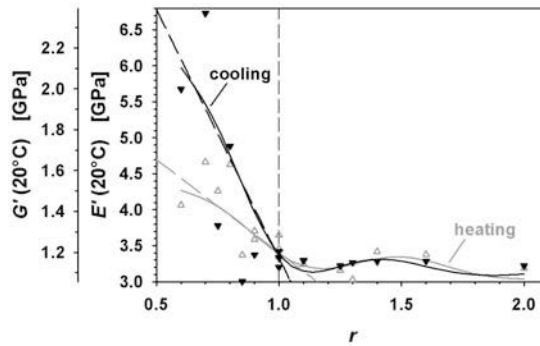


Figure 5.5-7. Storage modulus of DER332-DDS at 20°C as a function of amine concentration ratio (r). The samples were cured at 170°C for 2 hours. [5.21]

EDX was performed with SEM and TEM. After the SFM analysis a thin conducting metal layer, e.g. ~50 nm of titanium, was deposited for the SEM analysis in order to avoid an electrical charging effect. During the EDX with SEM, the applied voltage of the beam was 10 kV and the applied current on the surface was 0.6 nA. The spot size of the beam was ~125 nm. The magnification was adjusted to have an exposed area of ~1 (μm)² and each exposure lasted 60 seconds. In order to conduct EDX with TEM, the thickness of the sample was prepared to 100 nm. The surface of the sample was deposited with platinum in order to have a conductive layer. Then, using the focused-ion beam (FIB) the sample was cut into the thickness. The surface of the prepared film with the thickness of ~100 nm is shown in Fig. 5.5-8. The sample had to be placed in the TEM chamber with a tilt of 36° to the incident beam, so that the detector could receive the maximum amount of the X-rays emitted. Because of the tilted sample position, the incident beam traveled through the sample more than the thickness of the sample. The spot size of the beam was ~8 nm, which is a lot less than that of SEM, and the dwell time was 200 seconds. The surface current on the sample was 126 mA and the beam voltage of TEM was 40 kV. Taking advantage of the small spot size of the beam and the small thickness of the sample, the TEM-EDX acquires a better spatial resolution for the change of local sulfur concentration than the SEM-EDX. When the spot size of the electron beam decreases, it improves the spatial resolution and decreases the excitation volume effect as it is shown in Fig. 4-6. Therefore, the sensitivity to the change of sulfur concentration improves.

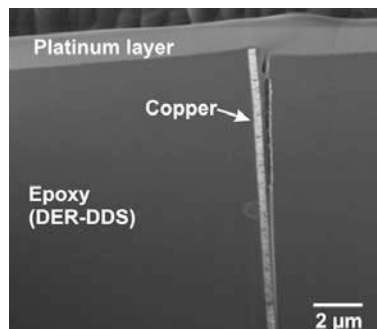


Figure 5.5-8. Sample surface prepared by using FIB for TEM-EDX analysis.

The profile of sulfur content in the interphase from SEM-EDX is shown in Fig. 5.5-9(a). It shows the temporal concentration variation, which infers that diffusion of amine took place. The epoxy resin and the curing agent were prepared in the stoichiometric ratio ($r = 1.0$), thus any change of the sulfur content indicates a change of concentration ratio. It is likely that the preferential adsorption occurs when the viscosity of the mixture is low, so the alteration of local concentration ratio has taken place at the beginning rather than at the end of the curing process. The sulfur content starts low at just outside of the copper. It increases up to $\sim 1.3 \mu\text{m}$, then decreases until $\sim 3 \mu\text{m}$ according to the profile. Afterwards, the sulfur content shows a slight increase before it reaches the bulk region at $\sim 5 \mu\text{m}$. Each data point indicates $\sim 1 \mu\text{m}^2$ and it has some overlap with the previously measured point. Despite the limited spatial resolution, the SEM-EDX shows the general behavior of the sulfur content in the interphase. Variation of the sulfur content is revealed until $\sim 5 \mu\text{m}$, showing a peak at $\sim 1.3 \mu\text{m}$. With an improved spatial resolution, the TEM-EDX was conducted and the result was compared with the SEM-EDX result. Once more the sulfur content was measured and the profile is shown in Fig. 5.5-9(b).

TEM-EDX takes advantage of small spot size, so comparing with SEM-EDX, the spatial resolution is vastly improved and the detection is more sensitive to the local property variation. A result from the TEM-EDX is shown with a smooth curve to show the trend in Fig. 5.5-9(b). The smooth curve was created with the Savitzky-Golay algorithm (*TableCurve 2D*, Systat Software Inc.). The content of sulfur is evidently low at the beginning of the profile, which denotes the beginning of the epoxy at the edge of the copper structure. The curve increases until $\sim 1.3 \mu\text{m}$ away from the copper and reaches a peak of sulfur content. A reasonable correlation is seen with the result from the SEM-EDX. On the other hand, a dip shows at $\sim 2.2 \mu\text{m}$ and the bulk region seems to start at $\sim 3.5 \mu\text{m}$, while the result from the SEM-EDX shows a dip at $\sim 2.8 \mu\text{m}$. The horizontal dashed line indicates the sulfur content in the bulk, which is the mean of the values obtained starting at $3.5 \mu\text{m}$. Thus, the sulfur content in the bulk is 18.6 in arbitrary units. Although the spatial resolution was improved with the TEM-EDX, the scattering of the data hindered to recognize the exact behavior of the curing agent by analyzing the sulfur content. The smoothing curve could also have slightly moved the location of the peak or dip, being evaluated with the neighboring points. The position variation of the peaks and dips between the results of SEM-EDX and TEM-EDX could be caused by those reasons. However, both analyses show well correlated results, including the same trend of the increase and the decrease of the sulfur contents.

Employing the relation between the stoichiometric concentration ratio and the storage modulus found by Munz et al. [5.21], the profile of the storage modulus (E') in the interphase was constructed in Fig. 5.5-9(c). Using the sulfur content in the bulk epoxy as the reference point to calculate r in terms of the distance from the interface, the fit curve of the sulfur content was converted to E' using Eq. 5.2, which is valid if r is less than 1.1. The entire range of the calculated r values satisfied the condition. It is reasonable to assume that the EDX signal of sulfur concentration is linearly proportional to the sulfur concentration because the range of sulfur content is small. The profile of the estimated E' shows a high stiffness in the interphase in close vicinity of the copper structure. E' decreases until the peak of the sulfur content, then increases up to the dip of the sulfur content in the fit curve. Thus, the stiffness increases as the sulfur content decreases in the interphase. A decrease of sulfur content denotes a decrease of amine content. According to the calculated E' , the

lowest stiffness in the interphase is close to that of the bulk. The two low stiffness regions are ~6 percent below the bulk value. In addition, the local peak of the calculated stiffness at ~2.1 μm is ~13 percent higher than the bulk value. The stiffness analysis with the SFM-FMM, Fig. 5.5-9(d), also shows relatively high stiffness near the copper in comparison with the bulk similar to the calculated E' . According to the FMM-amplitude image, a rapid decline of stiffness takes place until 0.3 μm , then the decrease slows down and continues until ~1.8 μm . The lowest amplitude is ~15 percent lower than that of the bulk. Then, the stiffness increases until reaching the bulk at ~3.9 μm . A good agreement can be found in terms of the size of the interphase, which is ~4 μm . However, a discrepancy can be found at ~2.0 μm between the calculated E' and the FMM-amplitude profile. While E' reaches the highest value, the FMM-amplitude shows the lowest value at that distance away from the interface. Even though this FMM-amplitude profile indicates a decrease and then an increase of stiffness before it reaches the bulk value, the increasing part is often not shown by profiles of other regions in the same sample. As seen from the profile, the amplitude difference between the bulk and the lowest amplitude is relatively smaller than the difference of the highest amplitude and the bulk. The small difference of stiffness may not be recognized sometimes, or it may not occur always. As a result, the size of the interphase can show a variation. When a lowest amplitude appears at ~2 μm , the interphase tends to be wider than without the appearance of the lowest amplitude. Therefore, the stiffness profile from the FMM-amplitude analysis shows a good correlation with the EDX results especially at the beginning of the interphase.

The profile from the FMM amplitude does not show a peak and dip behavior, whereas this is seen in the profiles of SEM-EDX and TEM-EDX. The interphase determined by the stiffness variation is relatively smaller than the interphase determined from the variation of the sulfur content (~2.0 μm). The width of variations of the sulfur content are ~4.0 μm determined by SEM-EDX and ~3.5 μm by TEM-EDX. This is a strong indication that the storage modulus and the concentration ratio do not have a linear relationship with each other. A modulus peak at ~2.2 μm in the profile of TEM-EDX does not show in the profile of the FMM amplitude. It is likely that a small change of the curing agent concentration influences the mechanical property of the epoxy only modestly and is not detected by the FMM analysis. Therefore, there is a threshold concentration of the curing agent in order to change the mechanical property of the cured epoxy, which can be recognized by the SFM-FMM analysis. However, both analyses, the EDX and SFM-FMM, provide valuable information about how the mixture of the epoxy resin and the curing agent behaves at the beginning of the reaction when it is in contact with a copper surface, and how the mechanical property is influenced by this behavior.

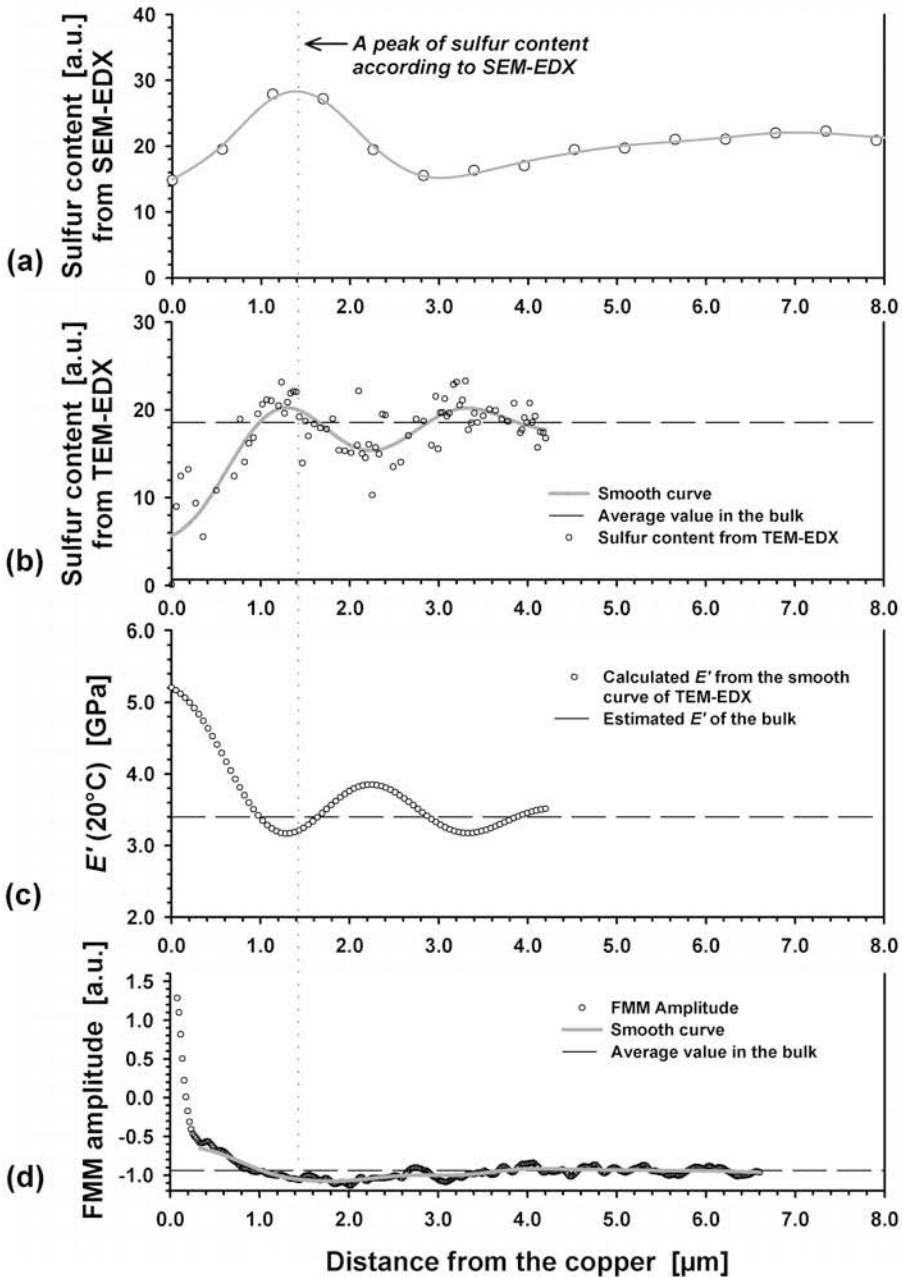


Figure 5.5-9. (a) Sulfur content in the interphase by SEM-EDX. (b) Sulfur content in the interphase by TEM-EDX. (c) Calculated Young's modulus from the fit curve of the TEM-EDX result. (d) Stiffness analysis of the interphase by SFM-FMM.

5.6. Surface morphology of the cured epoxy

The homogeneity of the cured epoxy has been discussed in terms of the morphology on the surface. Scientists have seen various sizes of nodules on the surface, but the condition of the nodule formation is still not defined [5.22]. Because the surface condition is an important factor for adhesion, the morphology on the cured epoxy surface is considered as significant information of cured epoxy properties.

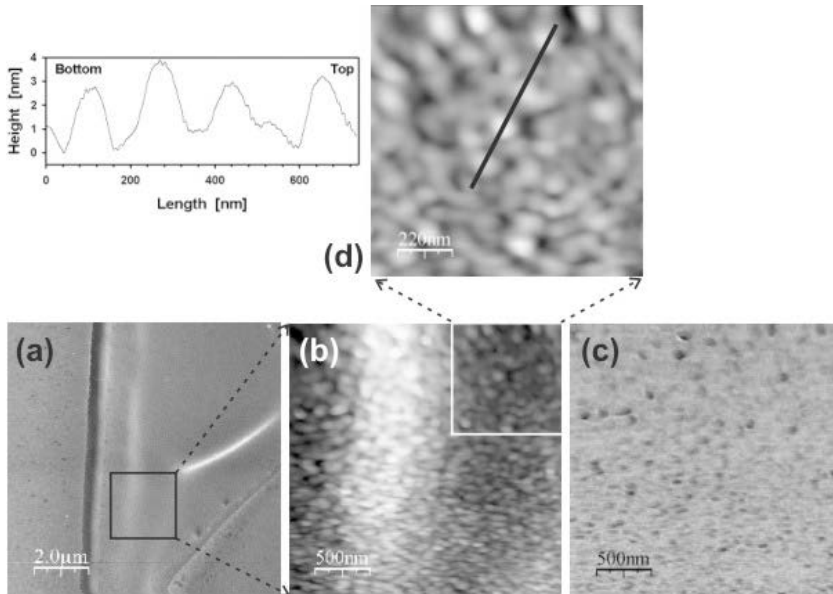


Figure 5.6-1. Nodules on the epoxy surface by SFM. (a) Topography of epoxy and copper surface. The copper structures are on the left and the lower right corner, and the rest is epoxy. The height scale is 22 nm. (b) Topography of nodules on epoxy surface. A new image was obtained within the previous image by SFM. The height scale is up to 76 nm. (c) FMM amplitude image of nodules on epoxy surface. (d) Software-based zoomed image. The range of height is up to 7 nm. The profile on the left describes the line marked in the image.

The mixture of the epoxy resin and the curing agent (EPIKOTE 828 and EPIKOTE F-205) was cured in the stoichiometric ratio on silicon substrate at 80°C for 2 hours, and then post-cured at 130°C for 1 hour. The nodular microstructures are observed in topography image and stiffness image, Fig. 5.6-1(b) and (c). The large scan area of $(10 \mu\text{m})^2$ in Fig. 5.6-1(a) shows copper structures on the left and the lower right corner, and the rest is epoxy. The image does not reveal the microstructures on the surface, but as the scan area was reduced, the microstructures were revealed. The topography image with a scan area of $(2.5 \mu\text{m})^2$ in Fig. 5.6-1(b) shows various sizes of microstructures, also called nodules. The bright middle part is induced by unevenness of the surface, rather than the height of the nodules. On the flat surface such as on the upper right corner, the contrast of the nodules is clearly seen. This region is further zoomed with software, Fig. 5.6-1(d), and the nodules are seen in detail. From the profile next to the zoomed image, the height of the nodules can be recognized as less than 3 nm. While the topography image is influenced by the surface unevenness in terms of showing the nodules, the FMM image is less influenced by the

surface evenness within the tolerable limit. The stiffness image in Fig. 5.6-1(c) displays the nodules with better contrast than the topography image. In addition, an irregularity of the amplitude within the nodules is apparent, and some nodules are stiffer than others. The stiff surface is shown as bright and the soft surface is shown as dark in the stiffness image. The inner side of the nodules is darker than the outer in the stiffness image, which indicates that the inside is softer than the outside of the nodules. In addition, the inner side of the nodules is darker than the outer side, which indicates that the inside is softer than the outside of the nodules. However, the contact area effect cannot be ruled out as a reason for the observed amplitude variations.

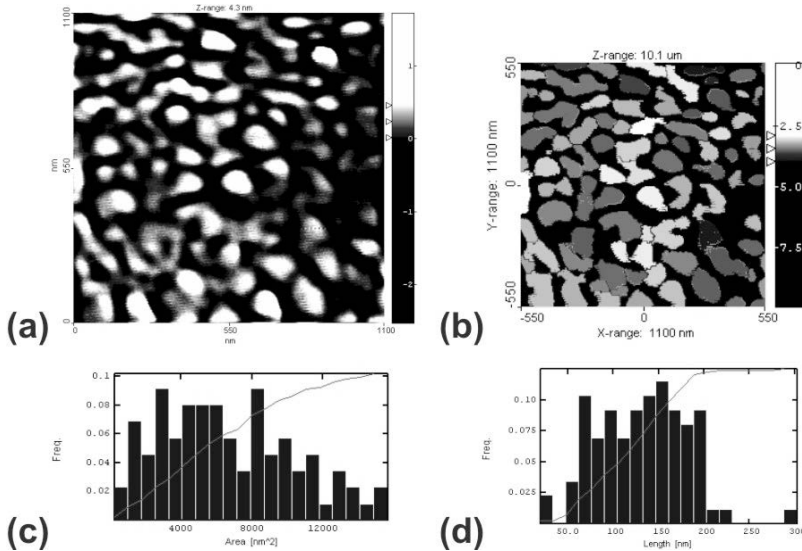


Figure 5.6-2. Statistical analysis of nodule size. (a) Nodules in the leveled topography. The topography image of Fig. 5.4(d) is leveled. (b) An image with categorized nodules. The different darkness indicates the different size distribution. (c) Area histogram. (d) Length histogram.

The surface is flat enough to obtain the images, but not perfectly flat. This hindered the statistical analysis of the size of the nodules (Fig. 5.6-2). By placing an x - y reference plane at a proper z position, the size of the microstructures can be measured. The size of the nodules changes depending on which z position the x - y plane is placed. In other words, the height is measured from the x - y plain to the peak of the nodule, and the perimeter of the nodule is measured from the area of the nodule on the x - y plain. However, when the surface is not flat, some microstructures may not be recognized by this method, or some may be measured smaller or larger than they are. Because the nodules are cone-shaped, as the z position of the x - y plane increases, the size of the nodules decrease. Thus, only the flat area in the upper right corner in Fig. 5.6-1(b) with typical representation of the surface was taken for the statistical analysis of the nodules. For a statistical analysis, shown in Fig. 5.6-2, an x - y reference plane was placed at 4.7 nm of the z position of the software-based zoomed image and the sizes of nodules were measured on the plane. As the x - y plane cut the topography in the z position, the adjusted topography image is shown as Fig. 5.6-2(a). The z position of the plane was selected as low as possible, but high enough

to recognize all nodules contained within the area. The average length of the nodules was ~125 nm. The nodules are categorized by size in a gray scale in Fig. 5.6-2(b). The histogram of the area shows the area distribution of the nodules, Fig. 5.6-2(c). 90 percent of nodules have an area of 10,000 nm² or less. The length distribution is shown in Fig. 5.6-2(d). More than 90 percent of nodules have a length between 75 and 200 nm.

6. Epoxy Surface and Interphase

6.1. Epoxy/Copper Interphase

Interphase characteristics are determined by various parameters such as the adherent properties, adhesive properties, and processing properties. Depending on the types of epoxy resin and the hardener, it was shown that the stiffness variations in the interphase between cured epoxy and copper are different. When the EPIKOTE828-EPIKURE F205 system is cured on copper, it produces an interphase with high stiffness in the close vicinity of the interface, and then the stiffness decreases to a minimum value and increases as approaching to the bulk. On the other hand, the DER332-DDS system generally creates a much higher stiffness than the bulk at the beginning of the interphase, then more or less continuously decreasing stiffness as it approaches the bulk. Summary of the analyses are shown in Table 6-1. It can be easily seen which information is available for the interphase analysis. The stiffness profile of interphase is obtained from the FMM amplitude image. The image is further interpreted with EDX and DMA results if available. The stiffness profile in the interphase can give additional information of the diffusion during the cure, combining the EDX and DMA results.

Table 6-1. Summary of analyses.

Epoxy system in the epoxy-copper composite	SFM-FMM analysis performed?	EDX performed?	Modulus information from DMA available?
EPIKOTE828 and EPIKURE F-205	Yes	No	Yes
DER332 and DDS	Yes	Yes	Yes

The result of the DMA on the EPIKOTE828-EPIKURE F205 system showed the glass transition temperature (T_g) and the storage moduli of Young's modulus (E') of samples with various amine contents in the amine-to-epoxy ratio (r , defined in Chapter 3). As it is generally considered, T_g was found as the temperature at which the loss modulus (E'') went through a maximum at a frequency of 1.0 Hz. The relationship between T_g and r is a bell-shape curve, Fig. 6-1(a), showing the maximum near the stoichiometric ratio ($r = 1.0$). As r is further away from the stoichiometric ratio, T_g becomes lower. The maximum T_g indicates the highest crosslink density, which seems to be close to the stoichiometric ratio. On the other hand, the relationship between E' at 20°C and r shows a local minimum at the stoichiometric ratio, Fig. 6-1(b). Different oscillation frequencies of 0.1, 1.0, 10 and 20 Hz were applied during DMA testing. The result shows that the stiffness is slightly lower at the stoichiometric ratio than the surrounding off-stoichiometric ratio. As r moves away from the stoichiometric ratio, E' increases. After reaching its peak point, E' decreases with a notably reduced or increased amine content. In addition, the frequency dependency of the E' measurement is evident according to the analysis. As the oscillation frequency increases, the measured modulus also increases. This effect is more noticeable when r is further away from the stoichiometric ratio.

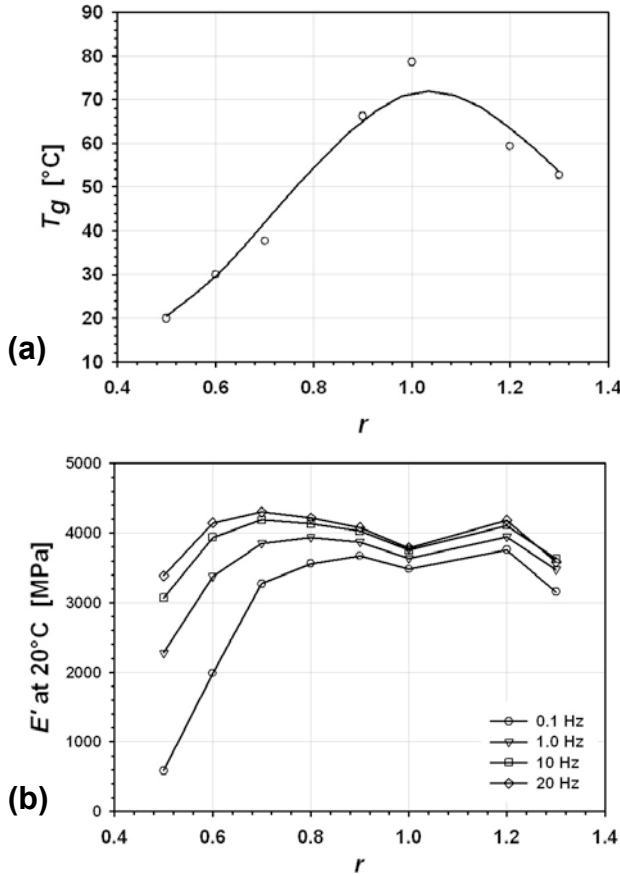


Figure 6-1. Results of the DMA as a function of the amine-to-epoxy ratio (r) for EPIKOTE828 and EPIKURE F-205. The stoichiometric ratio is when r equals 1.0. (a) Glass transition temperature (T_g) found as the temperature at the peak of loss modulus (E'') at 1 Hz. (b) Storage modulus of the Young's modulus (E') at 20°C with oscillation frequencies of 0.1, 1.0, 10 and 20 Hz.

The FMM amplitude profile of EPIKOTE828-EPIKURE F205 is analyzed in detail in Fig. 6-2, more closely studying the interphase image of Fig. 5.5-3. The interphase in epoxy, which is induced by the copper surface, reveals a gradient of stiffness as shown previously. The profile was obtained from the amplitude image in Fig. 5.5-3. The beginning of the epoxy region was recognized by a large difference in FMM amplitude between epoxy and copper, which is not shown in the profile. The profile can be seen to consist of two parts, which are divided by the vertical dash line. The first part is near the copper surface. The FMM amplitude starts with a high value and a quick decrease follows. The second part starts at the lowest amplitude and continues to the bulk. It is the region with increasing amplitudes. The two parts are treated separately to fit Gaussian curves. The original data was fitted to a trendline in order to reduce the scattered noise signals. Then, following the least squares procedures, a Gaussian algorithm was used to fit the amplitude profile. The Gaussian function is expressed by

$$y = y_0 - ae^{-\frac{1}{2}\left(\frac{x-x_0}{b}\right)^2} \quad (6.1)$$

where y_0 is the offset, x_0 is at the center, a is the line depth, and $b\sqrt{2\ln 2}$ is the full width at half-maximum (FWHM). After the fit curve of the first part was constructed, x_0 of the fit curve for the second part was given as the end value of x in the first part, so that the peak can occur at the end of the first part. The width of the interphase is determined as $\sim 1.9 \mu\text{m}$, which is the sum of the first part and three times the FWHM of the fit function of the second part, which gives 1 percent deviation from the bulk amplitude which is y_0 from the fit function of the second part.

Table 6-2. Gaussian fit parameters for the amplitude profile.

	Line depth [a.u.]	FWHM [μm]	Center	Offset
First part	1.86	0.58	0.50	-1.37×10^{-8}
Second part	0.30	0.49	0.44	-1.54

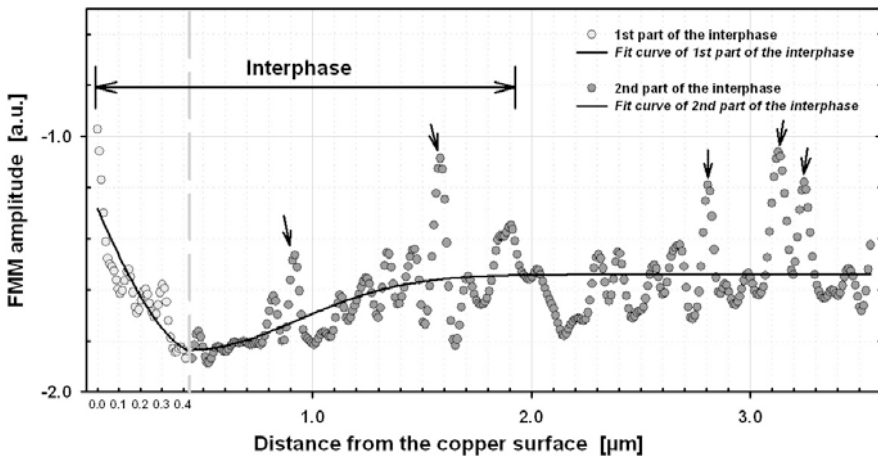


Figure 6-2. FMM amplitude profile from Fig. 5.5-3 with Gaussian fit curves. The first part is before the dash line and the second part is after the dash line. The arrows indicate topographical artifacts. The parameters from the fit curves are given in Table 6-2.

In the first part of the FMM amplitude profile, a significantly higher stiffness than that of the bulk was observed in the close proximity to the interface and the stiffness decreases rapidly until $\sim 0.43 \mu\text{m}$ below that of the bulk value. The high stiffness within $\sim 0.2 \mu\text{m}$ from the interface could have been caused by several factors. The interface induced stoichiometric imbalance could result in the high stiffness material. As shown in Fig. 6-1(b), Young's modulus is higher when the amine content is just over or under the epoxy equivalent ratio than at the stoichiometric ratio. The mixture of epoxy resin and the amine-curing agent was prepared with the stoichiometric ratio. Thus, the ratio of resin and curing agent was altered in the interphase, being influenced by the copper surface. It is difficult to determine whether the epoxy resin or curing agent was preferentially absorbed toward the copper surface. The DMA result shows that the stiffness increases nearly symmetrically on both sides of the

stoichiometric region, so either an increased or a decreased amine content might have created similar results in FMM analysis. In addition, Roche et al. showed that when the mixture of epoxy and hardener were applied to a metal surface, the polymerization is catalyzed by the presence of hydroxide acid groups and this leads to an interphase formation. As a result, the crosslink density in the close proximity to the interface could have been increased as well as the stiffness. The chemical environment of the copper surface might have enhanced the polymerization of the mixture in contact with the surface. As the liquid mixture was brought onto the metal surface, the curing agent is partially protonated by the hydroxyl group on the metal surface [6.1,6.2,6.3]. The presence of hydroxide acid on the metal surface turned out to catalyze the polymerization, influencing an interphase formation [6.1]. However, other studies demonstrated that oxidative degradation of polymer on copper substrates often produced carboxylic acids, which appeared to reduce the stability of the polymer-metal interphase [6.4,6.5]. The carboxylic acids can further react with the metal surface to produce soluble metal salts. The main cause of the degradation is considered to be the diffusion of the metal salts into the polymer matrix [6.6].

The second part of the interphase in Fig. 6-2 begins at where the FMM amplitude starts to increase after reaching the lowest point at $\sim 0.43 \mu\text{m}$. The FMM amplitude increases at a slow rate in comparison to the decreasing rate of the FMM amplitude in the first part. When the second part is considered to be out of reach from the chemical environment induced by the copper surface, the stiffness gradient is mainly influenced by the stoichiometric imbalance. Assuming the mobility of the amine is higher than the epoxy because the epoxy molecules are a lot larger than the amine molecules, the concentration of amine is either increased or decreased in the low stiffness region. Considering Young's modulus at various amine ratios from the result of DMA, the amine-to-epoxy ratio (r) must have been modified to either lower than 0.5 or higher than 1.2, in order to decrease the stiffness of the material evidently (see Fig. 6-1). If Young's modulus is proportional to the amine concentration, the profile of the amine concentration must resemble the stiffness profile. This can be seen when r is less than 1.0 in the DMA result. However, if the Young's modulus decreases with the increase of r , the amine concentration profile should have an inversely proportional relationship with the stiffness. This can be seen when r is greater than 1.0 from the DMA result. The data in the second part contains sudden high peaks, which are shown with arrows. The peaks are generated by topographic artifacts. The surface of the cured epoxy surface contains tiny dips as shown previously in Fig. 5.3-7. When the tip scans across the dips, the FMM amplitude is increased dramatically. The artifacts are induced by the sudden increase of the tip-sample contact area. Because the dips exist throughout the surface, when a line profile is drawn like in Fig. 6-2, it includes the high FMM amplitudes from the tiny dips.

The FMM amplitude profile of the interphase between DER332-DDS and copper, Fig. 6-3, shows different characteristics than the interphase between EPIKOTE828-EPIKURE F205 and copper. Two different typical behaviors of the profile were found. One indicates a high stiffness near the copper, and then a decrease of the stiffness until it reaches the bulk stiffness. The other similarly shows a high stiffness near copper, however after reaching the lowest point it increases until the bulk value.

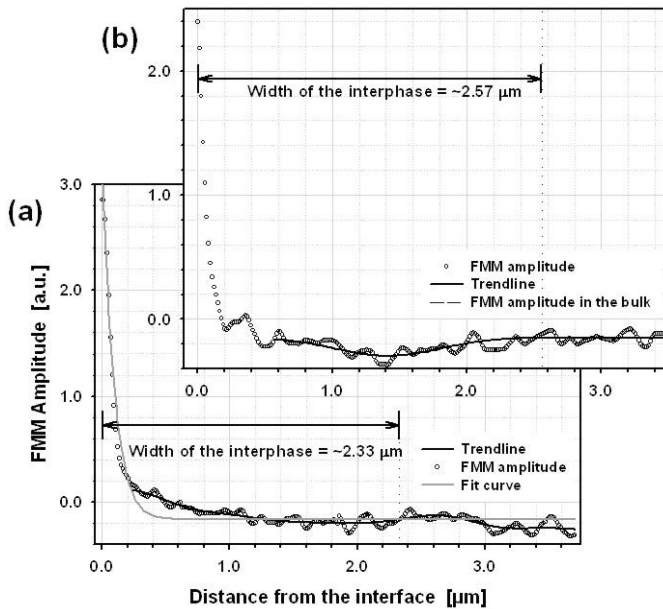


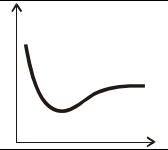
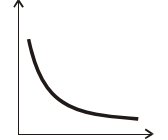
Figure 6-3. FMM amplitude profiles of DER332-DDS/Cu interphase from a sample amplitude image. (a) FMM profile with a fit curve with an error function and a trendline. A decrease of stiffness behavior is shown. (b) FMM amplitude profile with a trendline. A decrease and an increase of stiffness behavior are shown. The reference line of bulk FMM amplitude is at -0.15 .

In order to analyze the interphase, first the interface with the copper surface needs to be determined. A topography image gives only the information about height variation on the surface. When two different materials have smooth surfaces and same levels of height, they are represented alike, thus other information is required to determine the exact position of the interphase other than the topography. The beginning of the interphase is determined by analyzing different images of SFM besides the topography image. The interfacial region contains some unevenness, so it is a good starting place to look for the beginning of the interphase in the topography image. The normal force image is used in order to determine where a stable feedback control starts. The feedback control can be disrupted by the small unevenness. An acceptable feedback control and a constant tip-sample contact area mean also a valid FMM analysis. Because copper and cured epoxy are very different materials the lateral force images also provides different images between copper and epoxy surface. The copper surface is smoother than the epoxy surface and it causes less torsion of the cantilever, the lateral force signal is smaller on the copper than on the epoxy. According to these criteria, the position of interface was determined and the FMM amplitude profiles were analyzed.

The two amplitude profiles in Fig. 6-3 indicate a high stiffness near the interface and a steep decline until $\sim 0.2 \mu\text{m}$. An influence from copper can be considered due to a high stiffness in close proximity from copper. However, the width of the high amplitude region is too large to be considered as artifact from an influence of the copper during the SFM-FMM analysis, reflecting the tip-sample contact area and the penetration depth of the tip. In Fig. 6-3(a), the amplitude profile continues decreasing until the bulk, which approximately

begins at 2.33 μm . A trendline is drawn (dark line) to show the behavior of the amplitude profile. If the main cause of the stiffness variation is a concentration variation induced by a preferential absorption of the amine or epoxy towards the copper surface, a diffusion model can be applied for the further analysis, assuming the stiffness is proportional to the concentration. Using an error-function [6.7], which is often used to deduce diffusion behavior of finite source at a border of infinite number of solution, a fit curve (gray line) is generated. The region near copper showing high stiffness and the steep decline of amplitude correlates well with the fit curve. However, as the decline of amplitude slows down, the fit curve shows a deviation from the amplitude profile from 0.2 to 1.0 μm away from the interface. This deviation may have been caused by the fact that the profile describes the mechanical property of the interphase, which is the result of the diffusion, other than the concentration variation of amine or epoxy. On the other hand, the diffusion is induced by the copper surface. The error-function assumes a concentration change in the interfacial region, induced by the concentration difference of the two species. The width of interphase can be recognized as $\sim 2.33 \mu\text{m}$. The width of the interphase was determined by the distance between the interface and the point, where 1 percent deviation occurred comparing to the amplitude in the bulk region. This amplitude profile does not seem to include a lowest stiffness point in the interphase as the profile in Fig. 5.5-9(d) denotes. The low point at $\sim 1.9 \mu\text{m}$ can be seen as the lowest point, but its change is not large enough to be considered as a true characteristic. On the other hand, the profile in Fig. 6-2(b) contains a lowest point at $\sim 1.2 \mu\text{m}$ and the width of the interphase is $\sim 2.33 \mu\text{m}$. The width was determined by 1 percent deviation from the bulk value of 0.16, which was taken from the fit curve. As two similar profiles suggest, the profiles of the interphase is not always identical, but they are fundamentally alike.

Table 6-3. Interphase comparison between two epoxy systems.

Epoxy system in the interphase	Width of higher stiffness than the bulk region near Copper [μm]	Location of the minimum stiffness in the interphase [μm]	Width of the interphase [μm]	Shape of stiffness profile in interphase (distance vs. E)
EPIKOTE828 and EPIKURE F-205	~ 0.2	~ 0.4	~ 1.9	
DER332 and DDS	~ 0.25	n.a.	2.3-4.0	

The near copper region shows much higher stiffness than the bulk. Considering the magnitude of the difference in the stiffness, it correlates well with the DMA result of E' , which demonstrates an increase of stiffness as the amine concentration decreases. Some increase of stiffness has been seen with an increased amine concentration, but the magnitude of the increase is much smaller than that of a decreased amine concentration. In addition, EDX results with SEM and TEM also exemplify the low concentration of amine

near the copper surface, which means within $0.5\ \mu\text{m}$ from the interface. In this region, a different chemical environment should be considered as well for a reason of the stiffness variation besides the stoichiometric imbalance of the mixture. As earlier studies show, another reason could be from the presence of the hydroxyls on the metal oxide surface, which may have catalyzed the curing reaction [6.1]. This catalytic effect may affect a smaller region than the preferential segregation of amine.

As it has been shown, the amine concentration in the resin-hardener mixture influences the stiffness of the cured epoxy. When the epoxy-hardener mixture is brought to a metal surface, an interphase is created due to the concentration gradient. The relationships are modeled and several different cases are discussed in Fig. 6-4. Possible concentration gradients (e.g. amine) in an interphase with metal surfaces are shown in (A), (B), (C), and (D). C_a denotes the concentration of amine in the mixture and x denotes the distance from the interface. Epoxy systems can show various stiffness behavior with the concentration and some possible profiles are proposed in (1), (2), (3), and (4).

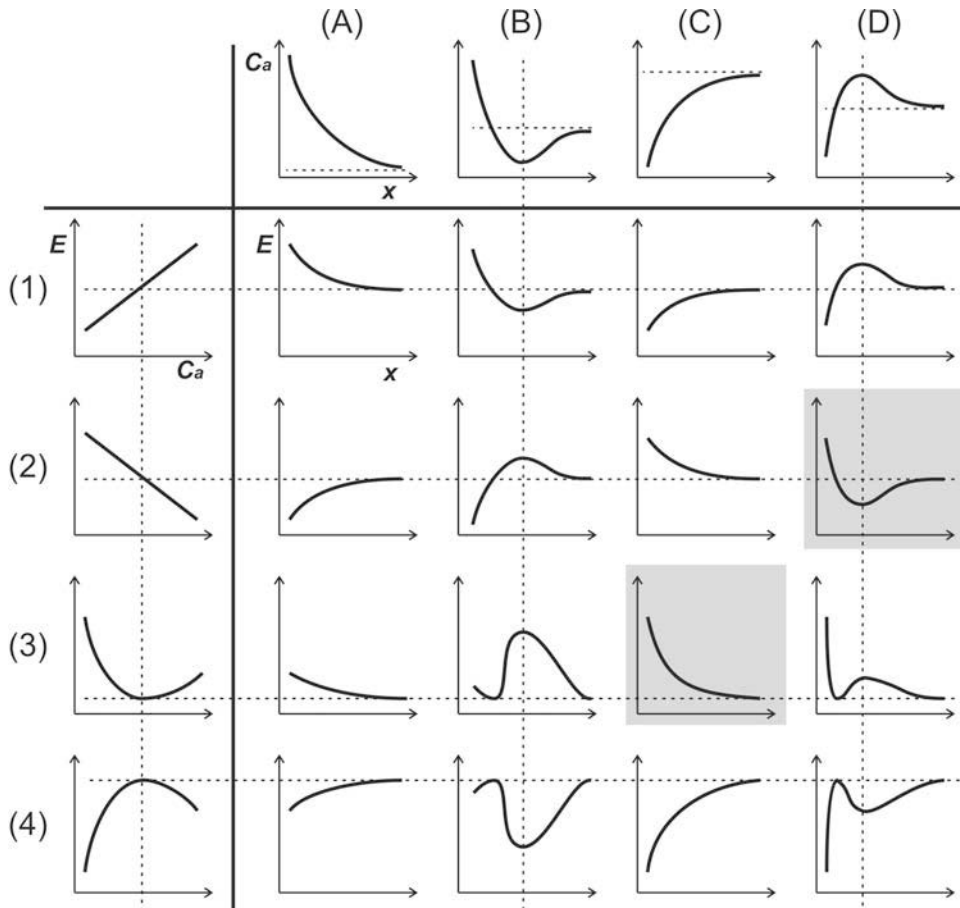


Figure 6-4. Overview of various possible relationships of the stiffness and the concentration in the interphase. C3 represents the DER332-DDS system, and D2 represents the EPIKOTE828-EPIKURE F205 system.

The models are constructed with the following assumptions. For the concentration (C_a) profiles in terms of the distance (x) from the metal surfaces, the epoxy-amine systems are mixed in the stoichiometric ratio, thus the bulk material has same concentration ratio as the mixture. The concentration of the bulk is indicated by dash lines. Thus, in (A) the amine concentration is higher near the metal surface than in the bulk. In (B) the vertical dashed line represents the lowest amine concentration. In (D) the vertical dashed line indicates the highest amine concentration in the interphase. The models from (1) to (4) describe the relationships between the modulus (E) and the amine concentration (C_a). In the graphs, the vertical dashed line denotes the stoichiometric ratio of epoxy resin and amine curing agent, and the horizontal dashed line is the modulus at the epoxy equivalent ratio of amine.

The results of the studies of interphases with different epoxy systems on copper surface show that the stiffness profile of the interphase is not always identical. The models are constructed to consider the possibilities of different interfacial reactions of epoxy-hardener mixtures on a metal surface and the following stiffness variation as a consequence. The models indicate that even if the stiffness profiles in interphases show a similar behavior, the source can be different. The stiffness profile produced by (A) and (1) is referred as A1. A2, A4, C1, and C4 deduce the low stiffness near the metal surface and the stiffness increases as it approaches to the bulk. This kind of stiffness profile is generated with various adsorption behaviors of amine in the interphase and different relationships between stiffness and concentration.

The interphase between EPIKOTE828-EPIKURE F205 system and copper seems to be similar to D2. This indicates that two zones exist; a zone of low amine concentration near the copper surface and a zone of increased amine concentration, which is above the bulk level. This profile can be obtained when the relationship between the stiffness and the concentration is disproportional. The interphase generated by DER332-DDS system and copper seems to be similar to A1, A3, C2 and C3 when the stiffness does not have a lowest point in the interphase. It has been found by the EDX that the amine concentration is low near the copper surface, so the equivalent concentration profile would be (C). Previously it was discussed that the stiffness and amine concentration relationship was found to be similar to (3). Thus, the case of DER332-DDS system is C3. Considering the disproportional relationship of the stiffness and the concentration below the stoichiometric ratio, the model associates well with the outcome of the experiments.

6.2. Nodules on the epoxy surface

In addition to the stiffness analysis of the interphase between the cured epoxy and the copper, this SFM analysis exhibited microstructures on the cured epoxy surface. The microstructures on the surface were observed by photomicrography [6.8] and electron microscopy [6.9,6.10] before scanning force microscopes became available. In some cases, epoxy resin with lower crosslink density showed more distinct microstructures on the surface than epoxy resins with high crosslink density. However, it is not certain if there is any correlation between crosslink density and the nodule size. As Dušek suspected, nodular structures might have been formed from a result of interaction of electrons or other ionic particles from the electron beam exposure [6.9]. Thus, the morphological inhomogeneity of cured thermoset may not be generalized from investigations with electron

microscopy, especially in terms of crosslink density [6.11]. On the other hand, Giraud et al. [6.12] reported microstructures on epoxy-amine surfaces that were cured on silicon substrates under ambient conditions followed by post-curing, and the surface was investigated by SFM in tapping mode. This work used a DGEBA based epoxy and a tri-amine based on propylene oxide curing agent. Epoxy thin films were prepared in solvent and polished in several steps. The thin film cured in contact with air revealed nodular microstructures with sizes ranging from 30 to 70 nm. The sizes of the nodules of the epoxy cured on silicon were not mentioned. However, Giraud et al. reported that larger nodules appeared on the film/substrate surface than on the film/air surface. Therefore, they believed that the chemical composition and phase separation at the two interfaces should have different effects. The results shown in section 5.6 and the work by Giraud et al. [6.12] were derived from similar materials, thus they show similar result. However, because the film thickness and the preparation procedures were different, the two results are not directly comparable. The other reason for the difficulty of comparing the results of two similar experiments is that the analytical methods are different. Giraud et al. [6.12] analyzed the nodules by acquiring topography and phase images with tapping mode SFM. The size of nodules is nanometer scale, so different criteria of defining the border between the nodules or the height of the nodules might influence the result significantly. Therefore, a study of the microstructures requires a well-defined criterion.

Previously it was suggested that the highly crosslinked region is surrounded by a less crosslinked region [6.13]. A reason was proposed that some unreacted and partially polymerized parts might be unable to join the homogeneous parts during the polymerization and remained in the perimeter of the network units. Racich and Koutsky [6.14] observed that the average size of nodules decreased as the concentration of the amine-curing agent increased. On the other hand, the nodule characteristics may also depend on curing temperature. Lüttgert et al. observed that the nodular structures on epoxy surface were much smaller at high curing temperature than low curing temperature [6.10]. They suggested a model that described the nodule formation. Considering the exothermic nature of the epoxy-amine curing reaction, the local heat distribution from the core of the reaction during the cure may be the cause of the nodule formation. As the cure is initiated, nuclei of the reaction develop throughout the mixture. Local regions near nuclei undergo temperature rise from the first exothermic reaction of the nucleus. Because of the temperature rise, the reaction rate is increased in the vicinity of the nuclei, and the curing reaction continues. Likewise, the cure propagates from the nucleus, and the propagation of the reaction ends when it meets its neighboring propagation of the curing reaction. Therefore, the nodules are created. The nodule formation is a localized reaction and it depends on the condition of the local region. The model takes into consideration the heat diffusion and the reaction rate. The size of the nodules increases with the reduced number of the nuclei since the distance between the nuclei grows. High amine content increases the probability of the nucleus formation.

The curing reactions are not identical in all epoxy-amine systems. The local temperature rise is affected by a high reaction rate. Because aliphatic amines are inclined to produce higher reaction rates than aromatic amines, the nodular structures are more likely to be seen in the case of epoxy cured with aliphatic amines. Nodular structures were often observed when the epoxy system was cured with (cyclo-)aliphatic amines as the earlier

studies report [6.12,6.15,6.16]. The property variation within a single nodule cannot be easily determined. The difference might be subtle to be detected. Cuthrell [6.13] claimed that the inner part is more rigid than the outer part of the nodule. The rate of heat diffusion from the core of the initial reaction may affect the temperature of the local region during the curing process. The availability of the amine molecules in the local regions can affect the nodule. The region near the reaction core will experience higher temperatures than the region far away from the core due to the initial curing reaction. The mobility of the reacted amine at the core will be hindered by the increasing number of crosslinks, which increase viscosity. The outer region of the nodules might have less amine molecules available than the core region. As a result, the final mechanical properties in the core regions can be different from those in the outer regions.

The average size of the nodules varies according to the amine to epoxy mixing ratio. Mijović and Koutsky [6.16] used TEM to observe that larger nodules appeared in the case of samples with low amine concentration than for samples with high amine concentration. An SFM study by VanLandingham et al. [6.15] reported also similar trend according to the characterization of the samples with various amine concentrations. In case of the epoxy cured in contact with a substrate or a solid surface, a modified material forms between the solid and the bulk epoxy as so-called interphase. Because the solid surface can cause a preferential absorption of either epoxy or amine, a modified mixing ratio can occur. At the same time, the solid surface acts as a heat sink, which results in a heat loss in the vicinity of the interface. Thus, the temperature decreases in the region of epoxy mixture, which is in contact with the solid, and this can reduce the reaction rate. The larger nodules were observed previously in the area, which was in contact with the substrate or a solid surface [6.12, 6.17,6.18]. Racich and Koutsky [6.17] reported that the size of nodule increased near interfaces (~100 nm) in comparison to the size of the nodules far from the interphase (10–60 nm). These results correlate well with the nucleus-based model of nodule formation by Lüttgert and Bonart [6.10] considering the effect of amine concentration and temperature on the size of the nodules.

7. Conclusion

This research was aimed to broaden the comprehension of surface and interphase properties. The objective was to determine the existence of the interphase and to describe its stiffness property in the interphase by using scanning force microscopy in force modulation mode (SFM-FMM). The region of interest was the interfacial region in the polymer that was different from the bulk polymer between the metal surface and the bulk polymer. Interphases are considered to play a vital role in composite materials. The mechanical performance of the fiber-reinforced matrix is depended not only on the fiber and the matrix, but also on the effectiveness of the interphase in transferring the stress across the interface. Additionally, the interphase is critical for the durability of polymeric adhesive joints in integrated circuits.

Epoxy is one of the most commonly used polymeric materials in composites. Its electrical and adhesion properties are taken advantage of in numerous products. In this work, the epoxy systems used are the resins of EPIKOTE828 (Resolution Europe B.V.) and DER332 (Dow Chemical) with the curing agents of EPIKURE F205 (Resolution Europe B.V.) and DDS (4,4'-diaminodiphenyl sulfone, Fluka Chemika), respectively. The epoxy resins were based on diglycidyl ether of bisphenol A (DGEBA), and the hardeners were amine-based curing agents. Two systems were used to determine if differences existed in the interphase of two different systems. In addition, DDS contains sulfur, which can be detected by energy dispersive analysis of X-rays (EDX), thus the content of the curing agent in the interphase was described by measuring the sulfur content.

When the EPIKOTE828-EPIKURE F205 system was cured in contact with copper, the FMM amplitude profile revealed that the interphase consisted of a high stiffness region near the interface with the copper, then adjacent to the high stiffness region existed a relatively low stiffness region when compared to the bulk stiffness. Thus, the profile could be depicted as high stiffness close to the interface, decreasing until the point of minimum stiffness and then increasing towards the bulk. The width of the stiffness variation extended to $\sim 1.9 \mu\text{m}$ with a local minimum at $\sim 0.43 \mu\text{m}$. Young's moduli of various amine-to-epoxy ratios (r) determined by dynamic mechanical analysis (DMA) were compared with the FMM-amplitude profiles of the interphase. The variation of r resulted in alteration of Young's modulus. This indicated that a perturbation of stoichiometry between epoxy and amine was apparent in the interphase. Thus, the interphase had a different stoichiometry from the initial since its stiffness was different from the bulk material. DMA revealed that Young's modulus was the lowest at the stoichiometric ratio (r_0) in the vicinity of r_0 . Because the modulus of mixtures with slightly higher concentration than r_0 was close to the modulus of mixtures with slightly lower than r_0 , the content of amine was difficult to be determined by the Young's modulus profile. Although it was hard to determine if the high stiffness region was rich of amine or epoxy because the Young's modulus profile from the DMA exhibited nearly symmetry across r_0 , a preferential segregation of amine or epoxy towards the copper surface was evident, resulting in a stoichiometric imbalance in the interphase.

L. T. Drzal had proposed a rigid layer between the solid surface and the bulk epoxy, while M. R. Piggott had suggested a soft interphase. Both postulations could have been true for

particular systems, considering the FMM amplitude profile of the interphase between the EPIKOTE828-EPIKURE F205 and copper surface. The previous studies had not illustrated the profile of the interphase, and the gradient of the interphase had not been discussed. Traits of the dominant part of the interphase may have been recognized as the traits of the interphase as a whole. Likewise, if the softer region had occupied the majority of the interphase, it may have been observed that the interphase on the whole was soft. Because the previous studies had not been conducted with the same materials, it was also likely that the interphases had different properties. The DER332-DDS system indicated a different stiffness gradient in its interphase on the copper surface in comparison to EPIKOTE828-EPIKURE F205. Interphase properties seem to vary depending on the bulk epoxy material and cannot be generalized. The dependency of the bulk material on the nature of the interphase was shown in this research. The processing conditions such as curing temperature (T_{cure}) or the amine-to-epoxy ratio (r) could also play a role in the formation of the interphase. The interphase properties can be further investigated in this direction.

Some main conclusions can be drawn from the interphase analyses:

- A stiffness gradient exists in the interphase between epoxy and copper, and the profile of the interphase varies depending on the epoxy system. The interphase of the EPIKOTE828-EPIKURE F205 system is found to be $\sim 1.9 \mu\text{m}$. Its profile depicts that high stiffness appears in the close vicinity to the copper, and followed by a soft region before the bulk stiffness is reached. The DER332-DDS system produced an interphase, which appears to have a significantly higher stiffness than that of the bulk in the vicinity close to the copper. A steep decline of the stiffness occurs until $\sim 0.2 \mu\text{m}$ away from the interface and a slow decline continues until the bulk stiffness is reached. The width of the stiffness gradient appears to be between $2.3\text{--}4.0 \mu\text{m}$.
- EDX can detect the sulfur in DDS and its content identifies preferential segregation of the epoxy-amine mixture. EDX with SEM and TEM reveals a variation of the sulfur content in the vicinity of the copper surface and this implies the variation of the amine content. Lower amine content is evident in close vicinity to the copper surface within the interphase in comparison to the amine content of the bulk. This is in contrast to the previous findings, which claimed an increase of the amine concentration in close vicinity of copper.
- The amine concentration from the EDX result was correlated to Young's modulus variations in terms of the amine content as determined by DMA. The stiffness profile, which associates with Young's modulus, correlates well with the amine content in the interphase as the modulus increases with less than the epoxy equivalent amine content in the cured DER332-DDS. The EDX result indicates clearly that a low amine concentration region exists within $\sim 1.0 \mu\text{m}$ from the copper surface. The region with low amine content may be further extended considering the width of the stiffness variation.

The SFM-FMM characterization was proven to be an adequate method to analyze local stiffness of polymer. The advantage resulted especially from the recognition of stiffness gradients in small areas. The stiffness of the local area was depicted by its amplitude image, which was produced by amplitude variation of SFM-cantilever according to the

stiffness. With its excellent sensitivity to stiffness variation, it was a good choice for an analysis of a polymer/metal interphase. Its high lateral resolution added a unique ability to find localized characteristics. Considering the limited resolution of the depth-sensing indentation (DSI), this lateral resolution was significant for the analysis of narrow interphases. Flatness was identified as a critical criterion in order to run the SFM-FMM analysis because topographical artifacts could be generated when the sample surface was not very flat. As a rule of thumb, the local slope needed to be less than $\sim|3^\circ|$ for an optimal performance of FMM. In addition, when topographic features like small dips existed on the surface, they could cause variation of the tip-sample contact area, which could be another source of artifacts. During the SFM-FMM analysis other images were obtained besides the amplitude image, such as topography, normal force, lateral force, and phase shift images. These images provided additional information of the surface and the combined evaluation of all available contrasts allowed imaging artifacts to be separated from true stiffness variations.

A novel sample preparation approach was applied to produce an optimum surface utilizing a combination of the EBL and lift-off technique for preparation of copper microstructures. It allowed a comprehensive control over the geometry of the sample. Most importantly, a flat sample surface with continuous interfaces between epoxy and copper was achieved. The flatness and the continuous interface are important requirements of the sample for the SFM-FMM analysis. In addition, a desired distance between the copper electrodes was designed and implemented using the EBL. The thickness of the photoresist determines the thickness of the copper because the copper layer cannot be deposited thicker than the photoresist. The multifold sample preparation steps certainly complicated the procedure, however it was an effective method to produce samples for an interphase analysis with SFM-FMM.

Microstructures on the cured epoxy surface were revealed by the SFM-FMM analysis. The so-called nodules were also presented in the FMM amplitude image with better resolution than in the topography image. Thus, the border between the nodules could be better recognized. Although the nodules had been seen by earlier studies with various microscopic methods, the process conditions that create the nodules are still not known. A model of the nodule formation had been proposed; the nodules grow until the growing nuclei share a border, and the size of the nodules depends on the number of the nuclei at the beginning of the curing reaction. The SFM-FMM analysis may contribute to further studies of the nodules, e.g. the relationship of nodule formation and various process parameters such as curing temperature, ratio of epoxy resin and hardener, etc.

The epoxy interphase near the copper surface forms during the early stage of the curing process. As the mixture of the epoxy and the amine-based hardener are brought in contact with copper, the copper surface causes absorption of the mixture while it is still low in viscosity. Being influenced by the absorption, a preferential diffusion occurs near the copper surface and the interphase forms with a modified amine concentration, which is different from the initial concentration. Acquiring a different stoichiometry between epoxy and amine, the interphase has different mechanical properties such as stiffness compared to the bulk. An influence from metal salt had been also suggested for the formation of the interphase. It is likely that a combination of the modified stoichiometry and the metal salt is responsible for the interphase formation. Since the width of the interphase is in such a small scale, the

characterization of the interphase requires a high lateral resolution. SFM-FMM demonstrates that the interphase is not a uniform material, but a variation exists in the interphase. In designing a composite material, the adhesive liability of the interphase is in general considered one of the most important parameters. Its failure can occur at the point where the stress level is the highest, while the composite undergoes a load. In order to optimize the design of a composite, the interphase must be considered as a heterogeneous material. The extreme heterogeneity of the interphase will likely increase the possibility of failure. The heterogeneity can be reduced by decreasing the stoichiometry variation in the interphase. This may be achieved by, for example, adjusting the amine-to-epoxy ratio as well as the curing procedure.

Moreover, stress analysis in the interphase can be further considered in conjunction with the stiffness profile in order to foresee the failure characteristics and to find possible modifications of the interphase for the desired composite. SFM-FMM can be carried out at various temperatures, and the temperature dependency of polymer properties can also be studied. As a measure of the crosslink density, the glass transition temperature (T_g) may provide further insight into local variations of the epoxy network structure. The stiffness change in terms of temperature can provide important information for the failure characterization in the polymer-metal interphase.

Symbols

a	contact radius
C_{piezo}	slope between U_{exc} and Δz
C_{spd}	slope between U_{in} and Δb
d	fiber diameter
E	Young's modulus
E'	storage modulus
E''	loss modulus
E_r	reduced modulus
E_s	Young's modulus of sample
E_t	Young's modulus of tip
F_c	force exerted on the cantilever or indenter load
h	displacement
k_c	cantilever stiffness
k_{ts}	tip-sample contact stiffness
P	load
r	amine-to-epoxy concentration ratio
R	tip apex radius
S/V	surface-to-volume ratio
T_{cure}	cure temperature
T_g	glass transition temperature
T_{g^∞}	glass transition temperature of the fully cured system
U_A	signal representing amplitude
U_{exc}	excitation voltage
U_I	imaginary part of the signal
U_{in}	captured signal
U_R	real part of the signal
U_φ	signal representing phase shift
V_f	fiber volume fraction
V_{mi}	fraction of matrix phase occupied by interphase material

w	interphase width
Δb	cantilever bending amplitude
Δz	modulation height
σ	indentation depth
ν_s	Poisson's ratio of sample
ν_t	Poisson's ratio of tip
ω	angular frequency
ω_0	cantilever resonant frequency

Abbreviations

CMC	Ceramic matrix composite
CMP	Chemical-mechanical polishing
DDS	4,4'-diamino-diphenylsulphone
DEA	Diethanolamine
DGEBA	Diglycidyl ether of Bisphenol-A
DICY	Dicyandiamide
DMA	Dynamic mechanical analysis
DSC	Differential scanning calorimetry
DSI	Depth-sensing indentation
EDX	Energy dispersive X-ray spectroscopy
FIB	Focused-ion beam
FMM	Force Modulation Mode
FTIR	Fourier transform infrared spectroscopy
FWHM	Full width at half-maximum
HREELS	High resolution electron energy loss spectroscopy
IC	Integrated circuit
ITO	Indium tin oxide
Low- <i>k</i>	low dielectric constant
MDA	methylene dianiline
MEMS	Micro-Electro-Mechanical Systems
MMC	Metal matrix composite
p-LED	Polymer-based light-emitting diode
PMC	Polymer matrix composite
PMMA	Polymethyl methacrylate
ROI	Region of interest
SFM	Scanning Force Microscopy
TEM	Transmission electron microscopy
TPD	Temperature programmed desorption
XPS	X-ray photoelectron spectroscopy

References

Chapter 1

- 1.1 K.K. Chawla, *Composite Materials: Science and Engineering*, Springer-Verlag, New York (1998).
- 1.2 D.W. Schiering, J.E. Katon, L.T. Drzal, V.B. Gupta, *J. Appl. Polym. Sci.* 34 (1987) 2367—2375.
- 1.3 J.J. Lesko, K. Jayaraman, K.L. Reifsnider, *Key Eng. Mat.* 116—117 (1996) 61—86.
- 1.4 T.P. Skourlis, R.L. McCullough, *J. Appl. Polym. Sci.* 62 (1996) 481—490.
- 1.5 L.T. Drzal, *Adv. Polym. Sci.* 75 (1986) 1—32.
- 1.6 M.R. Piggott, *Polym. Compos.* 8 (1987) 291—296.
- 1.7 L.T. Drzal, *Vacuum* 41 (1990) 1615—1618.
- 1.8 J.L. Racich, J.A. Koutsky in: *Chemistry and Properties of Crosslinked Polymers*, S.S. Labana (Ed), 303—323, Academic Press, New York (1977).
- 1.9 F. Yang, P. Pitchumani, *Comp. Sci. Tech.* 64 (2004) 1437—1452.
- 1.10 T.A. Bogetti, T. Wang, M.R. VanLandingham, J.W. Gillespie, Jr, *Compos. Part A-Appl. S.* 30 (1999) 85—94.
- 1.11 F. Yang, R. Pitchumani, *J. Appl. Polym. Sci.* 89 (2003) 3220—3236.
- 1.12 C.P. Tsui, C.Y. Tang, T.C. Lee, *J. Mater. Process Technol.* 117 (2001) 105—110.
- 1.13 T.P. Skourlis, R.L. McCullough, *Comp. Sci. Tech.* 49 (1993) 363—368.
- 1.14 D. Arayasantiparb, S. McKnight, M. Libera, *J. Adhesion Sci. Technol.* 15 (2001) 1463—1484.
- 1.15 M.R. VanLandingham, R.R. Dagastine, R.F. Eduljee, R.L. McCullough, J.W. Gillespie, Jr., *Compos. Part A-Appl. S.* 30 (1999) 75—83.

Chapter 2

- 2.1 K.K. Chawla, *Composite Materials: Science and Engineering*, Springer-Verlag, New York (1998).
- 2.2 T.W. Clyne, P.J. Withers, *An Introduction to Metal Matrix Composites*, Cambridge University Press, Cambridge (1993).
- 2.3 R.A.L. Jones, R.W. Richards, *Polymers at Surfaces and Interfaces*, Cambridge University Press, Cambridge (1999).
- 2.4 E. Jabbari, N. A. Peppas, *J.M.S—Rev. Macromol. Chem. Phys.* C34 (2) (1994) 205—241.
- 2.5 T.D. Jones, J.S. Schulze, C.W. Macosko, T.P. Lodge, *Macromolecules*, 36 (2003) 7212—7219.
- 2.6 H.S. Jeon, P.S. Dixit, H. Yim, M.S. Kent, K. Shin, S. Satija, *J. Polym. Sci. Pol. Phys.* 40 (2002) 2653—2660.
- 2.7 F. Brochard-Wyart in: *Fundamentals of Adhesion*, L-H. Lee (Ed), 181—206, Plenum Press, New York (1991).
- 2.8 R.E. Baier, A.E. Meyer in: *Fundamentals of Adhesion*, L-H. Lee (Ed), 407—425, Plenum Press, New York (1991).
- 2.9 D.S. Soane, Z. Mantynenko, *Polymers in Microelectronics: Fundamentals and Applications*, Elsevier, Amsterdam (1989).
- 2.10 J.L. Lenhart, J.H. van Zanten, J.P. Dunkers, C.G. Zimba, C.A. James, S.K. Pollack, R.S. Parnas, *J. Colloid Interf. Sci.* 221 (2000) 75—86.
- 2.11 A.A. Griffith, *Philos. T. Roy. Soc. A*, 221 (1920) 163—198.
- 2.12 P.W. Erickson, E.P. Plueddemann in: *Interfaces in Polymer Matrix Composites*, E.P. Plueddemann (Ed), 2—29, Academic Press, New York (1974).
- 2.13 C. Jones, *Compos. Sci. Technol.* 42 (1991) 275—298.
- 2.14 J. Gonzalez-Benito, *J. Colloid. Interf. Sci.* 267 (2003) 326—332.
- 2.15 L.T. Drzal, M.J. Rich, P.F. Lloyd, *J. Adhesion* 16 (1982) 1—30.
- 2.16 L.T. Drzal, *Vacuum* 41 (1990) 1615—1618.
- 2.17 E. Mäder, H.-J. Jacobasch, K. Grundke, T. Gietzelt, *Compos. Part A-Appl. S.* 27 (1996) 907—912.

- 2.18 J.P. Bell, *J. Appl. Polym. Sci.* 14 (1970) 1901—1906.
- 2.19 J.C. Bolger in: *Adhesion Aspects of Polymeric Coatings*, K.L. Mittal (Ed.), 3—18, Plenum Press, New York (1983).
- 2.20 R.G. Schmidt, J.P. Bell, *Adv. Polym. Sci.* 75, (1986) 33—71.
- 2.21 D.E. Packham in: *Adhesion Aspects of Polymeric Coatings*, K.L. Mittal (Ed.), 4—44, Plenum Press, New York (1993).
- 2.22 J. Kurdi, H. Ardelean, P. Marcus, P. Jonnard, F. Arefi-Khonsari, *Appl. Surf. Sci.* 189 (2002) 119—128.
- 2.23 P.S. Ho, B.D. Silverman, R.A. Haight, R.C. White, P.N. Sanda, A.R. Rossi, *IBM J. Res. Develop.* 32 (1988) 658—668.
- 2.24 F. Faupel, R. Willecke, A. Thran, *Mater. Sci. Eng. R22* (1998) 1—55.
- 2.25 K.D. Jandt, M. Buhk, J. Petermann, *J. Mater. Sci.* 31 (1996) 1779—1788.
- 2.26 M. Munz, B. Cappella, H. Sturm, M. Geuss, E. Schulz, *Adv. Polym. Sci.* 164 (2003) 87—210.
- 2.27 A.K. Chakraborty in: *Proceedings of the First International Conference on Polymer-Solid Interfaces*, J.J. Pireaux, P. Bertrand, J.L. Bredas (Eds.), 3—25, I.O.P Publishing Ltd., Bristol, U.K. (1992).
- 2.28 P.S. Ho, P.O. Hahn, J.W. Bartha, G.W. Rubloff, F.K. LeGoues, B.D. Silverman, *J. Vac. Sci. Technol. A* 3 (3) (1985) 739—745.
- 2.29 R.E. Geer, O.V. Kolosov, G.A.D. Griggs, G.S. Shekhawat, *J. Appl. Phys.* 91 (2002) 4549—4555.
- 2.30 M. Fahlman, W.R. Salaneck, *Surf. Sci.* 500 (2002) 904—922.
- 2.31 X. Crispin, A. Crispin, M.P. de Jong, S. Marciniak, W. Osikowicz, S. Jönsson, M. Fahlman, Th. Kugler, L.J. van Ijzenjoorn, M.J.A. de Voigt, W.R. Salaneck, *Mat. Res. Soc. Symp. Proc.* 747 (2003) v5.5.1—12.
- 2.32 A.J. Wagner, G.M. Wolfe, D.H. Fairbrother, *Appl. Surf. Sci.* 219 (2003) 317—328.
- 2.33 F. Faupel, R. Willecke, A. Thran, *Mat. Sci. Eng. R 22* (1998) 1—55.
- 2.34 Ye.P. Mamunya, V.V. Davydenko, P. Pissis, E.V. Lebedev, *Eur. Polym. J.* 38 (2002) 1887—1897.
- 2.35 H. Dong, K.-S. Moon, C.P. Wong, *J. Electron. Mater.* 34 (2005) 40—45.
- 2.36 E. Kung, C. Mercer, S. Allameh, O. Popoola, W.O. Soboyejo, *Metal. Mater. Trans. A* 32 (2001) 1997—2010.
- 2.37 S. Wu, *Polymer Interface and Adhesion*, Marcel Dekker, Inc., New York (1982).
- 2.38 M. Gundjian, K. Cole, *J. Appl. Polym. Sci.* 75 (2000) 1458—1473.
- 2.39 D.S. Soane, Z. Martynenko, *Polymers in Microelectronics*, Elsevier Science Publisher B.V., Amsterdam (1989).
- 2.40 J.A. Kelber, J.W. Rogers, Jr., B.A. Banse, B.E. Koel, *Appl. Surf. Sci.* 44 (1990) 193—204.
- 2.41 J.A. Kelber, R.K. Brow, *Appl. Surf. Sci.* 59 (1992) 273—280.
- 2.42 S.G. Hong, T.C. Wang, *J. Appl. Polym. Sci.* 52 (1994) 1339—1351.
- 2.43 J.M. Park, J.P. Bell in: *Adhesion Aspects of Polymeric Coatings*, K.L. Mittal (Ed.), 205—224, Plenum Press, New York (1983).
- 2.44 D.H. Kaelble, *Physical Chemistry of Adhesion*, John Wiley & Sons, Inc., New York (1971).
- 2.45 A.W. Adamson, *Physical Chemistry of Surface*, 2nd ed., Wiley-Interscience, New York (1967).
- 2.46 G.R. Palmese, R.L. McCullough, *J. Adhesion* 44 (1994) 29—49.
- 2.47 B. Pukánszky, *Eur. Polym. J.* 41 (2005) 645—662.
- 2.48 J.B. Vella, I.S. Adhietty, K. Junker, A.A. Volinsky, *Int. J. Fracture* 119/120 (2003) 487—499.
- 2.49 K. Maex, M.R. Baklanov, D. Shamiryan, F. Iacopi, S.H. Brongersma, Z.S. Yanovitskaya, *J. Appl. Phys.* 93 (2003) 8793—8841.
- 2.50 H. Geisler, T. Adam, I. Zienert, H.-J. Engelmann, E. Zschech, 6. *Workshop Rasterkraftmikroskopie in der Werkstoffwissenschaft*, 11—12, Erlangen, Germany (2005).
- 2.51 S. Wolf, R.N. Tauber, *Silicon Processing for the VLSI Era, Vol. 1 – Process Technology*, Lattice Press, Sunset Beach, California (2000).
- 2.52 D.N. Theodorou, *Macromolecules* 21 (1988) 1391—1400.
- 2.53 B.K. Fink, R.L. McCullough, *Compos. Part A-Appl. S.* 30 (1999) 1—2.

- 2.54 J.J. Lesko, K. Jayaraman, K.L. Reifsnider, *Key Eng. Mat.* 116—117 (1996) 61—86.
- 2.55 L.T. Drzal in: *Tough Composite Materials: Recent Developments*, 207—222, Noyes Publications, Park Ridge (1985).
- 2.56 M.R. Piggott, *Polym. Compos.* 8 (5) (1987) 291—296.
- 2.57 J.G. Williams, M.E. Donnellan, M.R. James, W.L. Morris, *Mat. Sci. Eng. A-Struct.* 126 (1990) 305—312.
- 2.58 J.L. Racich, J.A. Koutsky in: *Chemistry and Properties of Crosslinked Polymers*, S.S. Labana (Ed), 303—323, Academic Press, New York (1977).
- 2.59 H. Yim, M. Kent, W.F. McNamara, R. Ivkov, S. Satija, J. Majewski, *Macromolecules* 32 (1999) 7932—7938.
- 2.60 L.T. Drzal, *Adv. Polym. Sci.* 75 (1986) 1—32.
- 2.61 A.A. Roche, J. Bouchet, S. Bentadjine, *Int. J. Adhes. Adhes.* 22 (2002) 431—441.
- 2.62 E.H. Andrews, N.E. King in: *Polymer Surfaces*, D.T. Clark, W.J. Feast (Eds.), 48—63, Wiley, New York (1978).
- 2.63 G.R. Palmese, R.L. McCullough, *Compos. Part A-Appl. S.* 30 (1999) 3—10.
- 2.64 C.A. Kumins, J. Roteman, *J. Polym. Sci. A* 1 (1963) 527—540.

Chapter 3

- 3.1 F.M. Smekhov, I.Z. Chernin, A.V. Uvarov, A.L. Barenbaum, A.I. Nepomnyashchii, S.V. Yakubovich, *Vysokomol. Soyed. A*18: No. 10 (1976) 2338—2342.
- 3.2 L.T. Drzal, *Adv. Polym. Sci.* 75 (1986) 1—32.
- 3.3 H. Lee, K. Neville, *Epoxy Resins: Their Applications and Technology*, McGraw-Hill Book Company, Inc., New York (1957).
- 3.4 J.P. Bell, *J. Polym. Sci. A2*, 6 (1970) 417—436.
- 3.5 M.R. VanLandingham, R.F. Eduljee, J.W. Gillespie, Jr., *J. Appl. Polym. Sci.* 71 (1999) 699—712.
- 3.6 T.P. Skourlis, R.L. McCullough, *J. Appl. Polym. Sci.* 62 (1996) 481—490.
- 3.7 D.H. Droste, A.T. DiBenedetto, *J. Appl. Polym. Sci.* 13 (1969) 2149—2168.
- 3.8 L.E. Nielsen, *J. Macromol. Sci. C3* (1969) 69—103.
- 3.9 F. Meyer, G. Sanz, A. Eceiza, I. Mondragon, J. Mijović, *Polymer* 36 (1995) 1407—1414.
- 3.10 B.-G. Min, J.H. Hodgkin, Z.H. Stachurski, *J. Appl. Polym. Sci.* 48 (1993) 1303—1312.
- 3.11 T. Murayama, J.P. Bell, *J. Polym. Sci. A2*, 8 (1970) 437—445.
- 3.12 K. Dušek, *Angew. Makromol. Chem.* 240 (1996) 1—15.
- 3.13 R.J. Morgan, J.E. O'Neal, *J. Mat. Sci.* 12 (1977) 1966—1980.
- 3.14 J.L. Racich, J.A. Koutsky, *J. Appl. Polym. Sci.* 20 (1976) 2111—2129.
- 3.15 K.E. Lüttgert, PhD thesis, Technischen Universität Berlin (1977).
- 3.16 R.E. Cuthrell, *J. Appl. Polym. Sci.* 11 (1967) 949—952.
- 3.17 J. Mijović, J.A. Koutsky, *Polymer* 20 (1979) 1095—1107.
- 3.18 J.L. Racich, J.A. Koutsky in: *Chemistry and Properties of Crosslinked Polymers*, S.S. Labana (Ed.), 303—323, Academic Press, New York (1977).
- 3.19 K. Dusek, *Adv. Polym. Sci.* 78 (1986) 1—59.

Chapter 4

- 4.1 G. Binnig, C.F. Quate, Ch. Gerber, *Phys. Rev. Lett.* 56 (1986) 930—933.
- 4.2 F. Dinelli, M.R. Castell, D.A. Ritchie, N.J. Mason, G.A.D. Briggs, O.V. Kolosov, *Philos. Mag. A* 80 (2000) 2299—2323.
- 4.3 G. Binnig, *Ultramicroscopy* 42—44 (1992) 7—15.
- 4.4 P. Maivald, H.J. Butt, S.A.C. Gould, C.B. Prater, B. Drake, J.A. Gurley, V.B. Elings, P.K. Hansma, *Nanotechnology* 2 (1991) 103—106.

- 4.5 U. Rabe, S. Amelio, E. Kester, V. Scherer, S. Hirsekorn, W. Arnold, *Ultrasonics* 38 (2000) 430—437.
- 4.6 M. Munz, B. Cappella, H. Sturm, M. Geuss, E. Schulz, *Adv. Polym. Sci.* 164 (2003) 87—210.
- 4.7 F. Dinelli, H.E. Assender, N. Takeda, G.A.D. Briggs, O.V. Kolosov, *Surf. Interface Anal.* 27 (1999) 562—567.
- 4.8 M. Munz, H. Sturm, E. Schulz, G. Hinrichsen, *Compos. Part A-Appl. S.* 29A (1998) 1251—1259.
- 4.9 G.V. Lubarsky, M.R. Davidson, R.H. Bradley, *Surf. Sci.* (2004) 135—144.
- 4.10 K.L. Johnson, *Contact Mechanics*, Cambridge University Press, Cambridge (1985).
- 4.11 E. Meyer, R.M. Overney, K. Dransfeld, T. Gyalog, *Nanoscience—Friction and Rheology on the Nanometer Scale*, World Scientific Publishing, Singapore (1998).
- 4.12 W.N. Unertl, *J. Vac. Sci. Technol. A* 17 (1999) 1779—1786.
- 4.13 M.R. VanLandingham, S.H. McKnight, G.R. Palmese, J.R. Elings, X. Huang, T.A. Bogetti, R.F. Eduljee, J.W. Gillespie, Jr., *J. Adhesion* 64 (1997) 31—59.
- 4.14 Model SR830 DSP Lock-in Amplifier, Stanford Research Systems, Inc, Sunnyvale, USA (1993)
- 4.15 A.C. Fischer-Cripps, *Vacuum* 58 (2000) 569—585.
- 4.16 S.J.B. Reed, *Electron Microprobe Analysis*, Cambridge University Press, Cambridge (1975).
- 4.17 H.-J. Butt, K. Graf, M. Kappl, *Physics and Chemistry of Interfaces*, Wiley-VCH, Weinheim (2003).
- 4.18 K. Tsutsumi, Y. Nagasawa, *JEOL News* 38 (2003) 41—45.
- 4.19 D.B. Williams, *Practical Analytical Electron Microscopy in Materials Science*, Verlag Chemie Intl, Deerfield (1984).
- 4.20 P.S. Turner, C.E. Nockolds, S. Bulcock in: *Surface Analysis Methods in Materials Science*, 2nd ed, D.J. O'Connor, B.A. Sexton, R.St.C. Smart (Eds.), Springer, Heidelberg (2003).

Chapter 5

- 5.1 N.G. Chechenin, J. Bottiger, J.P. Krog, *Thin Solid Films* (1997) 70—77.
- 5.2 W.C. Oliver, G.M. Pharr, *J. Mater. Res.* 7 (1992) 1564—1583.
- 5.3 N.A. Burnham, A.J. Kulik, G. Gremaud, P.-J. Gallo, F. Oulevey, *J. Vac. Sci. Technol. B* 14 (1996) 794—799.
- 5.4 F. Oulevey, G. Gremaud, A. Semoroz, A.J. Kulik, N.A. Burnham, E. Dupas, D. Gourdon, *Rev. Sci. Instrum.* 69 (1998) 2085—2094.
- 5.5 M. Munz, J. Chung, G. Kalinka in: *Adhesion – Current Research and Application*, W. Possart (Ed.), 103—123, Wiley-VCH, Weinheim (2005).
- 5.6 K.L. Johnson, *Contact Mechanics*, Cambridge University Press, Cambridge (1985).
- 5.7 M. Munz, PhD Dissertation, Technische Universität Berlin (1999).
- 5.8 T.P. Skourlis, R.L. McCullough, *J. Appl. Polym. Sci.* 62 (1996) 481—490.
- 5.9 M.R. VanLandingham, R.F. Eduljee, J.W. Gillespie, Jr., *J. Appl. Polym. Sci.* 71 (1999) 699—712.
- 5.10 F. Meyer, G. Sanz, A. Eceiza, I. Mondragon, J. Mijovic, *Polymer* 36 (1995) 1407—1414.
- 5.11 S.G. Hong, T.C. Wang, *J. Appl. Polym. Sci.* 52 (1994) 1339—1351.
- 5.12 M. Munz, H. Sturm, E. Schulz, *Surf. Interface Anal.* 30 (2000) 410—414.
- 5.13 G. Owen, J.R. Sheats: in *Microolithography Science and Technology*, J.R. Sheats, B.W. Smith (Eds.), 367—401, Marcel Dekker, New York (1998).
- 5.14 M. Hatzakis, *J. Electrochem. Soc.* 116 (1969) 1033—1037.
- 5.15 W. Chen, H. Ahmed, *Appl. Phys. Lett.* 62 (1993) 1499—1501.
- 5.16 C. Vieu, F. Carcenac, A. Pepin, Y. Chen, M. Mejias, A. Lebib, L. Manin-Ferlazzo, L. Couraud, H. Launois, *Appl. Surf. Sci.* 164 (2000) 111—117.
- 5.17 W.H. Wong, E.Y. Pun, *J. Vac. Sci. Technol. B* 19 (2001) 732—735.
- 5.18 D.L. Smith, *Thin-Film Deposition: Principles & Practice*, McGraw-Hill, Inc., New York (1995).

- 5.19 H.-J. Butt, K. Graf, M. Kappl, *Physics and Chemistry of Interfaces*, Wiley-VCH, Weinheim (2003).
- 5.20 E. Meyer, R.M. Overney, K. Dransfeld, T. Gyalog, *Nanoscience: Friction and Rheology on the Nanometer Scale*, World Scientific, Singapore (1998).
- 5.21 M. Munz, H. Sturm, W. Stark, *Polymer* 46 (2005) 9097—9112.
- 5.22 K. Dusek, *Angew. Makromol. Chem.* 240 (1996) 1—15.

Chapter 6

- 6.1 R.G. Dillingham, F.J. Boerio, *J. Adhesion*, 24 (1987) 315—335.
- 6.2 J.A. Kelber, R.K. Brow, *Appl. Surf. Sci.* 59 (1992) 273—280.
- 6.3 A.A. Roche, J. Bouchet, S. Bentadjine, *Int. J. Adhes. Adhes.* 22 (2002) 431—441.
- 6.4 R.H. Hansen, J.V. Pascale, T. DeBenedictis, P.M. Rentzepis, *J. Polym. Sci. Part A*, 3 (1965) 2205—2214.
- 6.5 M.G. Chan, D.L. Allara, *J. Colloid Interf. Sci.* 47 (1974) 697—704.
- 6.6 S.G. Hong, T.C. Wang, *J. Appl. Polym. Sci.* 52 (1994) 1339—1351.
- 6.7 J. Crank, *The Mathematics of Diffusion* (1975) Clarendon Press, Oxford.
- 6.8 R.E. Cuthrell, *J. Appl. Polym. Sci.* 52 (1994) 1339—1351.
- 6.9 K. Dušek, *Angew. Makromol. Chem.* 240 (1996) 1—15.
- 6.10 K.E. Lüttgert, R. Bonart, *Progr. Colloid Polym. Sci.* 64 (1978) 38—42.
- 6.11 K. Dušek, *Adv. Polym. Sci.* 78 (1986) 1—59.
- 6.12 M. Giraud, T. Nguyen, X. Gu, M.R. VanLandingham in: *Proc. 24th Adhesion Society Annual Meeting*, J.A. Emerson (Ed), 260—262, Adhesion Society, Blacksburg, Virginia, USA (2001).
- 6.13 R.E. Cuthrell, *J. Appl. Polym. Sci.* 11 (1967) 949—952.
- 6.14 J.L. Racich, J.A. Koutsky in: *Chemistry and Properties of Crosslinked Polymers*, S. Labana (Ed), 303—323, Academic Press, New York (1977).
- 6.15 M.R. VanLandingham, R.F. Eduljee, J.W. Gillespie, Jr., *J. Appl. Polym. Sci.* 71 (1999) 699—712.
- 6.16 J. Mijović, J.A. Koutsky, *Polymer* 20 (1979) 1095—1107.
- 6.17 J.L. Racich, J.A. Koutsky, *J. Appl. Polym. Sci.* 20 (1976) 2111—2129.
- 6.18 M. Munz, B. Cappella, H. Strum, M. Geuss, E. Schulz, *Adv. Polym. Sci.* 164 (2003) 87—210.

Acknowledgment

The author is truly honored to acknowledge his gratitude:

Prof. M. H. Wagner for fruitful suggestions for my thesis and his generous regards in order to progress this doctorate work smoothly,

Dr. Martin Munz and *Dr. Heinz Sturm* for organizing and providing a state-of-the-art project, Our SFM group for the inspiring work-atmosphere including interesting discussions during the espresso breaks,

Dr. Munz for his guidance, willingness, thoughtfulness, and friendship from the moment of my arrival at the Tegel Airport until the completion of my PhD,

Dr. Sturm for facilitating the research project, and for accommodating a TV next to the ESEM, so that I could watch World Cup 2002 in Korea and Japan upon my arrival in Berlin.

Dr. Eckhard Schulz for his warm support and kind care during my time at BAM, and for his continuous effort to bond our group together with a great (!) sense of humor,

Herr Rüdiger Sernow for helping me building the experimental setups and letting my two-wheeled vehicles run smoothly,

Dr. Gerhard Kalinka for showing me how to run depth-sensing indentation and for being a nice office neighbor,

Herr Thomas Linke for solving all the computer-related problems,

Frau Martina Bistriz for sample preparations and some of the SEM analysis,

Frau Ingrid Urban and *Frau Heidemarie Rooch* (BAM V.1) for the TEM-EDX analysis.

BAM for the financial support as a part of its PhD program,

Mother for her unlimited love for her sons,

Friends, who visited, invited, sent mails and packages, and gave me kind consideration in many different ways.

The memories won't be forgotten.

About the author:

Jaeun Chung (정 재운, Jeffrey Chung)

Born in Pusan (or Busan), Korea on August 26, 1974. He lived in Pusan and Seoul until the age of 16. During 12 years in USA, he spent most of the time in Seattle, Washington before starting the PhD program in Berlin in June 2002.

Education:

Bachelor of Science in Chemical Engineering at Univ. of Washington, Seattle, WA, USA

Master of Engineering in Chemical Engineering at Clarkson University, Potsdam, NY

Master of Business Administration at Clarkson University, Potsdam, NY, USA

Experience:

Internship, University of Applied Science (Fachhochschule Nürnberg) (1998)

Materials Engineer (Internship), Corning Incorporated, Corning, New York (2000)

Sales Engineer, K-tek International, Inc., Portland, Oregon (2001 – 2002)

Hobby:

Tennis Instructor at University of Washington

Assistant Tennis Coach for Women's tennis team at Clarkson University

Traveled over 20 countries and speaks Korean, English and German.